# EXPERIMENTAL AND THEORETICAL INVESTIGATION OF BIOMASS-$CO_2$ TRANSCRITICAL BRAYTON CYCLES AND HEAT EXCHANGER OPTIMIZATIONS

A thesis submitted for the degree of Doctor of Philosophy

By

**Xinyu Zhang**

Department of Civil and Building Services Engineering

School of the Built Environment and Architecture

London South Bank University

July 2022

# Abstract

Advanced energy conversion technologies can convert the massive amounts of waste heat rejected by industrial operations into power and useable heat. In this thesis, a small-scale transcritical $CO_2$ Brayton Cycles power generation test system integrated with biomass has been designed and constructed with purposely selected and manufactured system components. This thesis contributes to the knowledge and characterization of biomass-$CO_2$ transcritical Brayton Cycles. It is based on both experimental experience, CFD models and thermodynamic models.

Heat exchangers in power cycles highly influence the efficiency of system. Finned-tube gas cooler has been widely used in industries, and finned-tube water cooler was used in the proposed system. However, due to large amount of fins and then the difficulty of evaluating tube side temperature profile. A novel 1D-3D CFD model was carried out to investigate performance of $CO_2$ finned-tube gas cooler and correspondingly evaluate the feasibility of using it in biomass-$CO_2$ transcritical Brayton Cycles. The CFD model has been validated by comparing with published literatures. The novel CFD model allows to predict the finned-tube type heat exchanger with good accuracy and also to explore possible improvements or different configurations. The lower $CO_2$ outlet temperature makes it is an alternative gas cooler used in biomass-$CO_2$ transcritical Brayton Cycle systems. In addition, it is found that longitudinal heat conduction along fins can lead to inverse heat transfer between adjacent tubes and thus capacity degradation of the heat exchanger. Therefore, CFD models have been purposely developed for the $CO_2$ gas cooler with split fins to quantify the effect of the heat conduction through fins. Results show that average heating capacity can be increased by 10% when split fins are applied.

A detailed CFD simulation model of a particular designed shell-and-tube supercritical $CO_2$ gas heater in a biomass-$CO_2$ power generation system has been developed based on actual heat exchanger structural design and applicable operating conditions. The model has been validated with both manufacturer operational data and empirical correlations. The simulation results showed that increasing flue gas mass flow rate, flue gas temperature and $CO_2$ mass flow rate can enhance differently the heating capacity of the heat exchanger. It is also found that by minimizing the distance between hot fluid pipe inlet and cold fluid outlet ports, as well as hot fluid pipe outlet and cold fluid inlet ports, the heating capacity of the shell-and-tube heat exchanger and the performance of its associated system can be significantly improved.

In this thesis, a theoretical study was conducted to investigate the performance of biomass-$CO_2$ transcritical Brayton cycles. The thermodynamic model was integrated with the CFD results of $CO_2$ gas heater to precisely evaluate the power generation, power consumption, exergy loss, system thermal efficiency and system exergy efficiency at different operating conditions. Results showed that there exists an optimal $CO_2$ turbine inlet pressure or $CO_2$ turbine outlet pressure to maximize the system thermal efficiency and system exergy efficiency. Model development and simulation can contribute significantly to understand the system operations and eventually optimize the system structure designs and controls.

# Publications

*Published journal paper*

**Zhang, X.,** Ge, Y., Sun, J., Li, L. and Tassou, S.A., 2019. CFD modelling of finned-tube $CO_2$ gas cooler for refrigeration systems. *Energy Procedia*, 161, pp.275-282.

**Zhang, X.,** Ge, Y. and Sun, J., 2020. CFD performance analysis of finned-tube $CO_2$ gas coolers with various inlet air flow patterns. *Energy and Built Environment*, 1(3), pp.233-241.

**Zhang, X.Y.,** Ge, Y.T. and Sun, J.N., 2020. Performance analysis of finned-tube $CO_2$ gas cooler with advanced 1D-3D CFD modelling development and simulation. *Applied Thermal Engineering*, 176, p.115421.

**Zhang, X.** and Ge, Y.T., 2021. The effect of heat conduction through fins on the performance of finned-tube $CO_2$ supercritical gas coolers. *International Journal of Heat and Mass Transfer*, 181, p.121908.

**Zhang, X.** and Ge, Y., 2022. Design optimization of shell-and-tube supercritical $CO_2$ gas heater in a biomass-$CO_2$ power generation system. (Submitted on Applied Thermal Engineering - under review)

Li, M., Yin, N., Ge, Y. and **Zhang, X.,** 2019. Design and Dried Performance Test of a Solar Assisted Heat Pump Two-Stage Drier. *In Advances in Manufacturing Technology XXXIII* (pp. 412-417). IOS Press.

Li, M., Guan, Z., Ge, Y., **Zhang, X.** and Ling, C., 2020. Effect of pretreatment on water migration and volatile components of heat pump dried tilapia fillets. *Drying Technology*, 38(14), pp.1828-1842.

*Published conference paper*

**Zhang, X.,** Ge, Y., Sun, J., 2019. Performance analysis of finned-tube $CO_2$ gas cooler with advanced CFD modelling development and simulation. The 25th IIR International Congress of Refrigeration (ICR). Montreal, Canada. Paper ID 835.

**Zhang, X.,** Ge, Y., 2019. CFD performance analysis of finned-tube $CO_2$ gas coolers with various inlet air flow patterns. The International Conference on Energy and Sustainable Futures (ICESF). Nottingham, UK.

**Zhang, X.,** Ge, Y., Sun, J., Lang, P., 2020. Performance analysis of a Shell-and-tube $CO_2$ supercritical heater with CFD modelling. 6th IIR International Conference on Sustainability and the Cold Chain (ICCC). Nantes, France. Paper ID 292303.

Ge, Y., **Zhang, X.,** Ling C., Lang, P., 2020 Power Generation and Heat Recovery from Biomass with Advanced $CO_2$ Thermodynamic Power Cycles: Modelling Development and Simulation. IIR Rankine 2020 Conference - Advances in Cooling, Heating and Power Generation. Virtual. Paper ID 1229

**Zhang, X.,** Ge, Y., 2020. Effects of split fins on the performance of finned-tube $CO_2$ gas coolers. International Conference on Applied Energy (ICAE). Bangkok/Virtual, Thailand. Paper ID 511.

**Zhang, X**. and Ge, Y., 2021. Performance Analysis of Shell-and-tube Supercritical $CO_2$ Gas Heater in a $CO_2$ Power Generation System. International Conference on Applied Energy (ICEA). Thailand/Virtual. Paper ID 541.

# Dedication

To

My parents

Guiping Zhang and Lifen Ma

My parents-in-law

Zhongjun Fan and Chunbo Xu

My husband

Zeng Fan

For their endless love, support and encouragement.

# Acknowledgements

I would like to express my deepest gratitude to Prof. Yunting Ge for his continuous support and valuable feedbacks during the whole period of my PhD career. His immense knowledge and plentiful experience have inspired me throughout my academic research and daily life. I would like to thank Prof. Issa Chaer for his treasured support and kind help, his support has made my study and life in London South Bank University a wonderful time.

I am extremely grateful to Dr. Jining Sun for his excellent guidance and invaluable assistance in the area of CFD simulation. I would also like to thank Dr. Liang Li for his wonderful guidance and help in setting up the experimental test rig. Additionally, I am also thankful to my friend and PhD colleague, Pingyuan Lang, for his valuable assistance.

I could not have undertaken this journey without the emotional and financial support of my parents and my parents-in-law, Guiping Zhang and Lifen Ma, Zhongjun Fan and Chunbo Xu.

Finally, I would like to thank my husband Dr. Zeng Fan from the deepest of my heart for his tremendous understanding, encouragement and love during this difficulty journey of PhD.

# Contents

## Chapter 5 – Investigation of the Effect of Heat Conduction Through Fins on The Performance of Finned-tube $CO_2$ Gas Coolers .................................. 86

## Chapter 6 - Design Optimization of Shell-and-tube Supercritical $CO_2$ Gas Heater in the Biomass-$CO_2$ Power Generation System ........................... 110

## Chapter 7- Thermodynamic Analysis of Biomass-$CO_2$ Transcritical Brayton Cycles Combined with CFD Simulations. ........ 138

# List of Figures

# List of Tables

# Nomenclature

| | |
|---|---|
| A | area ($m^2$) |
| $A_s$ | bundle crossflow area ($m^2$) |
| Cp | specific heat at constant pressure ($J\ kg^{-1}\ K^{-1}$) |
| d | tube inner diameter (m) |
| D | depth (m) |
| $D_e$ | equivalent diameter (m) |
| $D_s$ | shell side diameter (m) |
| $\dot{E}$ | rate of exergy (kW) |
| f | fanning friction factor |
| $f_p$ | fin pitch (m) |
| $G_s$ | mass velocity ($kg\ m^{-2}\ s^{-1}$) |
| $h$ | enthalpy ($J\ kg^{-1}$) |
| H | height (m) |
| HTC | heat transfer coefficient ($W\ m^{-2}\ K^{-1}$) |
| j | Colburn factor |
| $J_c$ | segmental baffle window correction factor |
| $J_l$ | correction factor for baffle leakage effects |

| | |
|---|---|
| $J_b$ | correction factor for bundle bypass effects |
| $J_s$ | correction factor for baffle spacing |
| $J_r$ | correction factor for laminar flow |
| $k$ | thermal conductivity (W $m^{-1}$ $K^{-1}$) |
| $L$ | flow length (m) |
| $\dot{m}$ | mass flow rate (kg $s^{-1}$) |
| $N$ | number of tube row |
| $Nu$ | Nusselt number |
| $P$ | pressure (Pa) |
| $\Delta P_c$ | pressure drop in the cross-flow section (Pa) |
| $\Delta P_w$ | pressure drop in the window (Pa) |
| $\Delta P_e$ | pressure drop in the entrance and exit sections (Pa) |
| $Pr$ | Prandtl number |
| $Q$ | heat transfer (W) |
| $r_p$ | pressure ratio |
| $Re$ | Reynolds number |
| $Re_{in}$ | Reynolds number based on air frontal velocity |
| *STHXA* | shell-and-tube heat exchanger A |
| *STHXB* | shell-and-tube heat exchanger B |

| | |
|---|---|
| $T$ | temperature (K) |
| $u$ | velocity (m s$^{-1}$) |
| $u, v, w$ | velocity components (m s$^{-1}$) |
| $v_a$ | air velocity (m s$^{-1}$) |
| $W$ | width (m) |
| $W$ | power (kW) |
| $x, y, z$ | direction coordinates (m) |
| $\eta$ | thermal efficiency |

Greek symbols

| | |
|---|---|
| $\Delta$ | difference |
| $\boldsymbol{\rho}$ | density (kg m$^{-3}$) |
| $\boldsymbol{\xi}$ | friction coefficient |
| $\boldsymbol{\mu}$ | dynamic viscosity (Pa s) |
| $\mu_t$ | turbulent molecular viscosity (Pa s) |
| $\sigma_k$ | turbulent Prandtl number for energy dissipation rate |
| $\sigma_\varepsilon$ | turbulent Prandtl number for kinetic energy |
| $\nu$ | kinematic molecular viscosity (m$^2$ s$^{-1}$) |
| $\varepsilon$ | effectiveness |

| | |
|---|---|
| α, β, γ | correlation parameters (dimensionless) |

Subscripts

| | |
|---|---|
| $a$ | air |
| $ain$ | air inlet |
| $av$ | average |
| $b$ | baffle |
| c | cooling water |
| $comp$ | compressor |
| ex | exergy |
| $gh$ | gas heater |
| $gc$ | gas cooler |
| $i$ | $i$th grid |
| $in$ | inlet |
| $l$ | loss |
| $m$ | mean |
| $o$ | outer |
| $out$ | outlet |
| $r$ | refrigerant |
| $rin$ | refrigerant inlet |

| | |
|---|---|
| *revout* | refrigerant at evaporator outlet |
| *revin* | refrigerant at evaporator inlet |
| *rcpout* | refrigerant at compressor outlet |
| *rcpin* | refrigerant at compressor outlet |
| *rec* | recuperator |
| *s* | shell side |
| s | isentropic |
| *t* | tube side |
| *t* | turbine |
| *w* | wall |

# Chapter 1 Introduction

## 1.1Energy Consumption and Heat Recovery

With the population growing and economic development, fossil fuels such as oil, coal and nature gas are still the primary resources for power generation in the global world, as shown in Figure 1.1. Oil continues to comprise the greatest portion of the energy mix (31.2 %). In 2020, coal contributed for 27.2% of total primary energy consumption, slightly increased from 27.1% in the previous year [1]. However, these primary sources are finite, if we continue to use them as usual way they will be eventually run out. In addition, consumption of conventional fuels can lead to environmental problems such as global warming, ozone depletion, and atmospheric pollution. Greenhouse gases (GHG) are the most prevalent industrial emission. Carbon dioxide is the primary pollutant produced by GHG emissions. Global $CO_2$ emissions from energy combustion and industrial processes reached their highest yearly level ever in 2021, reaching to a high record of 36,3 gigatons (Gt), increased by 6% from 2020 [2].

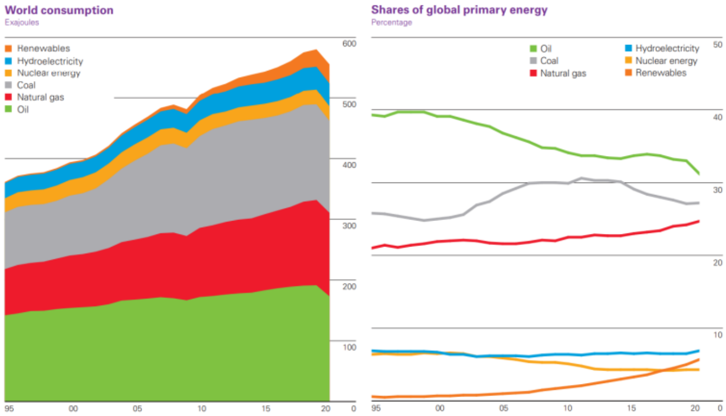

Figure 1. 1 Word energy consumption [1].

In 2020, the consumption of oil and gas are 31.2% and 41.9% of total energy consumption in UK as demonstrated in Figure 1.2. Although over the past decades, consumption of bioenergy and waste has grown, only 11% of total energy consumption [3].

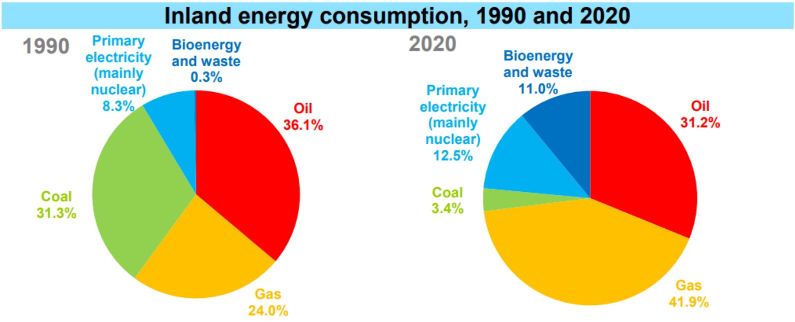

**Figure 1. 2 Inland energy consumption in UK [3].**

A decarbonized society is an unavoidable tendency to protect the environment while also meeting human requirements. Utilization of renewable energy is gaining increasing interest. Moreover, In many manufacturing industries, 20% ~ 50% of the energy consumed by manufacturing is lost as waste heat [4]. However, this heat cannot be recovered completely on-site and used for district heat. It is then discharged into the air, which has significantly negative impact on human health, biodiversity and environment. Generally, waste heat can be categorized as low-temperature (<230 ℃), medium-temperature (230-650 ℃) and high-temperature (>650 ℃) [5]. As a consequence, it is vital to optimize heat recovery technologies and increase the conversion efficiency of power producing systems in order to avoid energy loss as much as feasible.

## 1.2 Biomass-based power generation technologies

As discussed above, it is imperative to improve the conversion efficiency of power generation cycles, including explore the alternative heat sources, different working fluid and promising energy conversion technologies.

### 1.2.1 Opportunities of using biomass

Biomass has become one of the world leaders in development of low-carbon power. It is a renewable and inexhaustible source generated from plants, animals and microorganisms. There are two thermochemical conversion routes to use biomass for supplying electricity and heating, gasification and combustion. Combustion is the most mature technology to conversion biomass to useful electricity and heating. By using biomass as a heat source, not only can effectively reduce biomass-waste, but also provide high temperature always higher than 900 ˚C [6] during combustion process. In addition, if biomass is combusted completely, the produced carbon dioxide is equal to the amount absorbed by biomass growth. Therefore, biomass makes no net contribution on carbon dioxide emissions to the atmosphere. As a consequence, the substitution of fossil fuels by biomass makes significant contributions to the reduction of $CO_2$ emissions.

### 1.2.2 Opportunities of using carbon dioxide

$CO_2$ is a natural, non-toxic and non-flammable working fluid with superb thermophysical properties including higher values of density, latent heat, specific heat, thermal conductivity and volumetric cooling capacity as well as lower value of viscosity [7], $CO_2$ plays an important role in many energy conversion systems. Its critical properties are 7.4 Mpa and 31 ℃ respectively. Advantages of using $CO_2$ in thermodynamic cycles can be summarized as: 1) it is environmental-friendly with no ozone depleting potential

(ODP) and low global warming potential (GWP). 2) It is abundant, no-toxic and non-combustible. 3) it does not react with the materials of components. 4) It has good thermodynamic and transport properties. For high temperature heat source cycles, according to low critical temperature of $CO_2$, $CO_2$ can easily go through both subcritical and supercritical regions, can be a $CO_2$ transcritical cycle or a $CO_2$ Brayton cycle (a gas cycle). Therefore, $CO_2$ has been utilized extensively in supermarket refrigeration [8], and a number of power generation system used transcritical (T-$CO_2$) Rankine cycle [9-11].

### 1.2.3 power generation systems

In biomass-based power generation system, biomass based Organic Rankine Cycle technology has been well-developed. However, the electrical efficiency of this biomass-fired ORC system was between 7.5% and 13.5% [12]. Electricity generation efficiency was 1.41% for a biomass-based recuperated ORC micro-CHP system [13]. Therefore, It is necessary to make great efforts to improve biomass-based power plant electric efficiency further. Besides, it is suggested that the utilization of Organic Rankine Cycle is more suitable for low-temperature heat sources [14]. And due to the limitation of maximum temperature heat transfer medium, large temperature difference between working fluid and heat sources leading to lower efficiency. Furthermore, for reducing the environment negative impacts of organic working fluid, $CO_2$ has been attracted more and more attention as a promise working fluid power generation system. It has been approved that transcritical $CO_2$ cycles can achieve higher power output due to better thermal match between heat source and working fluid compared to conventional Organic Rankine Cycles. However, T-$CO_2$ Rankine Cycles demonstrated a lower efficiency because of higher pump power consumption [15]. For achieving higher efficiency, Supercritical/Transcritical $CO_2$ Brayton Cycles (gas cycles) are considered as a promising technology. The advantages of Supercritical/Transcritical $CO_2$ Brayton Cycle are higher thermal efficiency and compactness components make it a cost-effective and promising technology for waste heat recover from high temperature heat sources. Correspondingly, theoretical and experimental analysis of the biomass-$CO_2$ Superctitical/Transcritical Brayton Cycle need to be thoroughly carried out.

### 1.2.4 Heat exchangers in power generation systems

Heat exchangers play significant role in power generation systems to transfer heat from heat source to working fluid directly or indirectly. A finned-tube gas cooler is typically used in a $CO_2$ transcritical Cycle due to its characteristics of simplicity, durability and versatility. In supercritical or transcritical operations, finned-tube heat exchanger release heat from high temperature $CO_2$ to ambient temperature without condensation phase. Thus, the finned-tube heat exchanger is classified as $CO_2$ gas cooler. It also feasible to use a $CO_2$ gas cooler in $CO_2$ Supercritical/Transcritical Brayton Cycle for cooling $CO_2$. Besides, considering the high temperature and high pressure involved in the heat transfer fluids, a shell-and-tube type heat exchanger can be the most appropriate $CO_2$ gas heater used in the biomass-$CO_2$ power generation system [16]. However, the performance of power generation systems such as $CO_2$ transcritical cycles and Supercritical/Transcritical $CO_2$ Brayton Cycles can be improved by operational of heat exchangers and $CO_2$ exit temperature profiles [7]. Numerical simulations of different types of heat exchanger need to be carried out for performance evaluation and optimization of its associated power generation systems.

## 1.3 Research aims and objectives

The PhD research in this thesis aims to provide experimental and theoretical investigations of biomass power generation test system with $CO_2$ transcritical Brayton cycles. Numerical studies and improvements of a finned-tube $CO_2$ gas cooler and a $CO_2$ shell-and-tube gas heater in the biomass-$CO_2$ transcritical Brayton Cycle need to be carried out. The objectives of this research are:

- Conduct literature review on the designs and performance of transcritical carbon dioxide cycles and Brayton cycle systems.
- Carry out the design and construction of biomass-$CO_2$ Transcritical Brayton Cycle system.
- Investigate and optimize the performance of finned-tube $CO_2$ gas cooler and its associated system at various heat exchanger designs and operating conditions by using Computational Fluid Dynamics (CFD) modelling method.
- Investigate and optimize the performance of shell-and-tube $CO_2$ gas heater at various heat exchanger designs and operating conditions by using Computational Fluid Dynamics (CFD) modelling method.
- To thermodynamically model the power generation system with biomass-$CO_2$ transcritcial Brayton cycle.

## 1.4 Structure of thesis

This thesis is organized as follows:

**Chapter 1** Provides an overview background of this research, aims and objectives, and the structure of this thesis.

**Chapter 2** presents the review of research work of Rankine Cycle and Brayton Cycle. This chapter also presents overview of finned-tube heat exchangers and shell-and-tube heat exchangers used in thermodynamic power cycles.

**Chapter 3** presents detailed design and construction of biomass-$CO_2$ transcritical Brayton Cycle system, including introduction of each component, control and electricity system, and data acquisition.

**Chapter 4** carries out detailed CFD simulation of finned-tube $CO_2$ gas cooler under different operating conditions. New coupled 1D and 3D CFD model on a finned-tube $CO_2$ gas cooler has been proposed and developed. The CFD model has been validated by comparing with literatures for parameters including airside heat transfer coefficient, refrigerant side temperature profile as well as heating capacity. The model has been applied to predict the heat exchanger performance at different operating conditions of both air and refrigerant sides and maldistributions of air flow inlet.

**Chapter 5** proposed an effective method to minimize the heat conduction effects that the heat exchanger design with split fins between tube rows was applied. From the results of Chapter 4, it was found that longitudinal heat conduction influence the performance of $CO_2$ negatively. Further verification and analysis were carried out by detailed CFD simulations.

**Chapter 6** presents a comprehensive CFD simulation model of a particular designed shell-and-tube supercritical $CO_2$ gas heater in a biomass-$CO_2$ power generation system, which was based on actual heat exchanger structural design and applicable operating condition. The model has been validated using both operational data from the manufacturer and empirical correlations. Therefore, it is applied to investigate and predict the performances of the heat exchanger and its associated system at various heat exchanger designs and operating conditions.

**Chapter 7** presents thermodynamic analysis of biomass-$CO_2$ transcritical Brayton cycles combined with CFD results of $CO_2$ gas heater. Simulations were developed and calculated in Engineering Equation Solver (EES) software. Variations of turbine power generation, compressor power consumption, $CO_2$ mass flow rate, system thermal efficiency and system exergy efficiency at different operating conditions were analyzed.

**Chapter 8** presents overall conclusions of thesis and recommendations for future work.

# Chapter 2 Literature Review

As discussed in Chapter 1, considering the environmental impact and energy loss in industries, it is essential to explore alternative technologies to decrease the primary fuel consumption, to reduce $CO_2$ emissions and to improve conversion efficiency of power cycles.

## 2.1 Organic Rankine Cycle

### 2.1.1 Basic ORC configuration

Over the past decades, Organic Rankine Cycle has become a mature energy conversion technology. ORC is a power generation technique based on the Steam Rankine Cycle. Working fluid selection is the primary distinction between the ORC and traditional Rankine Cycle. Water is replaced by organic compound by comparing with traditional Rankine Cycle. Organic Rankine Cycle is superior to the traditional steam Rankine Cycle in terms of performance when employing a low-temperature heat source due to its greater thermal efficiency. Typical heat sources include solar energy, geothermal energy, and industrial waste heat. Working fluids for ORC are effective at low temperatures (150 °C) and medium temperatures (150-300 °C) [17]. When waste heat is below 370°C, the Steam Rankine Cycle using water as the working fluid has a low recovery efficiency [18]. The basic ORC system consists of an evaporator, an expansion device, a condenser and a pump as shown in Figure 2.1. The subcritical ORC T-s diagram is also indicated in Figure 2.1. The working fluid exits the condenser, which is then compressed to a high pressure and heated to a saturated or supercritical vapor within the evaporator. After that it is expended in expender device to generate electricity. The working fluid is fully condensed in condenser. Then the cycle repeats.

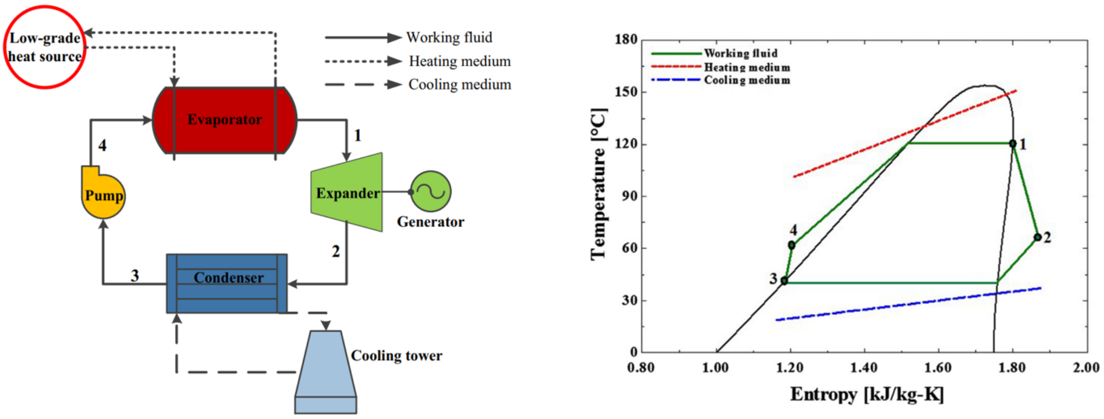

(a)

(b)

Figure 2. 1 (a) Schematic of the simple ORC layout; (b) T-s diagram of the simple ORC [19].

### 2.1.2 Working fluid selection

Working fluid selection is a certain challenge for a ORC application. The potential working fluid used in ORC includes hydrochlorofluorocarbons (HCFCs), hydrofluorocarbons (HFCs) and hydrocarbons (HCs), refrigerants, ethers and siloxanes. However, the ozone depleting substances such as HCFCs need to be phased out. This is because these organic compounds highly depleting the stratospheric ozone layer and have high Global Warming Potential (GWP). Although HFCs have zero Ozone Depleting Potential (ODP) but higher Global Warming Potential (GWP). HCs are considered as an alternative refrigerant; pinching problem may occur in ORC systems. The desirable thermos-physical properties of working fluids should be: environmental friendly as much as possible, low critical temperature and pressure, small specific volume, non-toxic, high latent heat, high thermal conductivity and low viscosity [20]. Saleh et al. [21] studied 31 pure component working fluids for Organic Rankine Cycle. The operation temperature varied between 30 ℃ and 100℃. The pressure was controlled at 20 bars. Results showed that the highest thermal efficiency is 13%. It is suggested that the selection of working fluid is highly dependent on the maximum temperature of it.

### 2.1.3 ORC applications

ORC has been applied for different types of heat source. ORC has been utilized to extract energy from agricultural byproducts and biomass [22-24]. Algieri et al. proved that by adopting internal heat exchanger or recuperator can increase electrical efficiency [25]. However, biomass-based ORC still faces the issue of a reduced electric efficiency, normally less than 15% [12-13]. Due to ORC is more appropriate for low-temperature heat sources, which means it is a promising technology to generate electricity from solar energy. From the results of Cohen et al. [26], the overall solar to electricity efficiency is 12.1% by utilizing solar-based ORC. However, very few solar ORC plants are constructed on commercial scale. Improving the scale of solar power plant on only rely on cost-effective and high efficiency solar concentrating collectors, but also depends on operability and better performance of ORC. Some researchers also evaluated the performance of ORC for waste heat recovery [27– 30]. ORC is a more viable option for the conversion of low to medium temperature heat sources into electricity.

## 2.2 $CO_2$ transcritical Power cycle

### 2.2.1 $CO_2$ transcritical Cycle configuration

By comparing with organic substances, $CO_2$ has superb thermal-physical properties which was the first working fluid used in supercritical/transcritical cycles [31]. due to its lower critical temperature and pressure, supercritical state can be easily achieved. A basic $CO_2$ transcritical cycle (T-$CO_2$) consists of a vapor generator, a turbine, a condenser and a pump as seen in Figure 2.2. The flow processing across transcritical cycle is similar as Organic Rankine Cycle. The major difference between subcritical and transcritical is heating process. For transcritcial cycle, working fluid can be compressed directly to supercritical state, as shown in Figure 2.2 (b).

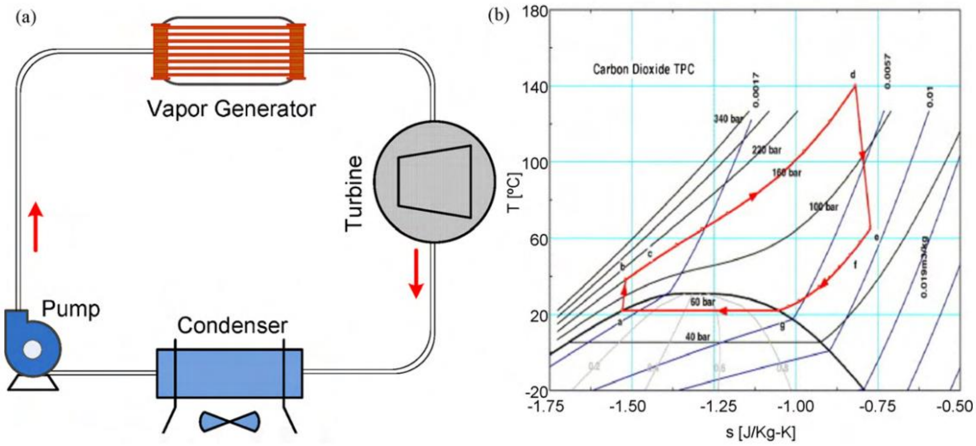

Figure 2. 2 Configuration and processes of a $CO_2$ Transcritical Cycle: (a) configuration. (b) T-s diagram [32].

### 2.2.2 $CO_2$ transcritical cycle applications

Although ORC has been widely used in the conversion of low-grade heat source to electricity, the maximization of power output is limited by the constant temperature evaporation process, which is not an advantage option for sensible heat sources. Due to avoid the isothermal boiling process, $CO_2$ of Transcritical Cycle provides better thermal match with heat source, and thus higher thermal efficiency can be achieved by comparing with ORC as seen in Figure 2.3 [15]. The pinching-problem is effectively solved by using transcritical $CO_2$.

Chen et al. [15] carried out a study of comparison of $CO_2$ transcritical cycle and R123 Orgainic Rankine Cycle in waste heat recovery. The low-grade heat source with temperature of 150 ˚C was used. Results indicated that T-$CO_2$ cycle has higher power output than that of ORC. Yamaguchi et al. [33] investigated the potential of T-$CO_2$ power cycle with solar power heat source. From the results that heat recovery efficiency can be reached to 65%. Angelino [34] carried out a detailed study on transcritical $CO_2$ cycle, results showed that T-$CO_2$ cycles has better performance than steam Rankine Cycle. However, for high temperature heat source, $CO_2$ need to be cooled down to relative low temperature. Thus, the design and thermal performance of condenser could face a big challenge. By reviewing other researchers' work, the T-$CO_2$ power cycles are mostly applied for low-grade heat sources [35-40]. From the studies of Li et al. [41-42], it is known that although T-$CO_2$ cycle can improve the power output compared to conventional ORC, the thermal efficiency could be reduced due to the increasing consumption of $CO_2$ liquid pump. Recuperator is an important component which has been widely used in T-$CO_2$ power cycle for increasing system thermal efficiency. Meanwhile, it was found that a great internal irreversibility occurred in recuperator due to the large difference of specific heat between turbine outlet and pump outlet [43].

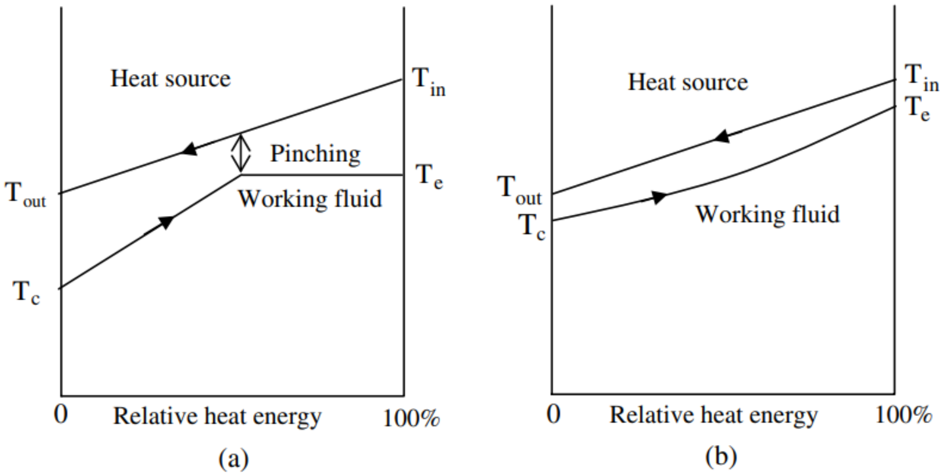

**Figure 2. 3 Schematic representation chart of the heat transfer between waste heat and working fluid in the high temperature main heat exchanger: (a) ORC cycle. (b) $CO_2$ transcritical power cycle [15].**

## 2.3 Brayton cycle

### 2.3.1 Basic Brayton Cycle configuration

It is known that although T-$CO_2$ cycle is an option for numerous applications such, the high liquid $CO_2$ pump power is a big challenge for thermal efficiency. For medium to higher temperature heat sources, Brayton cycle is a promising technology, which has characteristics of compact components and small-scale make it cost-effective. The overall size of Steam Rankine Cycle is approximately 4 times that of S-$CO_2$ Brayton cycle [44].

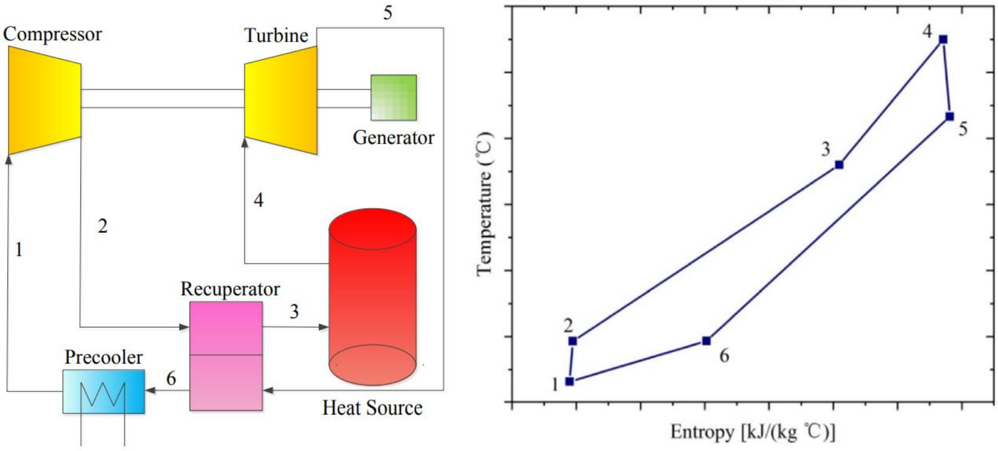

Figure 2. 4 Layout of the simple Brayton Cycle and T-S diagram [45].

The simple Brayton cycle consists of heat source heater, a turbine, a recuperator, a precooler and a compressor as seen in Figure. 2.4. The Brayton Cycle generally has four process: (1) adiabatic compression (''1''- ''2''), the working fluid is compressed under adiabatic condition; (2) isobaric heating (''2''-''4''), after passing through the recuperator, the working fluid is preheated to point ''3''. Then it enters the heater, in which working fluid is further heated to the highest temperature point ''4''; (3) adiabatic expansion (''4''-''5''), the working fluid is expanded to point ''5'', reducing the pressure to produce work by turbine; (4) isobaric heat release (''5''-''1''), working fluid is passing through the recuperator to preheat the compressed fluid to point ''6''. Then the working fluid is cooled to initial temperature point ''1'' in a cooler. Recuperator in process increases thermal efficiency greatly in Brayton Cycle.

### 2.3.2 Working fluid selection

The selection of working fluid significantly affects the size, geometry and efficiency of Brayton cycle. There are several types of working fluids are suitable for this cycle, such as air, helium, carbon dioxide, and some noble gases.

Air is a considerable working fluid, due to its abundant and cost-effective. Zhang et al. [46] presented an air Brayton cycle for recovering waste heat from blast furnace slag, with data indicating the best heat recovery efficiency is 11.98%. Although air is a promising working fluid for the Brayton cycle, it does have a few disadvantages: 1) Less heat transfer coefficient than helium. 2) For optimal system performance, a turbine's input temperature should be high.

As an inert gas, nitrogen is an appealing alternative for the Brayton cycle's working fluid. Olumayegun et al. [47] studied a nitrogen closed Brayton cycle integrated with a small modular sodium-cooled fast reactor. Results showed that the cycle efficiency was 39.44%. For the disadvantages of using nitrogen as working fluid for Brayton cycle are: 1) it also needs high turbine inlet temperature. 2) the heat transfer characteristics are not superb. 3) It may react with materials at high temperature.

Helium is an inert gas with a high coefficient of heat transfer. Brayton cycle employing helium as the working fluid has the ability to utilize the nuclear system's high output temperature. The temperature range of helium Brayton cycle is 900 to 950 ℃ [48]. Gad-

Briggs and Pilidis [49] carried out an analysis of simple and intercooled recuperated Brayton helium cycle for generation IV reactor power plant.

Comparing to other working fluids, $CO_2$ has low critical temperature and pressure, which is proper for Brayton Cycle. As shown in Figure 2.5 and Figure 2.6 high density and low compressibility factor of $CO_2$ close to its critical point, as a result of the large and rapid change in its thermodynamic properties. Compressibility factor is defined as the ratio of the actual volume to the ideal volume. From Figure 2.6, around critical point, the compressibility factor $CO_2$ is changed between 0.2 and 0.5, reducing power consumption of compressor. Therefore, the supercritical carbon dioxide (S-$CO_2$) Brayton cycle features a high thermal efficiency, a simple cycle configuration, compactness components. Using S-$CO_2$ rather than helium as the working fluid at the same temperature can increase efficiency [50-51]. Similar results are also concluded by Ishiyama et.al [52]. Therefore, $CO_2$ is the most promising working fluid for Brayton cycle.

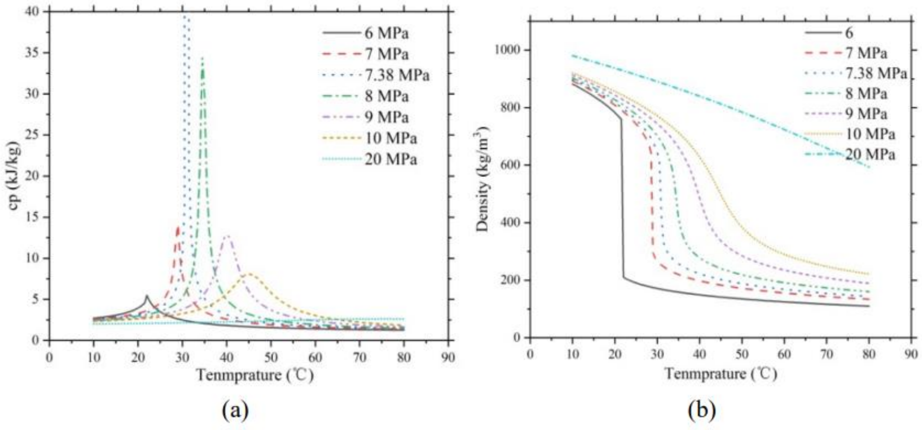

(a) (b)

Figure 2. 5 Changes of specific heat and density of $CO_2$ in different pressure and temperature [45].

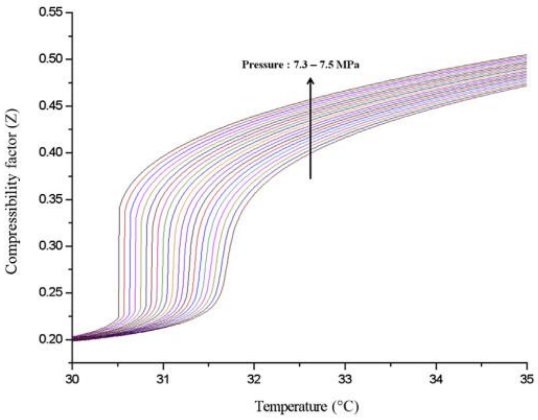

Figure 2. 6 $CO_2$ compressibility factor [2.3.1].

### 2.3.3 S-$CO_2$ Brayton Cycle applications

S-$CO_2$ Brayton Cycle is a promising technology which can be applied to nuclear energy, fossil fuel and some renewable energies. It has been studied that S-$CO_2$ Brayton Cycle has higher thermal efficiency than helium Brayton Cycle and Steam Rankine Cycle at low turbine inlet temperature of 450 ˚C – 750 ˚C [53]. in order to further increase the efficiency of S-$CO_2$ Brayton Cycle, different layouts were proposed, such as recompression, intercooling, reheating, precompression [54].

S-$CO_2$ Brayton cycle was proposed initially used for nuclear reactor to replace steam Rankine Cycle due to its high efficiency [55]. The results revealed that the thermal efficiency of the system is 50% at a turbine inlet temperature of 650 ° C, whereas the thermal efficiency of the simple Brayton cycle is 45.3 % at a turbine inlet temperature of 550 ° C. Wright et al. [56] carried out comprehensive experiments to investigate the S-$CO_2$ Brayton Cycle with solar, nuclear or fossil fuel heat sources in Sandia National Laboratories. Due to its high performance, Qiu et al. [57] studied the S-$CO_2$ Brayton Cycle based on solar power for generating electricity. An optimized recompression S-$CO_2$ Brayton Cycle for concentrating solar power application was studied, the net efficiency can be increased to 50% [58]. $CO_2$ has stable thermos-physical properties up to 1500 ˚C, the application of S-$CO_2$ Brayton Cycle in coal-fire has been investigated [59-60]. However, there is an important factor which can influence performance of S-$CO_2$ Brayton Cycle that it is difficult to manufacture the supercritical $CO_2$ compressor.

## 2.4 $CO_2$ Finned-tube gas cooler

### 2.4.1 Importance for Power cycles

Heat exchangers in power cycles highly influence the thermal efficiency of system. Due to its high compactness and low cost, finned-tube heat exchangers are widely employed in manufacturing processes and energy conversion systems such as heating, ventilation, air conditioning, and refrigeration. For a conventional finned-tube heat exchanger, it has individually or continuous fins and one or more tube rows, with air or gas fluid flowing through the fins and liquid or gas working fluid flowing through the tubes, as seen in Figure 2.7.

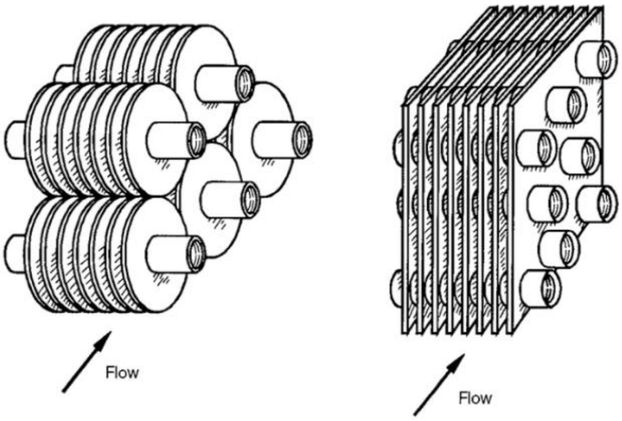

Figure 2. 7 Finned-tube heat exchangers with individually and continuous fins [61].

It has been suggested that application of internal heat exchanger integrations, employment of compression and expansion and optimal management of high-side operating pressures, the performance of $CO_2$ transcritical cycles can be enhanced [62].

A theoretical investigation [63] was carried out on a two-stage transcritical $CO_2$ refrigeration cycle equipped with a sub-cooler and intercooler. The results indicated that decreasing the $CO_2$ gas cooler's outlet temperature increased the system's coefficient of performance. The temperature difference between the $CO_2$ exit temperature and incoming air flow temperature is named as approach temperature. Lower approach temperature leads to higher cycle efficiency. Kim [64] experimentally built up a $CO_2$ refrigeration system with an internal heat exchanger to examine the control of gas cooler pressure. The system's COP could be improved by installing an internal heat exchanger and applying the proper control. In addition, it was found that there was an optimal gas cooler pressure for achieving the maximum COP value under the conditions of a particular refrigerant charge and the same heat sink temperature [65]. A method for controlling gas cooler pressure was proposed by Ge and Tassou [66] in order to maximize the system COP at specified variables, such as evaporation temperature and approach temperature. Therefore, it is essential to comprehensively investigate and optimize finned-tube gas cooler.

### 2.4.2 Experimental and numerical investigations

Many efforts have been made over the past few decades to explore the refrigerant side heat transfer and hydraulic behaviors of finned-tube heat exchanger. Gnielinski's [67] evaluation and development of general correlations of refrigerant in-tube heat transfer coefficients based on wall and bulk Nusselt numbers provided for the calculation of $CO_2$ refrigerant. Specifically, a number of researchers [68–70] experimented with the heat transfer coefficients of supercritical $CO_2$ in-tube cooling methods with various tube diameters. Based on experimental and analytical data analyses, Pitla et al. [71] determined a new correlation for calculating the heat transfer coefficient of supercritical

$CO_2$ in cooling processes. In contrast, Wang et al. [72] proposed correlations to determine the airside heat transfer coefficient and pressure drop for plain finned-tube heat exchangers based on measurements of 74 heat exchanger samples with varying geometric dimensions. These heat transfer and hydraulic calculations of both the refrigerant and air flow sides are crucial to study and analyze the heat exchanger's performance and modelling development.

Effectiveness-NTU method and LMTD method (lumped method and distributed method) are two common numerical methods applied in simulation of different heat exchangers [73]. Ge and Cropper [74] applied a detailed distributed method to model $CO_2$ gas coolers and predict $CO_2$ refrigerant temperature profiles along refrigerant pipe flow direction. Lee and Domanski [75] employed a tube-by-tube approach to evaluate the performance of finned-tube air-to-refrigerant evaporators under various operating conditions. Due to the complex performance of the airflow side and the rapid property changes of the supercritical $CO_2$ flow side in the $CO_2$ gas cooler, a highly accurate 3D CFD simulation approach is required. In comparison to experimental investigation, the CFD model can greatly minimize the time required to develop a physical prototype and allow researchers to conduct experiments in a virtual laboratory. Starace et al. [76] presented a 'hybrid method' that combines numerical and analytical methodologies to determine the total performance of a heat exchanger, beginning with a CFD simulation at the micro-scale and then proceeding to the multiscale. This method is then utilized to finned-tube evaporator. The effects of different geometry specifications have been investigated by CFD simulations [77-79], providing meaningful information for the design of heat exchangers.

### 2.4.3 Effects of heat conduction and air maldistribution

Due to the longitudinal heat conduction through fins, performance of heat exchangers can be deteriorated and therefore thermal efficiency of associated system can be reduced. The effect of heat conduction through fins for a microchannel serpentine gas cooler of a transcritical $CO_2$ air-conditioning system was investigated experimentally [80]. To analyze and compare the performance of the gas coolers with and without fin cutting, parts of fins where heat conduction was most significant were removed. As a result, the gas cooler's heating capacity was increased by up to 3.9%, while the approach temperature was decreased by between 0.9 and 1.5 K, when cutting or split fins were utilized. Similarly, the system's COP might be increased by 5% if the effect of heat conduction through fins could be reduced. Zilio et al. [81] conducted an experimental study on finned-tube $CO_2$ gas coolers with and without split fins and various tube circuit configurations. When split fins were used to the same gas cooler, it was discovered that the heating capacity and system COP could be increased by 3.7% to 5.6% and 5.7% to 6.6%, respectively. It also suggested that the diverse tube circuitry configurations in the coil could influence the effect of split fins on the coil's performance, however quantitative research is still required. Other forms of heat exchangers, such as printed circuit heat exchangers [82] and finned-tube evaporators [83-84], may also experience capacity reductions due to the negative impact of reversed heat conduction. Based on experimental findings, the increased longitudinal heat conduction through fins due to the greater superheat at the evaporator exit could deteriorate the cooling capacity of the coil with unsplit fins more than the coil with split fins [84].

Some researchers have explored numerically the effects of airflow maldistribution on heat exchanger performance [85-87]. Airflow maldistributions affected the thermal performance of heat exchangers negatively as concluded by their results. Aganda et al. [88] found that the maximum loss in heat transfer performance of evaporator affected by the air maldistribution could be up to 38%. In addition, experimental research conducted by Blecich [89] shown that under conditions of extreme airflow maldistribution, the effectiveness of heat exchangers could be reduced by up to 30%. In addition, Yaci et al. [90] presented a CFD thermal-hydraulic performance analysis on the influence of airflow maldistribution on finned-tube heat exchanger. It was discovered that Colburn j-factors could rise or drop by 50 percent under conditions of airflow maldistribution compared to conditions of uniform airflow.

## 2.5 Shell-and-tube heat exchanger

### 2.5.1 STHX classification

Generally, shell-and-tube heat exchangers (STHX) consist of a bundle of tubes mounted in a shell as demonstrated in Figure 2.8. The exchangers can be designed for high pressure up to 100MPa and high temperature up to 1100 ˚C [91]. As one of the most versatile exchangers, they have been utilized more than 65 % of the market in industries for past decades. Shell-and-tube heat exchangers can have multiple passes for tube side and different number of baffles. SHTX also can be classified as different tube arrangements, fluids flowing in same direction is named as parallel type, flowing in opposite directions is named as counter flow type, flowing normal to each other is named as cross flow type. A simple counter flow STHX consists of one shell pass and one tube pass.

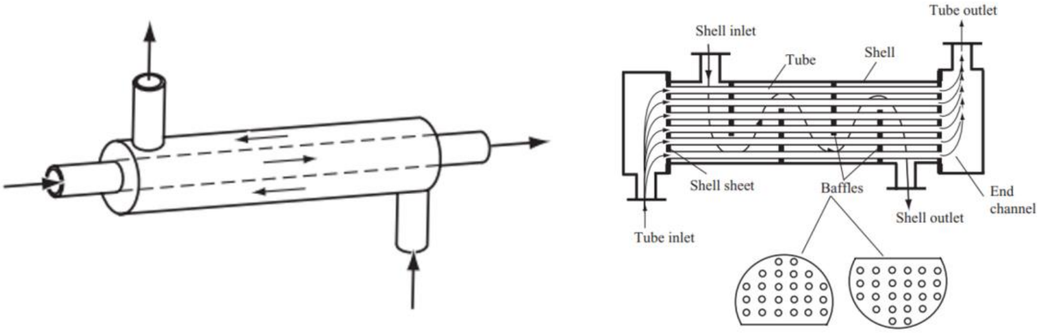

Figure 2. 8 Typical shell-and-tube heat exchangers [91].

### 2.5.2 Scopes for improvement in STHX performance

As high temperature and high pressure of the T-$CO_2$ or S-$CO_2$ power generation system, a supercritical STHX can be selected as $CO_2$ gas heater, which plays an important role in the system performance. However, the operational efficiency need to be further improved for higher thermal efficiency of associated system. Several experiments were carried out to explore the fundamental calculations of heat transfer coefficients and pressure drops of shell-and-tube heat exchangers at various design and operating conditions [92-93]. In particular, an experimental investigation was conducted by Kim and Aicher [94] to examine the heat transfer behaviors of a shell-and-tube heat exchanger by varying its structural parameters. It was found that the effect of tube pitch could be neglected. In addition, for the heat exchanger with shorter tube length, the shell-side fluid heat transfer coefficient in a tube nozzle region was much higher than those of tube parallel regions nearby. It was also proved that for a shell-and-tube heat exchanger with staggered tube arrangement, the local shell-side heat transfer coefficient near the inlet nozzle was significantly greater than those at other flow regions[95]. Furthermore, He et al. [96] found that a shell and tube heat exchanger with elliptic tubes had 14.7-16.4% higher heat transfer rate than the heat exchanger with circular tubes. On the other hand, the flow characteristics of the shell side are more complicated and difficult to be measured mainly due to the exist of baffles. The baffles are used to direct the fluid flow of shell side, prevent tube bundles from sagging and avoid the effect of vibration. The conventional segmental baffle arrangement can mostly lead to dead spaces and thus result in lower heat transfer rate [97]. To cope with this negative effect, it was proved that by increasing the number of baffles, the dead zones could be effectively eliminated [98], which however might cause higher pressure drops on shell side. Halle et al. [99] measured shell-side fluid pressure drops of shell-and-tube heat exchangers with different baffle configurations. Results showed that closer baffle spacing led to higher fluid flow velocity and enhanced heat transfer but higher pressure drop. Similar conclusions were also obtained by Sparrow and Reifschneider [100] such that higher pumping power was needed to handle the higher pressure drop. As to the effect of battle cut ratio, it could increase the heat transfer but simultaneously cause higher pressure drop [101]. Alternatively, a helically baffled shall-and-tube heat exchanger is a promising design to overcome the disadvantages of conventional segmental baffle arrangements, which has been proved experimentally and numerically[102-104].

### 2.5.3 Kern method and Bell-Delaware method

Theoretically, for estimating the performance of shell-and-tube heat exchanger, two most acknowledgeable methods by Bell-Delaware [105] and Kern [106] have been commonly used to calculate the fluid heat transfer coefficients and pressure drops on the shell side fluid flow. However, the Bell-Delaware method is more accurate to predict the heat transfer performance of shell side fluid flow since the effects of leakage and bypass streams on shell side fluid flow were taken into account. Based on the correlations and equations from Bell-Delaware method, Gaddis and Gnielinski [107] evaluated and updated the shell side pressure drop calculations. Alternatively, Jayachandriah and Vinay [108] used Kern method to design shell-and-tube heat exchangers with different baffle arrangements. Kern and Bell-Delaware methods can also be used for validations of the heat exchanger models[109-110].

## 2.6 Summary

As discussed above, it is imperative to using renewable energy and environmental-friendly working fluid for saving energy and protecting the environment. Compare to other working fluids, $CO_2$ has the competitive heat transfer and thermo-physical properties. Biomass as a renewable heat source, making great contribution to low $CO_2$ emission. S-$CO_2$ Brayton Cycle offers desirable advantages for power generation with biomass, such as high thermal efficiency, compactness devices and single phase in components. However, due to the lack of supercritical compressor in supermarket, the following chapter will propose a Biomass-$CO_2$ transcritical Brayton Cycle. The performance of this advanced energy conversion system needs to be comprehensively investigated and analyzed.

In addition, gas heater and gas cooler can significantly influence the performance of entire system. Thus, high effectiveness of heat exchangers is requested. However, for finned-tube gas cooler, very few research studies focused on the evaluation of tube side fluid heat transfer and hydraulic performance of $CO_2$ gas cooler, the majority of CFD modelling works focus on fin side fluid. Therefore, the effect of thermal conduction through fins on the temperature on the refrigerant side cannot be accurately detected.

As a consequence, a novel CFD simulation need to be carried out to provide precise $CO_2$ temperature profile along its flow direction. Furthermore, the system performance can be more accurately evaluated depending on the results of gas cooler CFD simulations. Besides, there are very few investigations on the design and operation of an actual high-temperature biomass flue gas heated supercritical $CO_2$ shell-and-tube gas heater with CFD model and their effects on the associated system performance. Subsequently, detailed CFD models for the $CO_2$ supercritical gas heater need to be developed to make contribution to optimized STHX for Brayton Cycle and better control of entire system.

Chapter 3 will present an overview on the construction of biomass-$CO_2$ transcritical Brayton cycle power generation system.

# Chapter 3 - Experimental Set-up for the Proposed Biomass-$CO_2$ Transcritical Brayton Cycle

## 3.1 Introduction

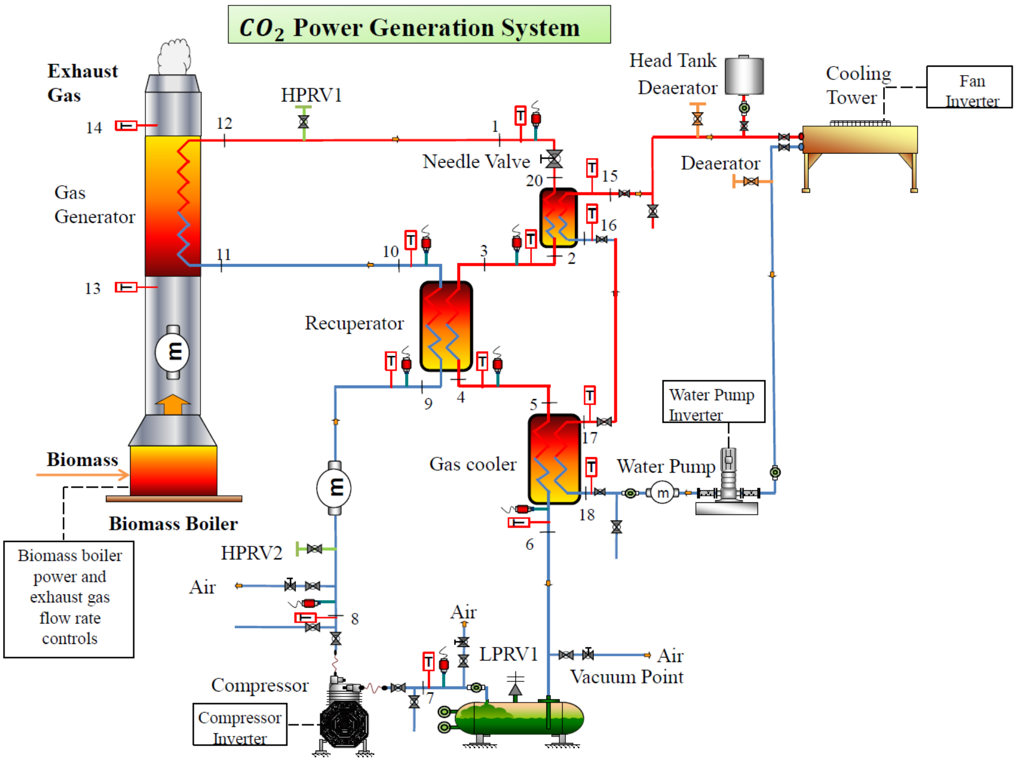

Figure 3. 1    Schematic diagram of the Biomass-$CO_2$ power generation system.

To investigate the performance of Transcritical S-$CO_2$ Brayton cycle, the biomass power generation system is designed as shown in Figure 3.1. The small-scale biomass power plant will be built using biomass boiler coupled with Brayton cycle system. In this project, wooden pellets are selected as biomass source. Wooden pellet is a kind of biomass which can make mass and energy densification. It increases bulk density and thus reduces volume. Meanwhile, it improves transport and feeding abilities. In other words, wooden pellets can improve the efficiency of biomass boiler.

## 3.2 System design and components selections

The overall test system consists of three operational loops, one open loop for biomass flue gas, one close loop for $CO_2$ thermodynamic power cycle and one close loop for cooling water.

In biomass flue gas open loop, it consists of a $100kW_{th}$ biomass boiler, a $CO_2$ gas heater, exhaust pipe, and an ejector with a air compressor to drive flue gas out of the chimney. Biomass is combusted in the biomass boiler and flue gases generated. The biomass unit was designed to produce high temperature flue gas around 800˚C. The flue gases are used to heat carbon dioxide, a working fluid in a closed transcritical carbon dioxide Brayton. In the close loop for $CO_2$ thermodynamic power cycle, it comprises of a $CO_2$ gas heater, a $CO_2$ turbine simulator (a needle and water-cooled gas cooler), a recuperator, gas cooler-2, a receiver, a $CO_2$ transcritical compressor.  It is worth mentioning that a needle valve combined with a $CO_2$ gas cooler is acted as a turbine. The receiver is applied to store any liquid from the main gas cooler and prevent any liquid flowing into the compressor.  In the close loop for cooling water, it consists of the cold sides of gas cooler-1 and gas cooler-2, a fined-tube water cooler and a water pump. The cold water from the water cooler outlet is withdrawn by the water pump and flows through the two gas coolers respectively. Figure 3.2 illustrates the main test rig of this biomass-$CO_2$ power generation system.

This system mainly focuses on transcritical region which between subcritical and supercritical regions. The $CO_2$ is in gas states without any liquid phase in the Brayton cycle. After being heated up to highest cycle temperature of 500 °C at point '1', the $CO_2$ is expanded in the turbine to generate electricity as shown in the T-S and P-h diagrams (Figure 3.3 and Figure 3.4) from point '1' to '3'. Then the working fluid releases heat through recuperator to point '4' and be furthered cooled down by gas cooler-2 to point '6'. The $CO_2$ release heat to ambient through the second water-cooled $CO_2$ gas cooler. The $CO_2$ state at the gas cooler-2 outlet is assumed to be saturated vapor. In addition to reduce $CO_2$ temperature, recuperator can also preheat the compressed $CO_2$ before it re-enters into biomass chamber. The last step is to adiabatically compress $CO_2$ through the compressor, from point '6' to '8'. The point numbers are same as the numbers in Figure 3.1. The cycle then repeats.

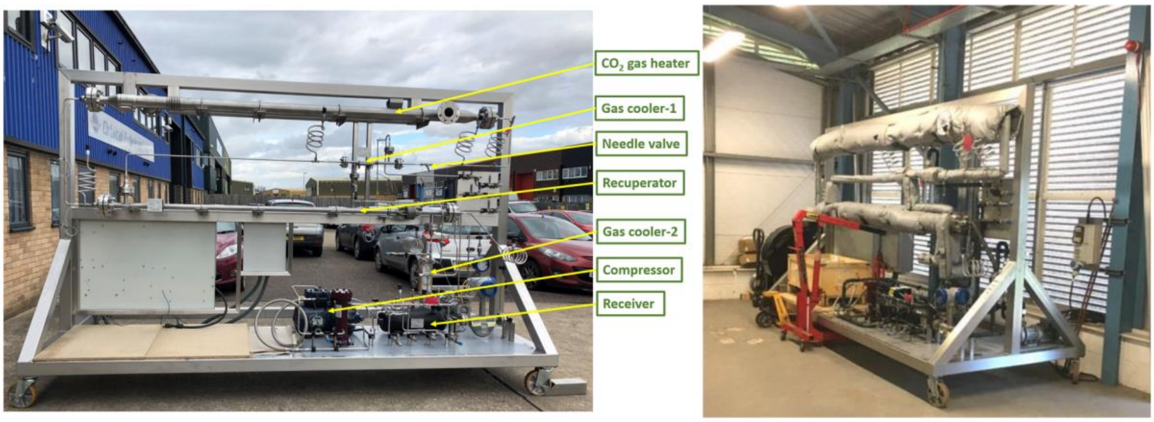

Figure 3. 2  Test rig of $CO_2$ power generation system.

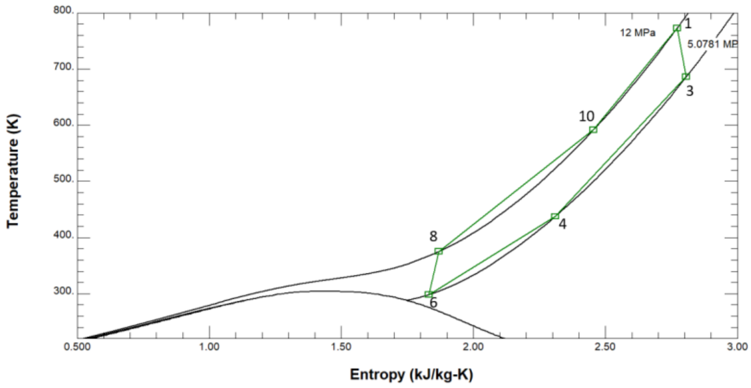

**Figure 3. 3  T-S diagram of biomass-$CO_2$ transcritical Brayton cycle.**

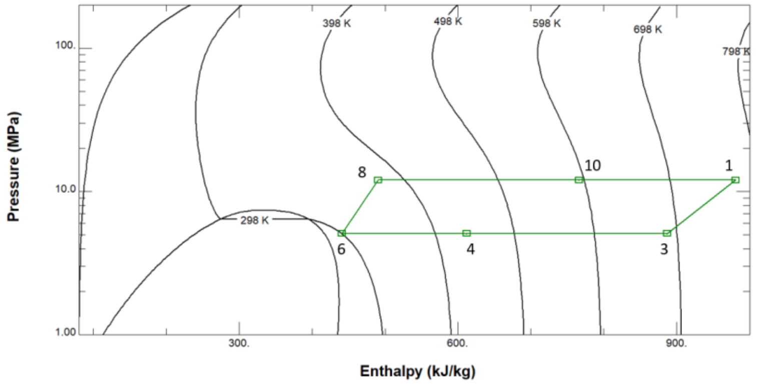

**Figure 3. 4  P-h diagram of biomass-$CO_2$ transcritical Brayton cycle.**

The biomass-$CO_2$ power generation system is designed to ensure 11.9 kW power generation. The designed conditions are specified in Table 3.1. For the specifications of the $CO_2$ expander, at design conditions, the maximum pressure applied is 120 bar and the pressure at the expander outlet is specified to 50.871 bar (subcritical) considering the high heat source and heat sink temperatures of 800 °C and 20 °C respectively. Furthermore, isentropic efficiency of expander, isentropic efficiency of compressor and effectiveness of recuperator are assumed as 0.8, 0.6252 and 0.8 respectively.

Table 3. 1 Specifications of designed conditions.

| design conditions | |
|---|---|
| working fluid | $CO_2$ |
| Critical temperature of working fluid (K) | 304.13 |
| Critical pressure of working fluid (MPa) | 7.3773 |
| Designed power generation rate from the system (kW) | 11.9 |
| Biomass flue gas temperature at $CO_2$ gas heater inlet (°C) | 800 |
| Biomass flue gas mass flow rate at $CO_2$ gas heater inlet (kg/s) | 0.12 |
| Cooling water temperature at $CO_2$ gas cooler-2 inlet (°C) | 20 |
| Cooling water flow rate at $CO_2$ gas cooler-2 inlet (kg/s) | 0.15 |
| $CO_2$ temperature at the turbine inlet (°C) | 500 |
| $CO_2$ pressure at the turbine inlet (bar) | 120 |
| $CO_2$ temperature at the compressor inlet (°C) | 25 |
| $CO_2$ pressure at the compressor inlet (bar) | 50.871 |
| Isentropic efficiency of expander | 0.8 |
| Isentropic efficiency of compressor | 0.6252 |
| Effectiveness of recuperator | 0.8 |

### 3.2.1 Biomass boiler

A 100kW$_{th}$ biomass boiler was integrated with system to provide high temperature flue gas as heat source, as shown in Figure 3.5. It is primarily consisted of combustion chamber, hopper, fan and mechanical feeding system. The shell of combustion chamber and tube nest are made of stainless steel. Insulated door was installed to inspect and clean the chamber and burner. There are primary and secondary combustion air system in the combustion chamber, which can improve the heat output from burning biomass. The hopper is used for the storage of biomass pellets. Mechanical feeding system can transfer the biomass to iron cast burner, meanwhile the feed speed can be controlled. Fan speed also can be adjusted for control the rate of combustion. The pipe on the top of the combustion chamber was connected with the shell side inlet of $CO_2$ gas heater to heat the $CO_2$ to maximum cycle temperature, as shown in Figure 3.5.

Figure 3. 5 100kWth biomass boiler.

### 3.2.2 $CO_2$ gas heater

A supercritical $CO_2$ gas heater plays an important role in the system performance as a main component in the T-$CO_2$ or S-$CO_2$ power generation system. Shell-and-tube heat exchangers have been widely applied in industries and energy systems such as refrigeration and heat pump due to their simple design, compactness, easy-to-maintain and relatively high performance. $CO_2$ flows in the tube side while the flue gas passes along the shell side. As shown in Figure 3.6, $CO_2$ gas heater is a typical counter-flow shell-and-tube heat exchanger produced by UK Exchangers Ltd. Specifications of this $CO_2$

gas heater is demonstrated in Table 3.2. The muti-tube design is ideal for heating application for steam and fluids, which also improve the thermal efficiency. Under the design conditions, the heat load of $CO_2$ gas heater is 26.86 kW.

Figure 3. 6 $CO_2$ gas heater.

Table 3. 2 Geometric parameters of the $CO_2$ gas heater.

| | |
|---|---|
| Number of inner tubes | 13 |
| Inner tube diameter | 13.70 mm |
| Inner tube thickness | 2.24 mm |
| Shell tube diameter | 101.6 mm |
| Shell tube thickness | 3.05 mm |
| Numbers of baffles | 2 |
| Heat exchanger length | 3472 mm |

### 3.2.3 Turbine

A needle valve and gas cooler-1 were combined to act as a turbine simulator. The Swagelok needle valve SS-3NBS4-G is shown in Figure 3.7(a). This severe-service union-bonnet needle valve is made of 316 stainless steels. Its temperature ranges from -53 °C to 648 °C, and its pressure up to 118 bar at highest temperature of 648 °C. The valve flow coefficient is 0.86, which can be controlled by different number of turns open. The

$CO_2$ gas cooler-1 is a shell-and-tube heat exchanger as shown in Figure 3.7(b), the specifications of $CO_2$ gas cooler-1 is shown in Table 3.3. $CO_2$ flows through tube side and water flows through shell side. Under the design conditions, the heat load of $CO_2$ gas cooler is 11.45 kW.

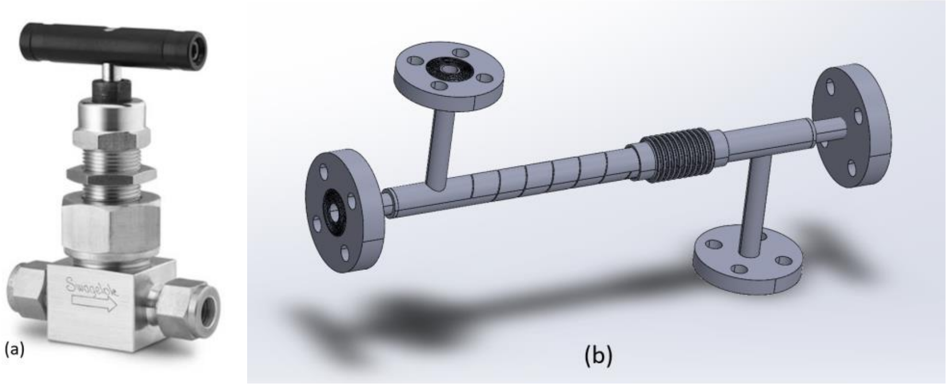

**Figure 3. 7 (a) Needle valve; (b) $CO_2$ gas cooler-1.**

**Table 3. 3 Geometric parameters of the $CO_2$ gas cooler-1.**

| | |
|---|---|
| Number of inner tubes | 1 |
| Inner tube diameter | 18 mm |
| Inner tube thickness | 1 mm |
| Shell tube diameter | 25 mm |
| Shell tube thickness | 1.5 mm |
| Heat exchanger length | 494 mm |

### 3.2.4 Recuperator

A counter-flow recuperator was installed in this system in purpose of energy recovery, in which the heat is transferred from hotter $CO_2$ to colder $CO_2$, as shown in Figure 3.8. It has been proved that installation of recuperator is an effective way to save energy and to improve thermal efficiency. The recuperator used in this system is produced by UK Exchangers Ltd. Geometric parameters of this recuperator are illustrated in Table 3.4. The capacity of this recuperator is 34.52 kW at the design conditions.

Figure 3. 8 Recuperator.

Table 3. 4 Geometric parameters of the recuperator.

| | |
|---|---|
| Number of inner tubes | 7 |
| Inner tube diameter | 18 mm |
| Inner tube thickness | 1.5 mm |
| Shell tube diameter | 33.7 mm |
| Shell tube thickness | 2.77 mm |
| Heat exchanger length | 3034 mm |

### 3.2.5 Water-cooled gas cooler

For releasing the heat from $CO_2$ and also providing heating, a plate type heat exchanger produced by SWEP is selected for the water cooling loop, which is gas cooler-2 in Figure 3.1. In this counter-current gas cooler, the hot side fluid is $CO_2$ and the cold side fluid is water. The geometry and photograph are shown in Figure 3.9. For the hot side, there are 12 channels, and there are 13 channels for cold side. Total number of plates is 26. The gas cooler has total heat transfer area of 0.984 $m^2$. Under the design conditions, heat load of the water-cooled gas cooler is 25 kW.

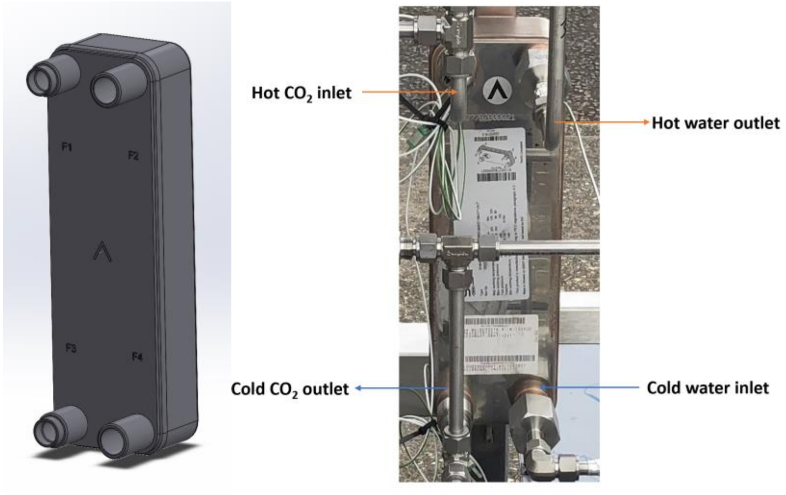

Figure 3. 9 Gas cooler-2.

### 3.2.6 $CO_2$ receiver

After $CO_2$ flows through gas cooler-2, a horizontal receiver with 20 litres was installed before it comes into the compressor. First, it can collect working fluid when the system is shut down. Second, it can separate liquid and gas, ensuring only vapour $CO_2$ follows into compressor without liquid. The mode number of this receiver is HR-2585-03, which is manufactured by Stanref International Ltd as seen in Figure 3.10. The temperature range is from -50 ˚C to 35 ˚C. Its design pressure is 90 bar. The inlet port and outlet port are on the top of the receiver, and the low-pressure relief valve was located between the two ports.

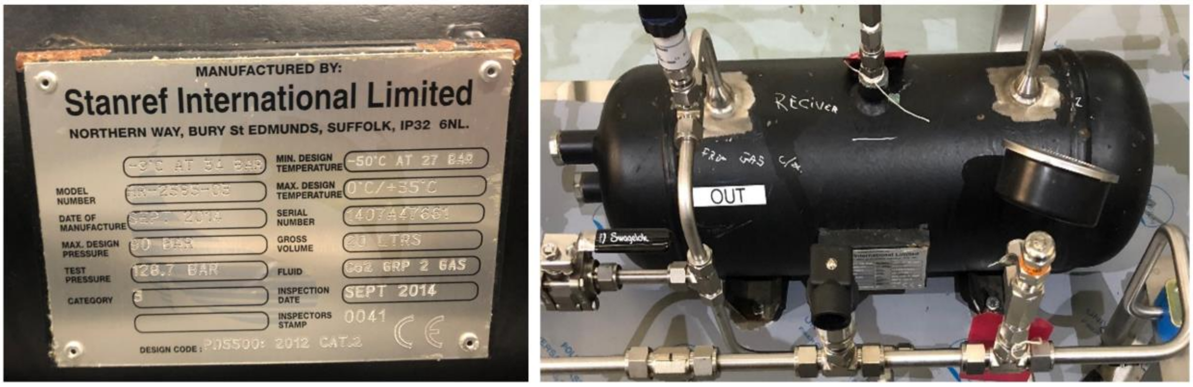

Figure 3. 10 $CO_2$ receiver.

### 3.2.7 $CO_2$ transcritical compressor

Due to there is no supercritical compressor available in current market, a transcritical compressor was employed and installed in the system. The compressor type is Dorin CD700H reciprocating compressor with swept volume 4.34 $m^3$/h, as shown in Figure 3.11. The evaporating temperature is 15 ˚C and the superheat temperature is 10 ˚C. Therefore, the compressor is designed to perform from low pressure of 50.871 bar to high pressure of 120 bar. The voltage, phase and frequency are 380-420 V, 3 phase and 50 Hz respectively. The power consumed by this $CO_2$ transcritical compressor is 7.3 kW at design conditions. it can be seen in Figure 3.11, there was an oil separator installed after $CO_2$ flow through the compressor to separate oil and $CO_2$.  Model 133A type manufactured by Temprite was selected.  The 130 Series of coalescent oil separators are designed and optimized specifically for transcritical $CO_2$ systems, which is suitable for $CO_2$ transcritical high-medium and low-temperature applications. The maximum operating pressure is 140 bar with nominal 98.5% separation efficiency rating.

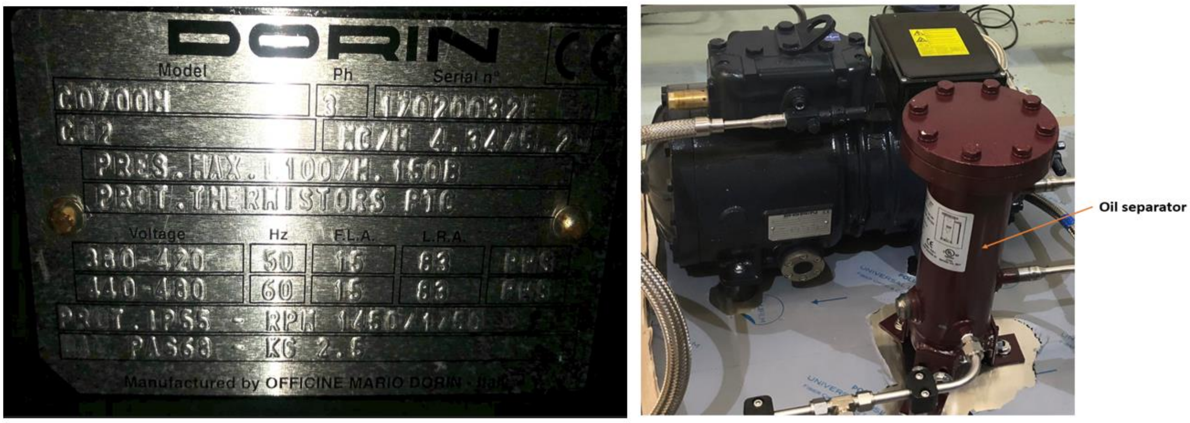

Figure 3. 11    Specifications of $CO_2$ transcritical compressor.

The variations in compressor isentropic and volumetric efficiency with $CO_2$ pressure ratios of compressor outlet and inlet can be estimated using manufacturer-provided compressor performance data and are depicted in Figure 3.12, respectively. Correspondingly, the isentropic efficiency and volumetric efficiency can be correlated as following equations:

$$\eta_{isentropic} = -0.0141R_p^2 + 0.0793R_p + 0.5603 \tag{3.1}$$

$$\eta_{volumetric} = -0.059R_p + 0.9458 \tag{3.2}$$

It can be observed that, with the pressure ratio increases, isentropic efficiency increases firstly. Then it decreases with further increasing the pressure ratio. In other words, there is an optimal value of pressure ratio that leads to the highest isentropic efficiency. The volumetric efficiency decreases mostly linearly with the increase in pressure ratio.

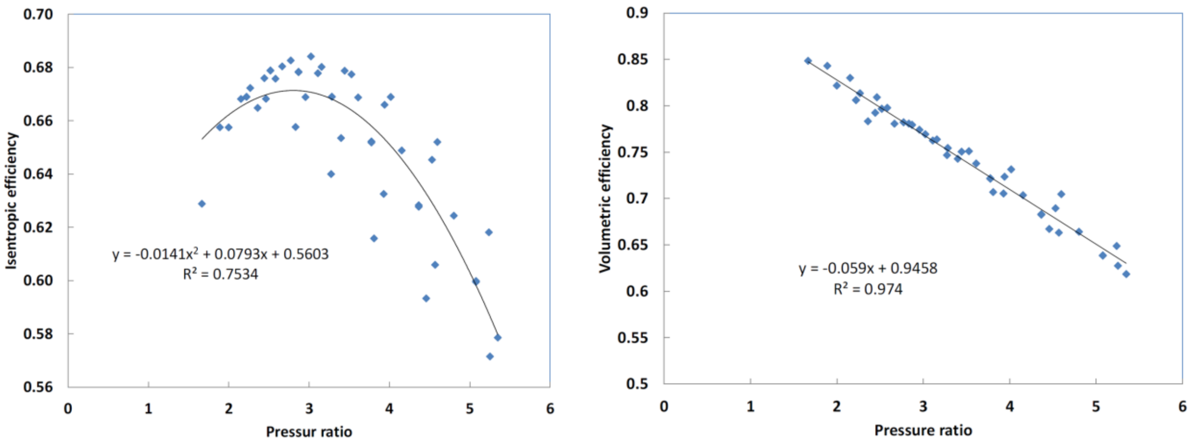

**Figure 3. 12 Variations of compressor isentropic efficiency and volumetric efficiency with compressor ratios.**

### 3.2.8 Ejector and air compressor

The ejector which was installed between the exhaust pipe and the chimney was employed to cover the pressure losses of flue gas flow through the $CO_2$ gas heater, as shown in Figure 3.13 The flue gas ejector was manufactured by Bamford & Morris Ltd, which is made of 316 stainless steel. The molecular weight of motive gas is 28.9 MolWt, the molecular weight of suction gas is 66.5 MolWt. For providing high pressure motive air to flow through the nozzle, screw compressor Renner RSD 11.0-10 was used. Specifications of the air compressor is illustrated in Figure 3.14.The motor power of this compressor is 11 kW; the productivity of it is 1500 L/min; operating pressure of it is 10 bar. After the $CO_2$ gas heater, the flue gas flow then can be withdrawn by the ejector and exhausts to ambient through the chimney.

Figure 3. 13 Flue gas ejector and the chimney.

Figure 3. 14 Air compressor.

### 3.2.9 Finned-tube water cooler and water pump

Finned-tube heat exchanger is typically used in industries due to its characteristics of simplicity, durability and versatility. Correspondingly, finned-tube water cooler was used for cooling $CO_2$ in this system. As seen in Figure 3.15, the whole water cooler is consisted of three smaller finned-tube water coolers. On the top of the cooler, there are three fans, by varying fan speed to control the water and $CO_2$ temperature. As the $CO_2$

temperature is an significant parameter affecting the efficiency of entire system, the performance of finned-tube heat exchanger plays an important role in this $CO_2$ transcritical Brayton cycle. Therefore, comprehensive parameters on this type of heat exchanger should be investigated. For pumping cold water into cooling loop, a water pump manufactured by SPECK PUMPEN with type of TOE-CY-6091.0039 SPECK PUMPEN was used in this system as seen in Figure 3.16. The water pump was driven by an electrical motor with power rating of 2.8 kW at 2800 rpm. The speed of the water pump can be controlled by a frequency drive inverter by adjusting the flow rate of water.

Figure 3. 15 Finned-tube water cooler.

Figure 3. 16 Water pump.

### 3.2.10 Auxiliary components

½” Swagelok SS-83PS8 Ball Valves are used for charging and discharging $CO_2$, as seen Figure 3.17(a). These ball valves were also used to isolate the system. Its maximum temperature can be reached to 232 ˚C at 34.4 bar.

For controlling the flow rate of cooling water, a Swagelok SS-6NBS8 stainless steel severe service union bonnet needle valve was installed, as seen in Figure 3.17(b). The minimum and maximum temperature of this needle valve is -53 ˚C and 232 ˚C, maximum temperature pressure rating of 284 bar. Flow coefficient of 0.86 was selected.

Due to flanges are frequently used in this system, gaskets were used between two flange faces to save energy.  The type of NOVUS TI (Tanged) gaskets were used for high temperature flanges as seen in Figure 3.17(c), it is suitable for maximum temperature of 500 ˚C at 120 bar. The type of NOVUS 30 gas gaskets were used for relatively low temperature flanges as seen in Figure 3.17(d), the maximum temperature and maximum pressure are 400 ˚C and 80 bar.

(a) SS-83PS8 Ball Valve (a) SS-6NBS8 needle valve (c) Novus TI (d) Novus 30

Figure 3. 17 Swagelok ball valve, Swagelok needle valve and gaskets.

## 3.3 Leakage test

As shown in Figure 3.18(a), to ensure that there is no leakage in the test rig of the $CO_2$ power generation system, high-pressure and low-pressure tests were conducted. For the high-pressure test, Argon was charged to 120 bar between the compressor outlet and needle valve inlet on the high-pressure side of the system. As shown in Figure 3.18(b), the high pressure was sustained at 120 bar for 30 minutes, proving that there is no leakage on the high-pressure side. For the low-pressure test, 50 bar of Argon was introduced between the needle valve outlet and compressor inlet on the low-pressure side of the system. As shown in Figure 3.18(c), the low pressure was maintained at 50 bar for 30 minutes, proving that there is no leakage on the low-pressure side.

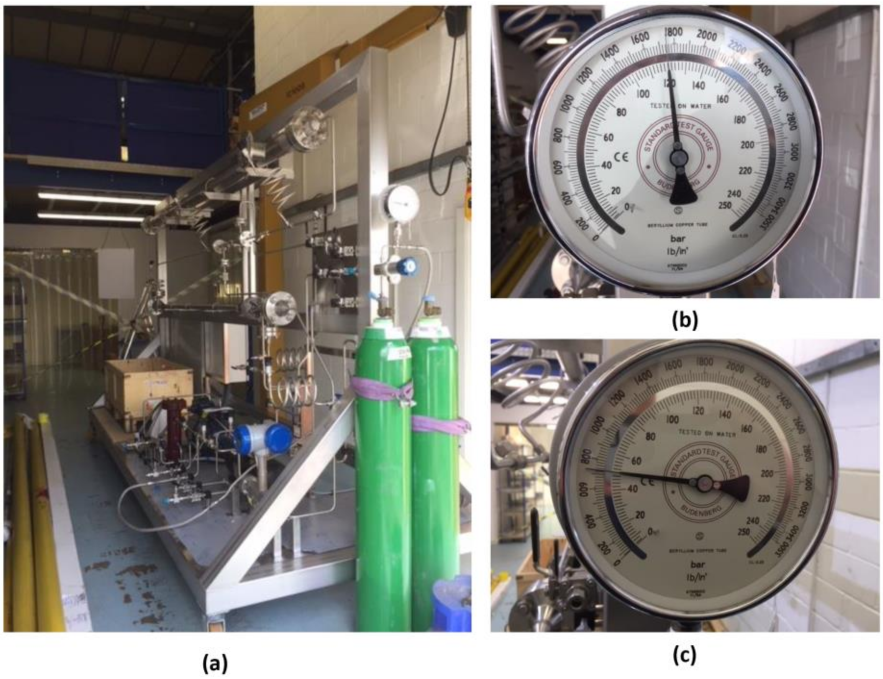

(a)

(b)

(c)

Figure 3. 18 (a) Pressure test on the test rig of $CO_2$ transcritical power generation system; (b) Gauge pressure for 120 bar test; (c) Gauge pressure for 50 bar test.

## 3.4 Control strategies

### 3.4.1 System operation controls

There are some parameters need to be controlled for this $CO_2$ power generation system, including $CO_2$ mass flow rate, turbine inlet temperature and pressure, compressor inlet temperature and pressure. By modulating biomass capacity, the $CO_2$ high-temperature side can be controlled due to the flue gas temperature and mass flow rate are relatively adjusted. By modulating compressor motor frequency and needle valve opening to control pressure ratio, thus the mass flow rate of $CO_2$ and highest pressure can be controlled. By modulating the capacity of water cooler via adjusting water pump speed, fan speed and water needle valve to control the compressor inlet temperature. Control strategies are summarized in the following Table 3.5.

**Table 3. 5 Control parameters and control devices.**

| Control Parameters | | Control components |
|---|---|---|
| $CO_2$ mass flow rate | | $CO_2$ compressor and $CO_2$ needle valve |
| $CO_2$ high pressure side | Pressure | $CO_2$ compressor |
| | Temperature | Biomass boiler |
| $CO_2$ low pressure side | Pressure | $CO_2$ Needle valve |
| | Temperature | Water pump, water cooler and water needle valve |

### 3.4.2 Safety controls

To ensure system safety operation, a high-pressure switch and a low-pressure switch were installed on this system. Two MBC-5100 Danfoss pressure switches with regulation range of 16 bar to 160 bar were utilized as shown in Figure 3.19. They are used to stop the compressor when the suction pressure drops below 50.871 bar and discharge pressure increases above 120 bar. Once the pressure switches are on, the electricity of system will be shut down and $CO_2$ will be released through pressure relief valves.

Figure 3. 19 Pressure switches.

Figure 3. 20 Pressure relief and spiral cooling coil.

Meanwhile, two high pressure relief valves and one low pressure relief valve were installed for safety considerations. One of the high-pressure relief valves (HPRV) was installed between $CO_2$ gas heater and $CO_2$ needle valve, the other one was installed between recuperator and compressor. The low-pressure relief valve (LPRV) was installed on the receiver, which is between compressor and gas cooler-2. The Swagelok SS-4R3A1 proportional relief valves with maximum temperature of 148˚C were used. For using this type relief valve safely in high temperature range, high temperature adapter should be connected before hot fluid flows into relief valves. Therefore, we used spiral cooling coils to reduce measurement temperature as seen in Figure 3.20.

### 3.4.3 Control system

The control system included an electrical control system and electronic control system, as shown in Figure 3.21. The primary purpose of the electrical control system was to connect or disconnect the power supply to each electrical component and the electronical control system. This control system is primarily used to regulate the mass flow rate of cooling water and the compressor outlet pressure by employing an integrated controller. The electronic controller was comprised of a main controller system (RDM PR0650-TDB) with multiple communication modules and a touchscreen display. There were two frequency drive inverters installed on this panel to achieve the control of the water pump and $CO_2$ compressor. The water pump can be inverter controlled via a potentiometer, and the actual frequency output can be displayed on screen. Similarly, the transcritical $CO_2$ compressor can be manually controlled by adjusting attached inverter.

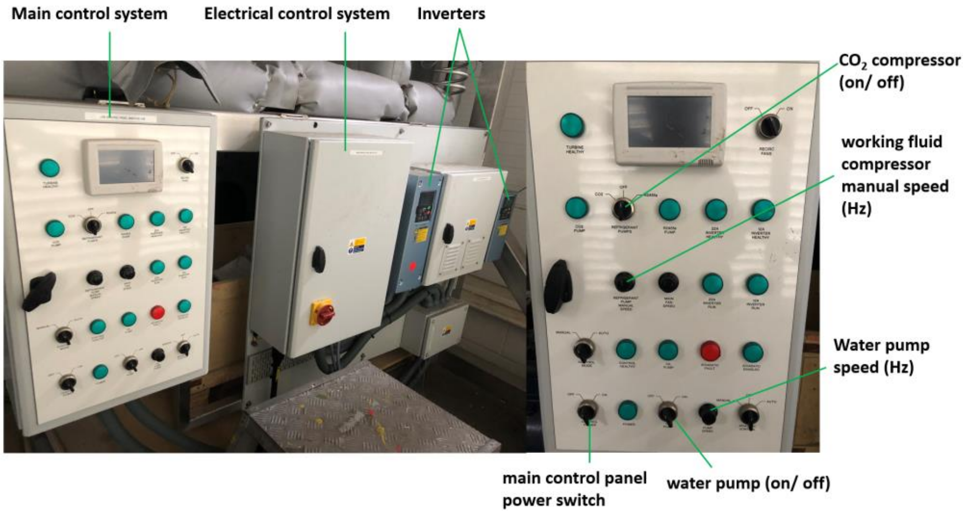

Figure 3. 21 Electrical control panel of Biomass-$CO_2$ power generation system.

## 3.5 Instrumentation and data logging system

For monitoring the stats of different location of system, thermocouples, pressure transducers, flow meters and data logger were selected.

### 3.5.1 Temperature measurement – thermocouples

There were two types of thermocouple used in this system, one is for low temperature, another one is for high temperature. There were total 20 thermocouples used. For low temperature, K-type thermocouples with temperature range of -10 ˚C – 400 ˚C and accuracy of ± 1.5 ˚C were selected, as shown in Figure 3.22 (a). For high temperature, K-type thermocouples with maximum temperature up to 900 ˚C and accuracy of ± 2.5 ˚C were utilized, as shown in Figure 3.22 (b). All thermocouples were calibrated using a calibration bath and a precision thermometer (ASL type F250MK II, probe J100-250-10-NA) with accuracy of ±0.04 ˚C. The calibrated equations for thermocouples are shown in Appendix A.

(a) (b) (c)

Figure 3. 22 (a) low temperature K-type thermocouple, (b) high temperature K-type thermocouple, (c) Swagelok pressure transducer.

8 Swagelok pressure transducers were installed on system to measure $CO_2$ pressure at different points.  Pressure transducers have measurement range of 0-160 bar, and converted the measured value 4-20 mA output signal to the data logging system, as shown in Figure 3.22 (c).

### 3.5.2 Flow meters

In this biomass-$CO_2$ transcritical Brayton cycle, KROHNE OPTIMASS 6400 C mass flow meter with measurement range of 0-0.3 kg/s was installed for measuring $CO_2$ flow rate, which has measurement accuracy of ± 0.35%, as shown in Figure 3.23 (a). KROHNE H250 M40 mass flow meter with measurement range of 0-0.3 kg/s was installed for measuring cooling water flow rate, as seen in Figure 3.23 (b). The measurement accuracy of it is ±0.25%. Both of them provide a current output signal of 4-20mA, which should be connected to data logging system directly.

(a) (b)

Figure 3. 23 (a) $CO_2$ mass flow rate, (b) water mass flow meter.

### 3.5.3 Data logging system

All measured experimental data should be transmitted by a National Instruments (NI) data logger system and automatically recorded by a computer running LabView software so that they could be viewed and recorded for evaluation and analysis of system. CompactDAQ-9188 chassis controls the timing, synchronization, and data transfer between C Series module an external host, which is featured an Ethernet connection with computer. NI-9203 module was used to connect pressure transducers and mass flow rate to collect data. NI-9214 module was used to connect thermocouples, as seen in Figure 3.24.

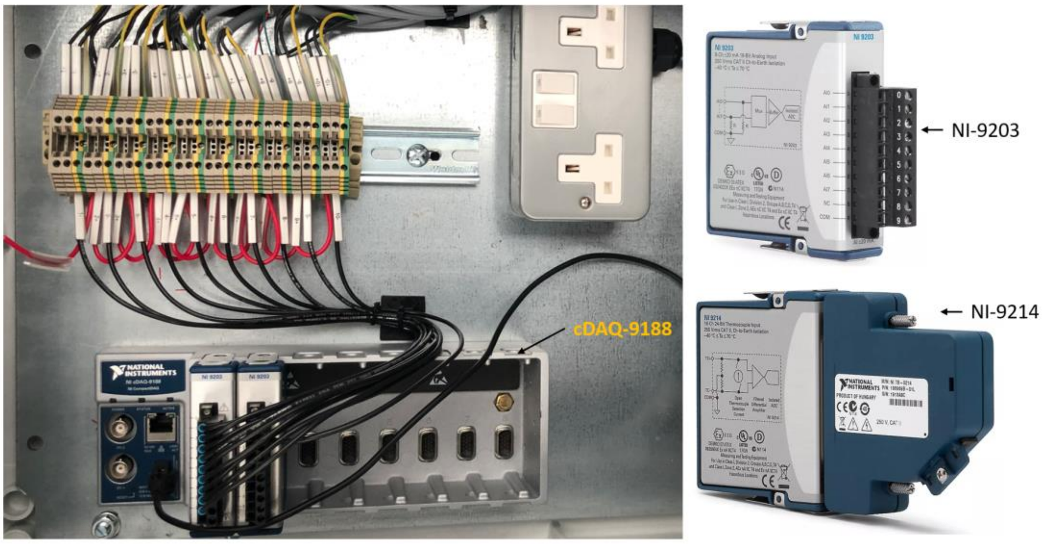

Figure 3. 24 Data logger.

## 3.6 Summary

This chapter provides detailed description of the power generation and heat recovery from biomass with advanced $CO_2$ thermodynamic systems. A small-scale test system has been designed and constructed with purposely selected and manufactured system components. All individual component used in this system has been detailed outlined. These include a biomass boiler, a $CO_2$ supercritical heater, a $CO_2$ turbine simulator, a $CO_2$

recuperator, a $CO_2$ gas cooler, a $CO_2$ transcritical compressor, a water pump, a finned-tube water cooler, the control system and all measurement devices. For fully controlling the system, control strategies and control system have been introduced.

It is known that the performance of this biomass-$CO_2$ transcritical can be modified and improved by several aspects such as controls and component operational performances. These could include the improvement of heat exchangers in system. A $CO_2$ plate heat exchanger was selected for cooling $CO_2$, and a finned-tube water cooler was selected for cooling loop, which play important roles for compressor performance and thus system performance can be further influenced. Finned-tube cooler has been widely used in industries, which could be a possible way to replace the $CO_2$ plate heat exchanger to finned-tube gas cooler to release $CO_2$ temperature into ambient in this system. Due to Covid 19, experiments were not carried out.  There is no experimental data for this specified water finned-tube cooler, a same type of finned-tube cooler was modelled and validated with published literature to comprehensively investigating and better understanding its performance. The following **chapter 4** will present a detailed CFD simulations of finned-tube $CO_2$ gas cooler. A novel CFD simulation method for finned-tube heat exchanger will be proposed, and the effects of different parameters will be discussed.

# Chapter 4 – Advanced CFD Simulation of Finned-tube $CO_2$ Gas Cooler

## 4.1 Introduction

In this chapter, a finned-tube $CO_2$ gas cooler was numerically modelled by using Computational Fluid Dynamic (CFD) method with the commercial package ANSYS Fluent, which has been published as a journal paper in Applied Thermal Engineering during my PhD study. Therefore, this chapter is a slightly modified version of Zhang et al. [111] published in Applied Thermal Engineering. The modelling process can be divided into three parts, including pre-process, CFD pre-processing, CFD solver and post-processing. In the pre-processing, geometry model was built and meshed. CFD-solver process included model selection, setup of materials, boundary identification, set up of solution methods and running simulations. In the post-processing, data were collected, and results analyzed. Due to the lack of experimental data, CFD results were validated with published literature by using the same finned-tube $CO_2$ gas cooler to investigate its performance and also the associated system.

A one-dimensional (1D) CFD numerical model is a promising method to investigate the performance of finned-tube gas cooler due to simplified coil geometry and largely reduced computing time. However, the 1D model cannot capture the temperature gradients or profiles vertical to the flow direction in the pipe and detect the heat conduction between two pipes through connected fins. On the other hand, a three-dimensional (3D) model divides the whole heat exchanger into a large number of elements, applies and solves the mass, energy and momentum conservation equations for each element by using finite volume method. It is important to note that the 3D CFD model is more precise and can capture most heat exchanger features. However, for the finned-tube $CO_2$ gas cooler to be investigated, a full-scale 3D CFD model alone is not an effective and applicable method to complete the model simulation considering of the complicated coil geometry and remarkable computation time.

Consequently, a coupled 1D-3D CFD numerical model is proposed and developed to analyze the performance of $CO_2$ finned-tube gas coolers at different operating conditions. This can be a feasible modelling method to ensure comprehensive and accurate simulation results and simultaneously maintain reasonable computing time. In this study, the whole modelling procedure is divided into phase Ⅰ model and phase Ⅱ model. In both models, 1D model developed by C language is used to customize thermo-physical properties and calculate heat transfer coefficient of $CO_2$ according to empirical correlations from published literature. The $CO_2$ thermo-physical properties of density, viscosity, specific heat capacity and thermal conductivity are all functions of temperature and pressure, which are obtained from REFPROP 8.0 software and then written in the C language program. For the fins and air flow, the fin surface temperatures and air flow parameters vary in three dimensions such that a 3D CFD model is necessarily employed. These models are then processed by a routine that couples 1D model and 3D CFD model to predict the overall performance of gas cooler.

## 4.2 Numerical methodology

In detail, the modelling route firstly starts from airside to calculate the airside heat transfer coefficient, in which fluid flow and heat transfer are processed in a passage between two consecutive fins in phase I model. The calculation is based on the conservation equations applied of mass, momentum and energy. Then, the simulation route turns into phase II model including 10 fins, airside heat transfer coefficient of each grid achieved from phase I model are assigned to surface of fins and tubes of phase II model as boundary conditions, method can be seen in Appendix B. In this case, the number of mesh elements of each fin in phase II model should be same as that of phase I model such that heat transfer coefficient of each grid can be perfectly matched. During the simulation process, a routine written in C ( as seen in Appendix B) was loaded into ANSYS FLUENT 18.2 by User Define Function that each pipe is divided into a number of segments to calculate tube side heat transfer rate, refrigerant heat transfer coefficient and refrigerant temperature for each segment. The refrigerant temperature of one tube segment can be used as the input for its next segment based on its pressure, physical-thermal properties and mass flow rate. The calculation run through each number of pipes along the refrigerant path. As inlet temperature and mass flow rate of refrigerant is known, the other temperature could be updated in each iteration and finally converged by setting up energy conservation equation. Consequently, $CO_2$ temperature profile and the temperature distributions of fin surface as well as the velocity distribution of air domain can be computed by this 1D-3D CFD simulation method. The following governing equations are employed for the present study.

Conservation of mass:

$$\frac{\partial u}{\partial x}+\frac{\partial v}{\partial y}+\frac{\partial w}{\partial z}=0 \qquad 4.1$$

Conservation of momentum:

$$\rho\left(u\frac{\partial u}{\partial x}+v\frac{\partial u}{\partial y}+w\frac{\partial u}{\partial z}\right)=-\frac{\partial P}{\partial x}+\mu(\frac{\partial^2 u}{\partial x^2}+\frac{\partial^2 u}{\partial y^2}+\frac{\partial^2 u}{\partial z^2}) \qquad 4.2$$

$$\rho\left(u\frac{\partial v}{\partial x}+v\frac{\partial v}{\partial y}+w\frac{\partial v}{\partial z}\right)=-\frac{\partial P}{\partial y}+\mu(\frac{\partial^2 v}{\partial x^2}+\frac{\partial^2 v}{\partial y^2}+\frac{\partial^2 v}{\partial z^2}) \qquad 4.3$$

$$\rho\left(u\frac{\partial w}{\partial x}+v\frac{\partial w}{\partial y}+w\frac{\partial w}{\partial z}\right)=-\frac{\partial P}{\partial z}+\mu(\frac{\partial^2 w}{\partial x^2}+\frac{\partial^2 w}{\partial y^2}+\frac{\partial^2 w}{\partial z^2}) \qquad 4.4$$

Conservation of energy:

$$\rho C_p\left(u\frac{\partial T}{\partial x}+v\frac{\partial T}{\partial y}+w\frac{\partial T}{\partial z}\right)=\frac{\partial}{\partial x}\left(k\frac{\partial T}{\partial x}\right)+\frac{\partial}{\partial y}\left(k\frac{\partial T}{\partial y}\right)+\frac{\partial}{\partial z}\left(k\frac{\partial T}{\partial z}\right) \qquad 4.5$$

### 4.2.1 Physical model

A typical staggered $CO_2$ finned-tube gas cooler depicted in Figure 4.1 is selected and investigated. The air flow passes from right to left and refrigerant flows into the top tube numbered '0' and out from the bottom tube numbered '53'. Table 4.1 shows the specification of the coil parameters.

The CFD model is developed based on the following assumptions:

- The model is developed under steady state condition.
- The actual raised lance fins are simplified as plain fins.
- A small coil element consists of two consecutive fins and connected short tubes as well as associated air domain which are used to calculate local airside heat transfer coefficient of each short tube.
- Air flow hydraulic behaviors between each small coil element is assumed the same under the consideration of symmetrical geometry.

- The refrigerant temperature does not change when it flows within a short distance.

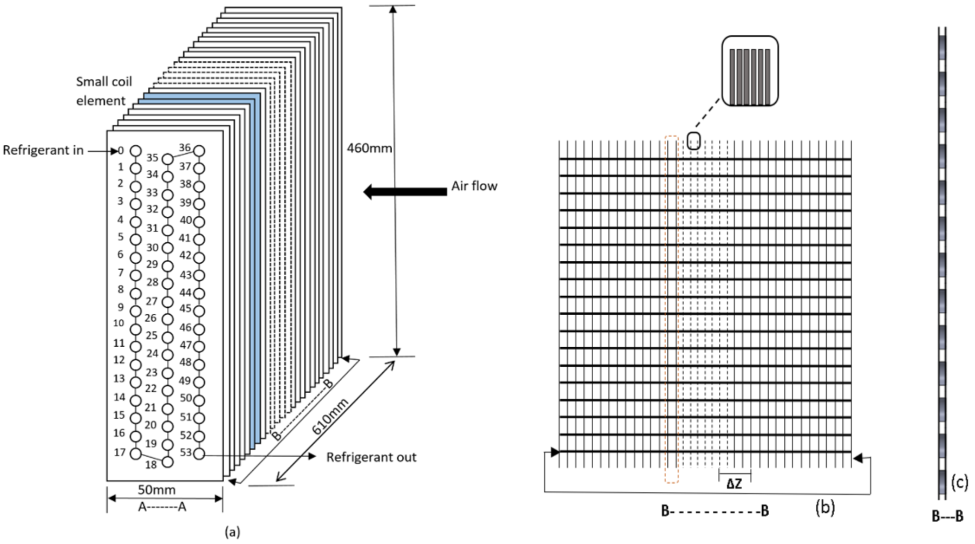

Figure 4.1 The geometry of simulated gas cooler.

Table 4.1 Specification of the modelled gas cooler.

| Dimensions | Value |
|---|---|
| W × H × D (m) | $0.61 \times 0.46 \times 0.05$ |
| $A_f$ ($m^2$) | 0.281 |
| $f_p$(mm) | 1.5 |
| $f_t$(mm) | 0.13 |
| N | 3 |
| $D_o$ (mm) | 7.9 |
| $D_i$(mm) | 7.5 |
| Tube shape | smooth |
| Fin shape | Raised lance |

### 4.2.2 Working fluid properties

$CO_2$ thermal physical properties were obtained from REFPROP 8.0. Due to the thermal-physical properties of $CO_2$ used in visual studio are the function of temperature and pressure. The properties variations with different temperature and pressure are shown in Figure 4.2.

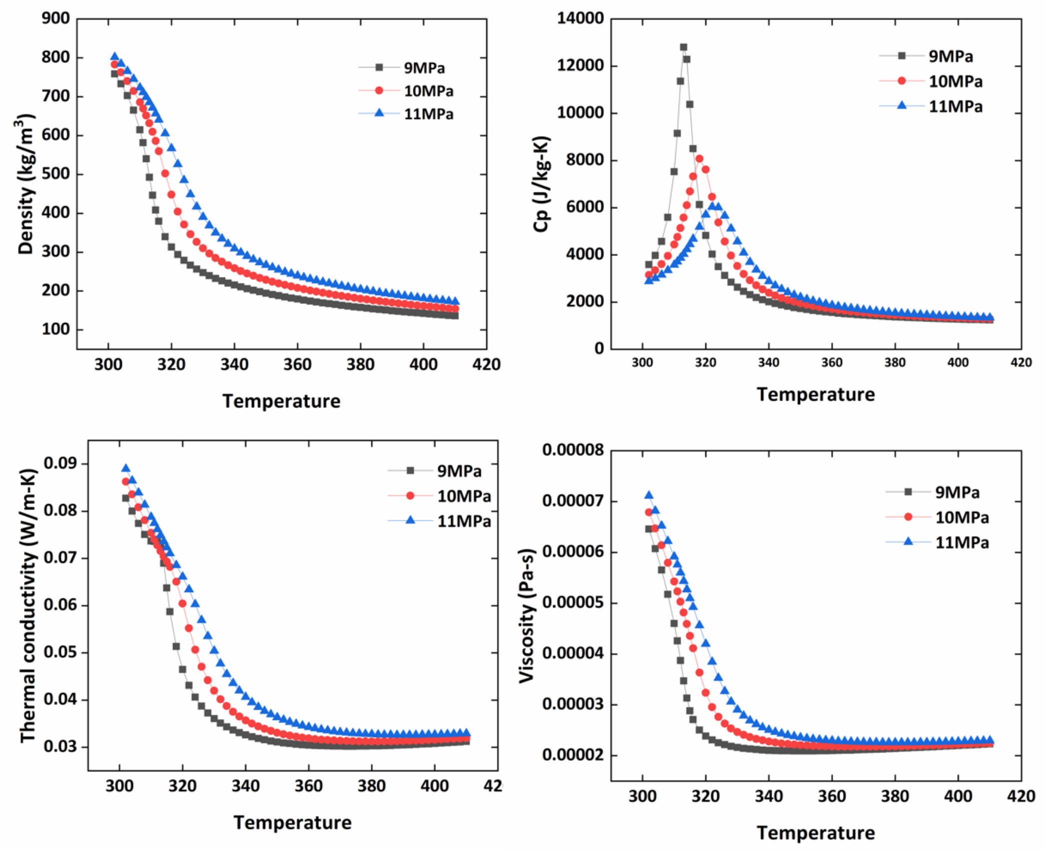

Figure 4. 2 Density, specific heat, thermal conductivity and viscosity of $CO_2$ at different pressure.

### 4.2.3 1D-3D CFD model: Phase I

In phase I model, as shown in Figure 4.1, a small coil element containing two adjacent fins and connected short tubes as well as air domain is purposely selected to calculate airside heat transfer coefficient. The coil element highlighted in Figure 4.1 has two fins and a number of short tubes between them, as shown in Figure 4.1 (c). This model is built in SolidWorks 2017. Then the 3D geometry of this model in STEP format is imported to ANSYS ICEM CFD 18.2 while in ICEM each part of the geometry is named. The geometry is meshed using hexahedral type elements as shown in Figure 4.3. There exists an air fluid domain to model the airside heat transfer and flow characteristics. Meshing is an important step for pre-processing simulation since the quality of mesh could significantly influence the accuracy of simulation results, each element of the mesh holds specific solutions of the conservation equations applied. The detailed mesh specification can be seen in Table 4.2.

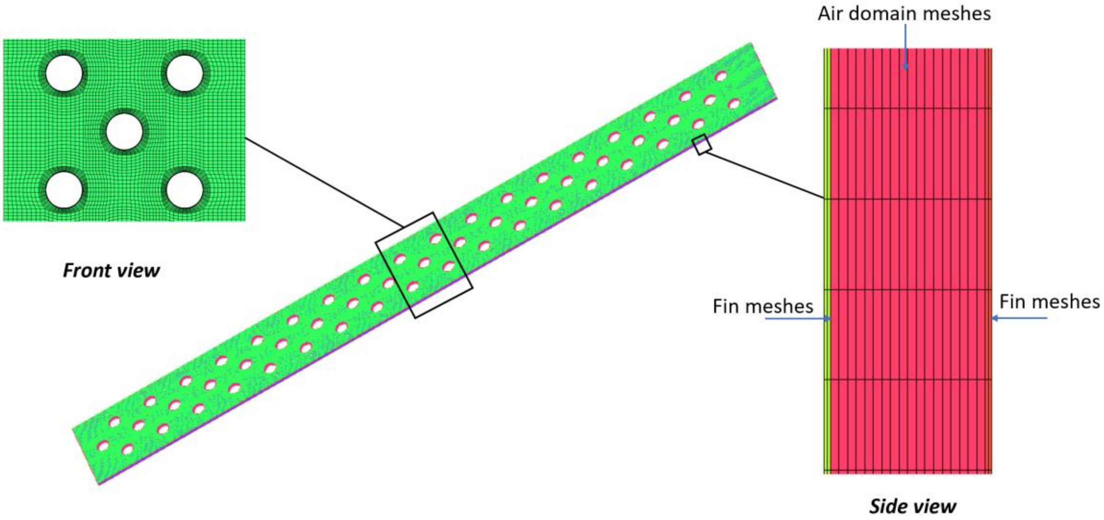

Figure 4. 3 Meshing of Phase I model.

Table 4.2 Specification of CFD model meshes.

| Parameters | Phase-I model | Phase-II model |
|---|---|---|
| Mesh type | hexahedral | hexahedral |
| Number of elements | 1370572 | 3132924 |
| average aspect ratio | 0.97 | 0.97 |
| average skewness | 0.64 | 0.64 |
| average orthogonal quality | 0.89 | 0.89 |

For each smaller element, the airside model is applied to solve the mass, momentum and energy equations at a steady state heat transfer condition. Heat transfer coefficient is an important parameter to calculate the convective heat transfer between solid tube surface and heat transfer fluid (airflow). For the selected phase I model, the local airside heat transfer coefficient can be determined by the heat flux and temperature difference between tube outer surface and incoming air flow. If air inlet average temperature is used for the heat flux calculation of each tube, the heat transfer coefficient near the second and third tube rows could be inaccurate. The reason is primarily caused by the larger air temperature changes when flowing through fins. The feasible method is to use air bulk temperatures in different sections to obtain various heat transfer coefficients. A modified method for obtaining heat transfer coefficient of each particular point using the results of CFD model contains two consecutive fins and an air domain. In this method, local airside heat transfer coefficient is determined by air temperature distribution in fluid domain. The total air temperature increase equals to the summation of temperature increases over the first row, the second row and the third row. Air temperatures along the gas cooler are changed through three sections, which are section 0, section 1 and section 2. The evaluation planes between two consecutive fins are assumed to obtain the average air temperature of $T_{1,air}$ and $T_{2,air}$, as shown in Figure 4.4. The local heat transfer coefficient is determined by the temperature difference between surface and average temperature of different sections.

The airside heat transfer coefficient at each particular point is calculated as:

$$HTC_{a,i} = \frac{Q_{a,i}}{A_i(T_{w,i} - T_{a,average})} \quad 4.6$$

The Colburn j-factor is expressed as:

$$\mathrm{j} = \frac{Nu}{Re_{in} Pr^{1/3}} \quad 4.7$$

The fanning f-friction factor is defined as the ratio of sheer stress and flow kinetic energy density, relating to the pressure drop of air in passages:

$$\mathrm{f} = \frac{\Delta P f_p}{2\rho u^2 L} \quad 4.8$$

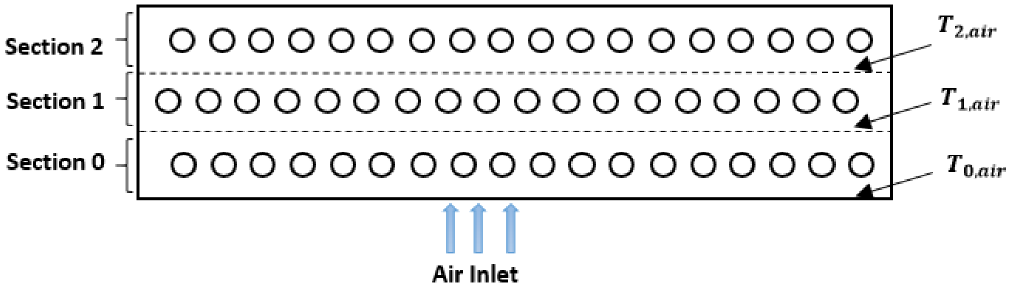

Figure 4. 4 Evaluation planes for average temperatures T0,air, T1,air and T2,air used in CFD simulation.

The meshed gas cooler models are imported to ANSYS Fluent 18.2 to solve mass, momentum and energy governing equations. The boundary conditions used in this model are listed in Table 4.3.

Table 4. 3 Boundary conditions.

| Model | Boundary | Condition |
|---|---|---|
| Phase-I | coil top and bottom surfaces | adiabatic walls |
| | Air inlet | Velocity inlet |
| | Air outlet | Pressure outlet |
| | Tube inner wall | $HTC_r$, free stream temperature (UDF) |
| Phase-II | coil top and bottom surfaces | adiabatic walls |
| | Fins and tubes surface | $HTC_a$, free stream temperature (UDF) |
| | Tube inner wall | $HTC_r$, free stream temperature (UDF) |

### 4.2.4 1D-3D model: Phase II

In phase II model, the entire gas cooler is divided into 10 segments along the pipe length direction in which the length of each segment is ΔZ, as shown in Figure 4.1(b). In each segment, it contains approximately 35 consecutive small coil elements. It is assumed that when refrigerant fluid flow through the length of ΔZ in each pipe, its temperature does not change. Following the assumptions of (d) and (e), the entire gas cooler model is developed based on 10 consecutive fins to simplify the model development and simulation processes. This geometry is also built in SolidWorks 2017 and the model is meshed in ANSYS ICEM CFD 18.2. Meshing of phase II model is shown in Figure 4.5. There is no fluid domain in phase II model, which reducing the computation time greatly. The mesh details are shown in Table 4.2. There is no fluid domain in phase II model which saving computation time greatly. The airside heat transfer coefficient profile developed and calculated from phase I analysis is used in phase II model as the boundary condition of coil fin and tube surfaces. The boundary conditions are indicated in Table 4.3. For the tube-side, C language program was compiled into calculate $CO_2$ heat transfer coefficient based on empirical correlations and therefore to calculate $CO_2$ temperature.

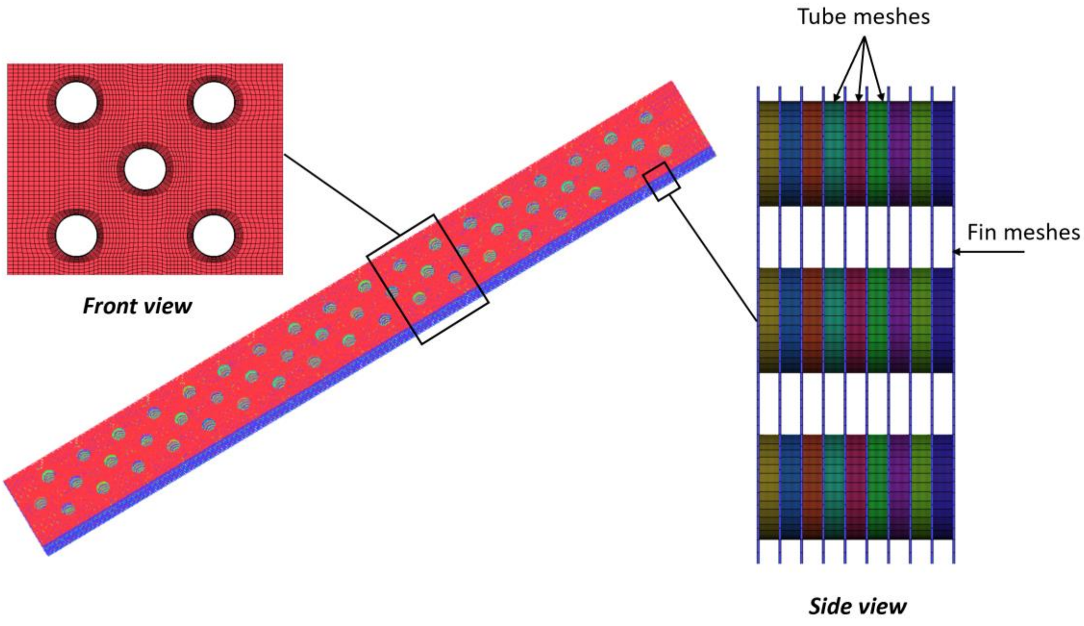

Figure 4. 5 Meshing of phase II model.

Therefore, on the refrigerant side, Gnielinski correlation is used to calculate the respective heat transfer coefficient [67]:

$$Nu = \frac{\xi/8(Re-1000)Pr}{12.7\sqrt{\frac{\xi}{8}}\left(Pr^{\frac{2}{3}}-1\right)+1.07} \qquad 4.9$$

where Filonenko’s correlation is used to predict the friction coefficient [67]:

$$\xi = (0.79\, ln(Re) - 1.64)^{-2} \tag{4.10}$$

While Reynolds number ($Re$), Nusselt number (Nu) and Prandtl number ($Pr$) are calculated:

$$Re = \frac{\rho u d}{\mu} \tag{4.11}$$

$$Pr = \frac{\mu c_p}{k} \tag{4.12}$$

$$Nu = \frac{HTC_r k}{d} \tag{4.13}$$

Refrigerant side heat transfer coefficient can be determined by following equation:

$$HTC_r = \frac{Nu}{d} k \tag{4.14}$$

There is a heat balance between surface and refrigerant, where refrigerant temperature of each segment will be calculated:

$$Q_r = \dot{m} c_p \left(T_{r,i} - T_{r,i+1}\right) = HTC_{r,i} A_i (T_{r,i} - T_w) \tag{4.15}$$

### 4.2.5 Grid independency test

A grid independence test was conducted to confirm the precision of the CFD modelling outcomes. The number of mesh elements for each fin in the phase II model is identical to that of the phase I model due to the simulation methods described previously. To reach the optimal grid number, three hexahedral type mesh structures of phase I model with varied mesh element sizes of 769,120, 993,168 and 1370572 were executed. The output temperature of the refrigerant was utilized to analyze the effect of grid size. Figure 4.6 illustrates the range of expected refrigerant outflow temperatures for varying grid node counts. The difference in relative temperature between the model's last two mesh sizes is less than 1%. Therefore, the number of 1370572 mesh elements was selected for all simulations.

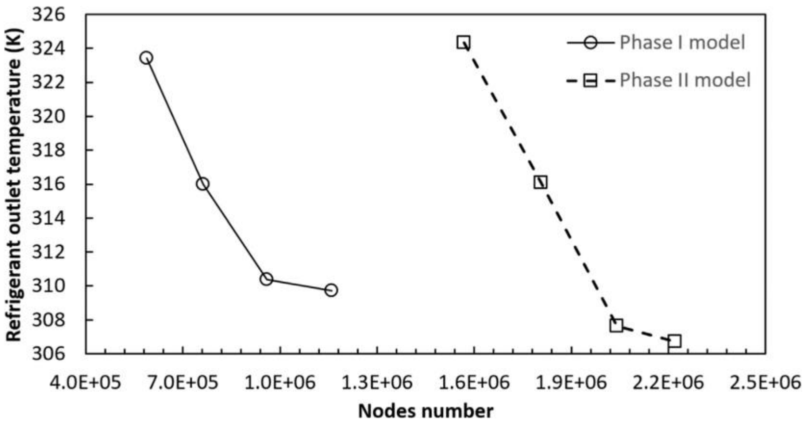

Figure 4.6 Variations of refrigerant outlet temperatures with different element numbers.

## 4.3 Model Results and Validations

Ge and Copper [7] used the correlations of Wang et al. [72] to compute the airside fanning f-friction and colburn j-factor in their numerical study. In addition, the experimental results conducted by Hwang [112] were used to validate the temperature profile of the refrigerant along the flow direction of the pipe. To investigate the heat transfer performance of a $CO_2$ finned-tube gas cooler, Hwang created a purpose-made test rig and operated it under varied operating settings in $CO_2$ transcritical cycles. The test apparatus consisted of an airflow duct, two environmental chambers, a finned-tube gas cooler (as depicted in Figure 4.1), an expansion valve, an evaporator, and a compressor. To analyze and compare the performance of the finned-tube gas cooler, a number of significant operating parameters were adjusted and monitored. These included air inlet velocity, air inlet temperature, refrigerant inlet pressure, temperature and mass flow rate.

Controlling the airflow velocity by adjusting the airflow fan speed. An inverter was utilized to alter the mass flow rate of the refrigerant by controlling the speed of the reciprocating compressor. 52 thermocouples were utilized to measure refrigerant temperatures at each pipe bend along the path of refrigerant flow.

There are totally 36 test and CFD simulation conditions as shown in Table 4.4. Air inlet temperature varied from 302.55 K to 308.15 K, air inlet velocity changed from 1 m/s to 3 m/s, $CO_2$ inlet pressure varied from 9 MPa to 11 MPa, $CO_2$ mass flow rated changed from 0.038 kg/s to 0.076 kg/s.

The validation of the CFD model is based on the results of air-side heat transfer coefficients and refrigerant temperature profiles at different operating conditions in this study. Correlations of Wang et al. [72] are utilized to validate the CFD predictions of airside fanning friction factor and Colburn j-factor. In Wang et al.'s research, 88.6% of j factors are within 15% errors and 85.1% of the friction factors are within 15% errors. Besides, the database of Hwang's experiment has also validated the CFD results of $CO_2$ temperature profile and $CO_2$ gas cooler outlet temperatures in which the discrepancies between test and simulation are all within +5K, as shown in Figure 4.7.

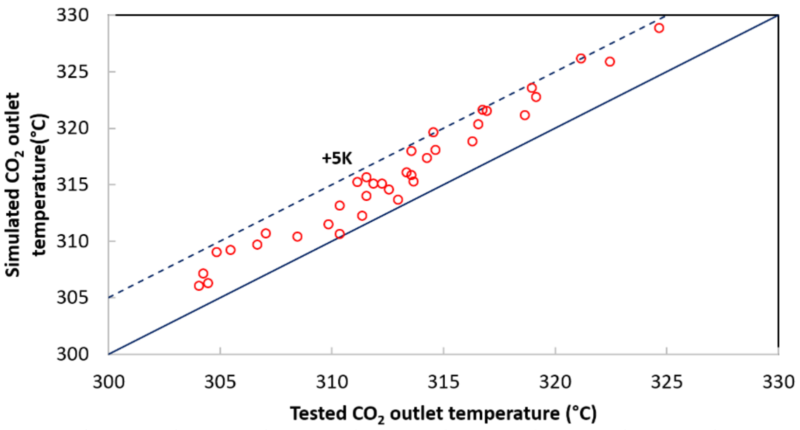

Figure 4.7 Comparisons of simulation and test results for $CO_2$ outlet temperatures of the gas cooler.

**Table 4. 4 36 Operating conditions and results.**

| Air inlet temperature(k) | Air inlet velocity(m/s) | Refrigerant inlet temperature(k) | Refrigerant flow pressure (MPa) | Refrigerant flow rate(kg/s) | Tested refrigerant outlet temperature(k) | CFD simulated refrigerant outlet temperature(k) |
|---:|---:|---:|---:|---:|---:|---:|
| 302.55 | 1 | 391.25 | 9 | 0.038 | 313.55 | 315.87 |
| 302.55 | 2 | 382.65 | 9 | 0.038 | 306.65 | 309.71 |
| 302.55 | 3 | 386.65 | 9 | 0.038 | 304.45 | 306.32 |
| 302.55 | 1 | 397.15 | 10 | 0.038 | 314.65 | 318.08 |
| 302.55 | 2 | 391.15 | 10 | 0.038 | 305.45 | 309.24 |
| 302.55 | 3 | 390.25 | 10 | 0.038 | 304.25 | 307.16 |
| 302.55 | 1 | 401.95 | 11 | 0.038 | 313.55 | 318.00 |
| 302.55 | 2 | 396.65 | 11 | 0.038 | 304.85 | 309.06 |
| 302.55 | 3 | 396.25 | 11 | 0.038 | 304.05 | 306.05 |
| 302.55 | 1 | 367.95 | 9 | 0.076 | 314.55 | 319.64 |
| 302.55 | 2 | 363.95 | 9 | 0.076 | 311.55 | 314.01 |
| 302.55 | 3 | 360.05 | 9 | 0.076 | 310.35 | 310.64 |
| 302.55 | 1 | 376.45 | 10 | 0.076 | 318.95 | 323.59 |
| 302.55 | 2 | 367.95 | 10 | 0.076 | 312.25 | 315.10 |
| 302.55 | 3 | 363.85 | 10 | 0.076 | 308.45 | 310.41 |
| 302.55 | 1 | 383.75 | 11 | 0.076 | 322.45 | 325.90 |
| 302.55 | 2 | 373.85 | 11 | 0.076 | 311.55 | 315.68 |
| 302.55 | 3 | 370.55 | 11 | 0.076 | 307.05 | 310.71 |
| 308.15 | 1 | 394.45 | 9 | 0.038 | 316.28 | 318.83 |
| 308.15 | 2 | 392.55 | 9 | 0.038 | 312.95 | 313.68 |
| 308.15 | 3 | 391.95 | 9 | 0.038 | 311.35 | 312.24 |
| 308.15 | 1 | 400.85 | 10 | 0.038 | 318.65 | 321.14 |
| 308.15 | 2 | 395.75 | 10 | 0.038 | 311.85 | 315.09 |
| 308.15 | 3 | 395.35 | 10 | 0.038 | 310.35 | 313.15 |
| 308.15 | 1 | 406.45 | 11 | 0.038 | 319.15 | 322.77 |
| 308.15 | 2 | 402.05 | 11 | 0.038 | 311.15 | 315.23 |
| 308.15 | 3 | 401.55 | 11 | 0.038 | 309.85 | 311.50 |
| 308.15 | 1 | 365.65 | 9 | 0.076 | 316.95 | 321.56 |
| 308.15 | 2 | 363.15 | 9 | 0.076 | 313.35 | 316.08 |
| 308.15 | 3 | 361.55 | 9 | 0.076 | 312.55 | 314.60 |
| 308.15 | 1 | 377.25 | 10 | 0.076 | 321.15 | 326.19 |
| 308.15 | 2 | 371.55 | 10 | 0.076 | 316.55 | 320.37 |
| 308.15 | 3 | 367.05 | 10 | 0.076 | 314.25 | 317.37 |
| 308.15 | 1 | 382.75 | 11 | 0.076 | 324.65 | 328.89 |
| 308.15 | 2 | 375.05 | 11 | 0.076 | 316.75 | 321.61 |
| 308.15 | 3 | 371.55 | 11 | 0.076 | 313.65 | 315.31 |

### 4.3.1 Airside heat transfer coefficient and pressure drop

For determining turbulent or laminar model during the CFD simulation, the air inlet Reynolds numbers based on the fin pitch were calculated in the range of 94.1-282.3 such that laminar flow and viscous models were selected. Different values of Colburn j-factor at various Reynolds numbers and different operating conditions have been calculated and compared with those calculated by Wang et al.'s [72] correlations to evaluate and validate the calculations of airside heat transfer coefficients , as shown in Figure 4.8(a) and 8(b). As a result, the airside heat transfer coefficient rises from 47.71W/m2K to 73.37 W/m2K while the Reynolds number increases from 94.1 to 282.3. The largest difference between the CFD predicted j-factor and Wang et al.'s correlation is 4%, indicating that the CFD simulations results and the literature correlations are in good agreement.

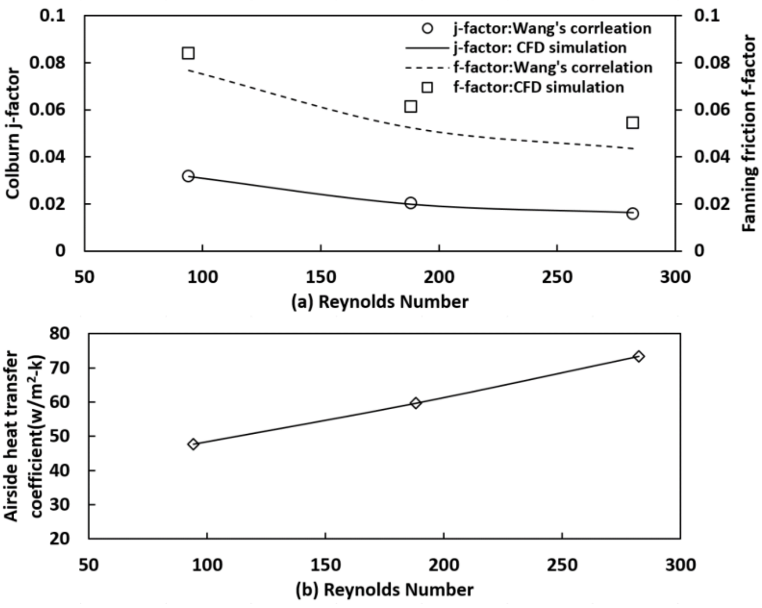

Figure 4.8 Comparison of performance parameters of varying Reynolds number: (a) Colburn j-factor and Fanning friction f-factor, (b) airside average heat transfer coefficient.

The only variable in airside pressure drop is the Reynolds number. Increased airflow inlet velocity increases pressure drop. When air moves through a crossflow finned-tube gas cooler, a pressure drop is produced, which can be influenced by a number of variables, including fin diameters, tube rows, fin structures, and air velocity. If the pressure drop is excessively high, the airflow fan will require more electricity. The comparison of Fanning friction f-factor between CFD simulation and Wang's correlation [72] at different Reynolds number is shown in Figure 4.8(a), indicating maximum deviation value of 13%. Since plain fins are considered in this CFD model, the simulation demonstrates a substantially higher pressure drop difference at various Reynolds numbers compared to measurements [113], as shown in Figure 4.9. The CFD simulation findings demonstrate that fin structure has a significant effect on pressure drop. To compensate that, the following equation is derived in order to predict the relation between air flow pressure drop with lance and plain fins (CFD) for this specific finned-tube gas cooler:

$$\Delta \mathrm{P} = \alpha * \Delta P_{CFD}^{2} + \beta * \Delta P_{CFD} + \gamma \qquad 4.16$$

Where, $\alpha = -0.003109, \beta = 2.272, \gamma = -0.1912$

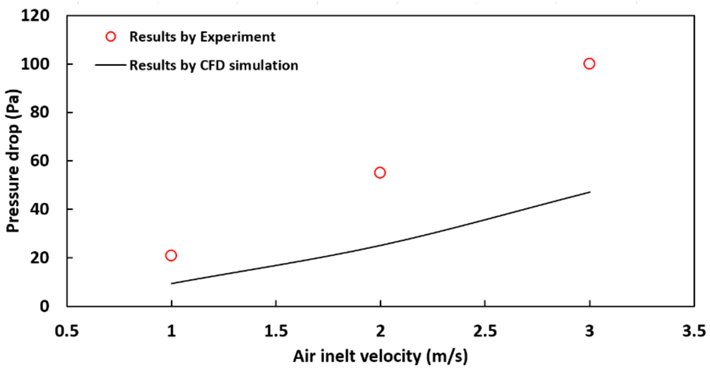

Figure 4.9 Comparison of pressure drop between experimental results and CFD simulation results.

Pressure drop is caused by friction when fluid flows through passages between fins. The lanced fins have substantially more friction than the plate fins, resulting in a significantly greater pressure decrease. Air pressure drop is a function of air flow rate, such that as air input velocity increases, so does air pressure drop. The airside pressure decreases from 20 Pa to 100 Pa as the air inlet velocity increases from 1m/s to 3m/s. However, with a gas cooler with plate fins, the airside pressure drop increases from 9 Pa to 47 Pa the same air inlet velocity changes.

### 4.3.2 $CO_2$ side heat transfer coefficient

The calculation of $CO_2$ heat transfer coefficient in tubes are based on the empirical correlation of Eq. 4.9. Figure 4.10 shows the variations of $CO_2$ heat transfer coefficient at different temperature, different pressure and different $CO_2$ mass flow rate for this study. From Figure 4.10 (a) it is known that the maximum $CO_2$ heat transfer coefficient is prominently influenced by its heat specific heat. With higher $CO_2$ mass flow rate, the higher heat transfer coefficient as shown in Figure 4.10 (b).

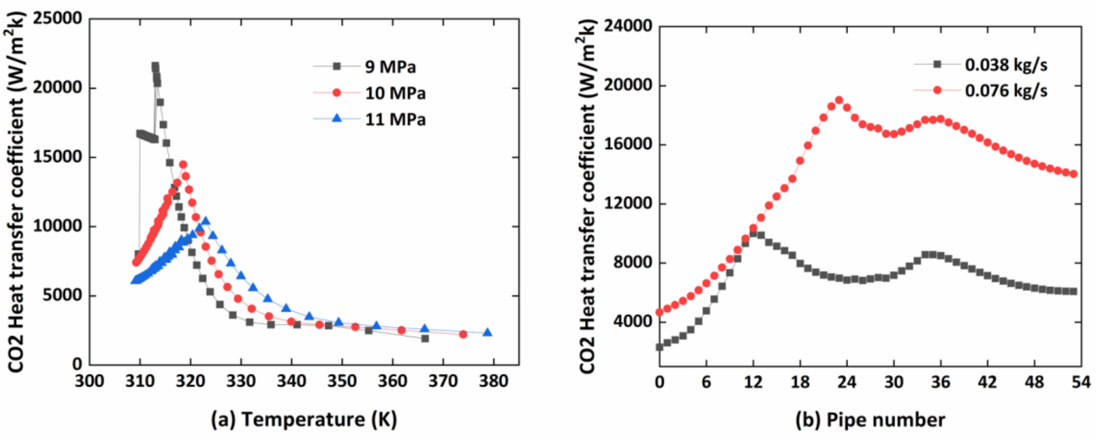

(a) Temperature (K)

(b) Pipe number

Figure 4. 10 Variations of $CO_2$ heat transfer coefficients.

### 4.3.3 Temperature and velocity distribution

Figure 4.11 (a) (b) (c)show the temperature contours and streamlines of along middle plane in airflow region of phase I model. With the increase of air velocity, the airflow temperature can be decreased due to higher heat exchange between airflow and $CO_2$ through fins and tubes. The temperature of airflow around the first tube row is lowest. The average temperature of airflow at 1 m/s, 2 m/s and 3 m/s are 317 K, 311 K and 309 K respectively.

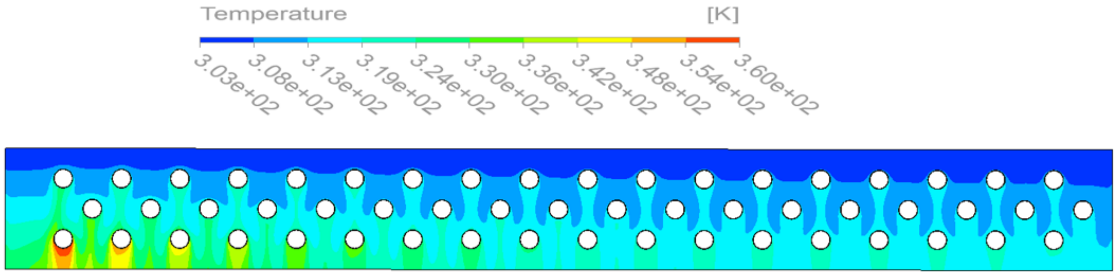

**(a)** $v_{airflow,inlet}$ **= 1 m/s**

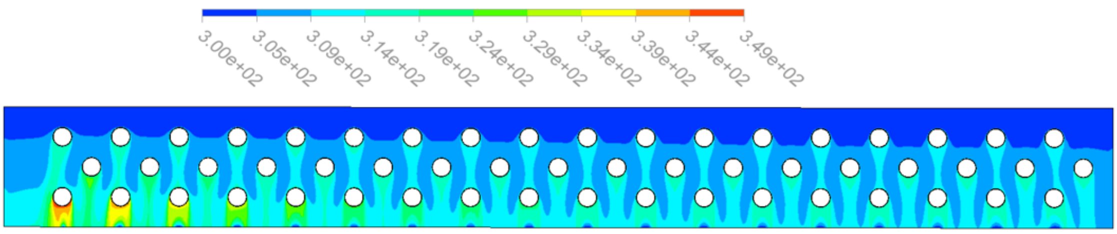

**(b)** $v_{airflow,inlet}$ **= 2 m/s**

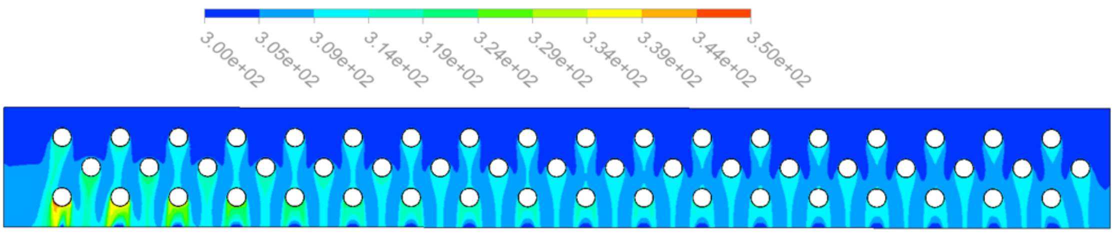

**(c)** $v_{airflow,inlet}$ **= 3 m/s**

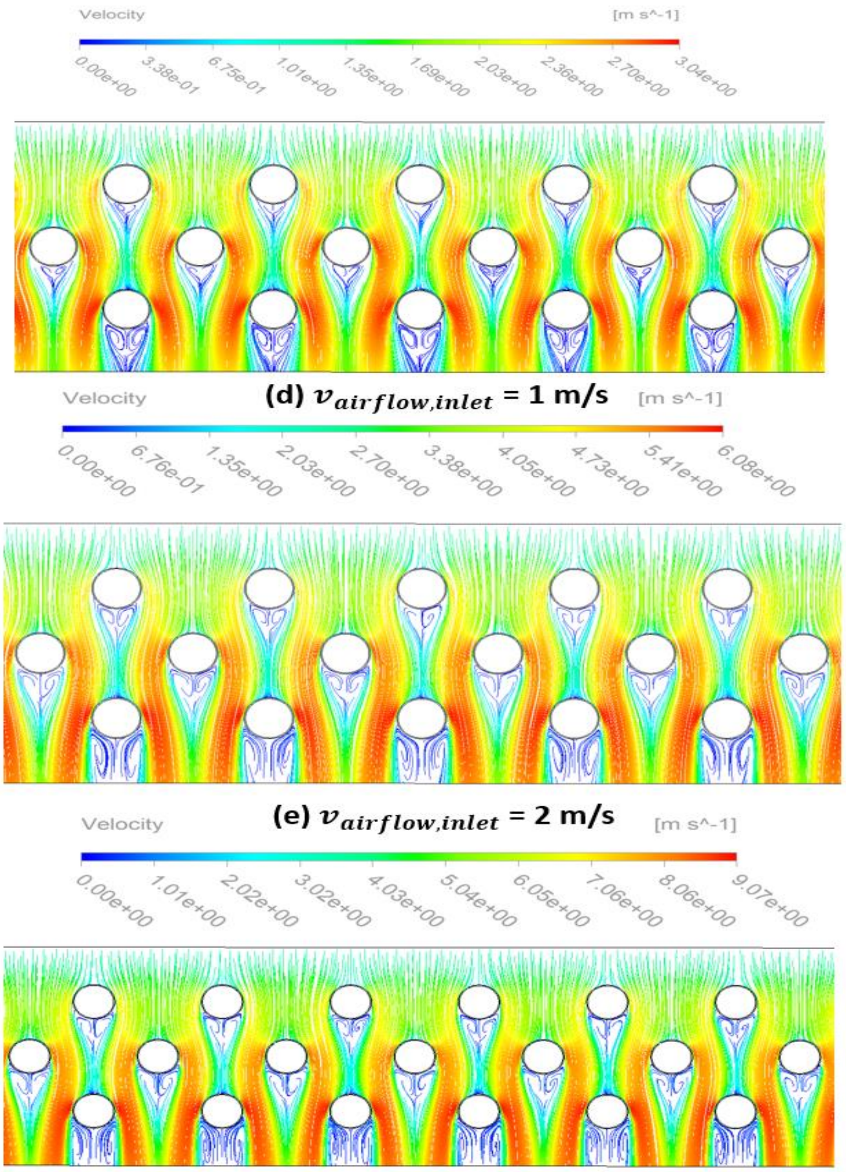

**(d)** $v_{airflow,inlet}$ **= 1 m/s**

**(e)** $v_{airflow,inlet}$ **= 2 m/s**

**(f)** $v_{airflow,inlet}$ **= 3 m/s**

**Figure 4.11 Temperature contours and streamlines of airflow at different air inlet velocity (operating condition: T $_{air,in}$ = 302.55K, m $_{CO2}$ = 0.038kg/s, P$_{CO2,in}$ = 9MPa).**

When the air flows externally through a tubular area, it separates into two side streams and then forms a pair of symmetric vortexes as shown in Figure 4.11 (d) (e) (f). The vortexes are also named as stagnant regions, heat transfer performance is not sufficient in these regions. vortexes are more obvious when airflow velocity is relative lower.

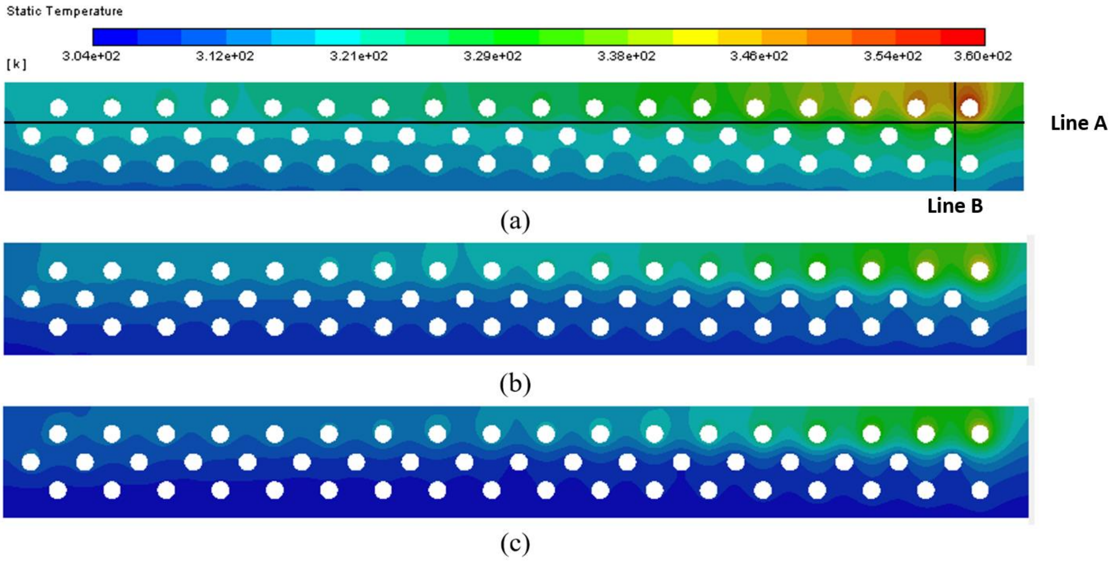

**Figure 4.12** The temperature of fin surface with the variation of air inlet velocity: (a) Va = 1m/s; (b) Va = 2m/s; (c) Va = 3m/s (operating condition: $T_{air,in}$ = 302.55K, $m_{CO2}$ = 0.038kg/s, $P_{CO2,in}$ = 9MPa).

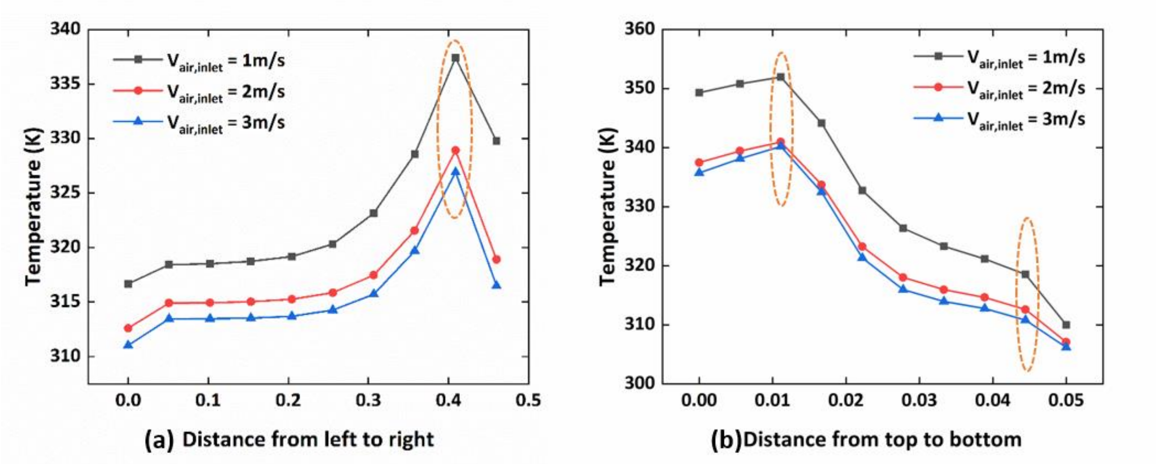

**Figure 4. 13** Temperature profile of Line A and line B at different air inlet velocity (operating condition: $T_{air,in}$ = 302.55K, $m_{CO2}$ = 0.038kg/s, $P_{CO2,in}$ = 9MPa).

This 1D-3D coupled simulation method allows researchers to observe directly the temperature distribution on the fin surface. The temperature at each point on the fin surface can be obtained. As shown in Figure 4.12, the average temperature of fin surface reaches to the lowest when air inlet velocity increases up to 3m/s. The fin surface temperature around the first tube row where the refrigerant inlet is located is the highest since it is close to the refrigerant inlet. Similarly, the surface temperature of the fins around the third tube row, where the refrigerant outflow is located, is the lowest. Reduced air velocity increases air outlet temperature. Due to the formation of symmetric vortices behind tubes, air is trapped in this region and heated by fins and tube surfaces. Air surrounding refrigerant inlet pipes has a greater average temperature than other locations. This is one of the reasons why reverse heat transfer occurs during the refrigeration cooling process.

Besides, for the 1D model, generally the heat conduction along longitudinal direction of fin is neglected. However, from the results of present study, longitudinal heat conduction has a great influence on fin temperature, and therefore both the air and refrigerant temperatures will be affected. Figure 4.13 shows the temperature profile of line A and line B in Figure 4.11. It can be observed from Figure 4.13 (a) that temperature of line A increased from left to right, and it dramatically increase when it is near the pipe inlet, as circled in figure. As seen from Figure 4.13 (b), it also proved that hotter tube can significantly influence the neighbor fin surface. Therefore, heat is transferred from hotter tube to colder tube across fins. That is the main reason causes reverse heat transfer, the refrigerant temperature thus might not decrease continuously along $CO_2$ refrigerant flow direction. As an important finding in this study, it is difficult to be detected by other simulation methods. In conclusion, heat transfer from hotter tubes to fins and colder tubes via thermal conduction has a substantial impact on the refrigerant and fin surface temperature distributions.

### 4.3.4 Analysis of gas cooler performance

As shown in Figure 4.14, refrigerant temperature profiles along refrigerant flow direction at various operating conditions are predicted. Refrigerant temperature drops dramatically in the first-row tubes numbered from ‘0’ to ‘17’, as indicated in Figure. 4.1.

It can be observed that approximately 90% of overall temperature drop takes place in the first-row tubes. When air flows through the gas cooler, its temperature increases greatly after the row tubes numbered from ‘36’ to ‘53’ than that after the middle row tubes. Although airflow temperature is increased at airflow exit, the temperature difference between airflow around the first-row tubes and tube wall surface is still large, causing large amount of heat transfer rate. In addition, particular thermos-physical properties of $CO_2$ can contribute to this phenomenon. There is a slight temperature step-down trend when $CO_2$ flow turns from pipe ‘18’ to ‘19’, since the air temperature around the middle row is lower than that of around first tube row, leading higher heat transfer rate and thus more temperature drop. In the middle row, refrigerant temperature decreases slightly from pipe ‘18’ to ‘26’. However, there is an upward trend when refrigerant flows from pipe ‘32’ to ‘36’. This phenomenon is prominent when air inlet velocity is at a lower value of 1 m/s. The main reason is that heat is conducted across fins from hotter tubes in the first tube row to the adjacent tubes in the middle and third tube rows. The thermal conductivity of a specified fin material is determined by temperature, material properties and path length. Higher temperature causes higher heat transfer rate through fins. Besides, when air flows after the upstream tube, it could be constrained for a long time due to the formation of vortexes. This confined air can be heated by adjacent hotter tubes, and then the heat will be transferred reversely from air to tube. Subsequently, to enhance the heat exchanger performance and the efficiency of its associated system, it is suggested to apply split fins between the first and middle tube rows so as to prevent the thermal conductions.

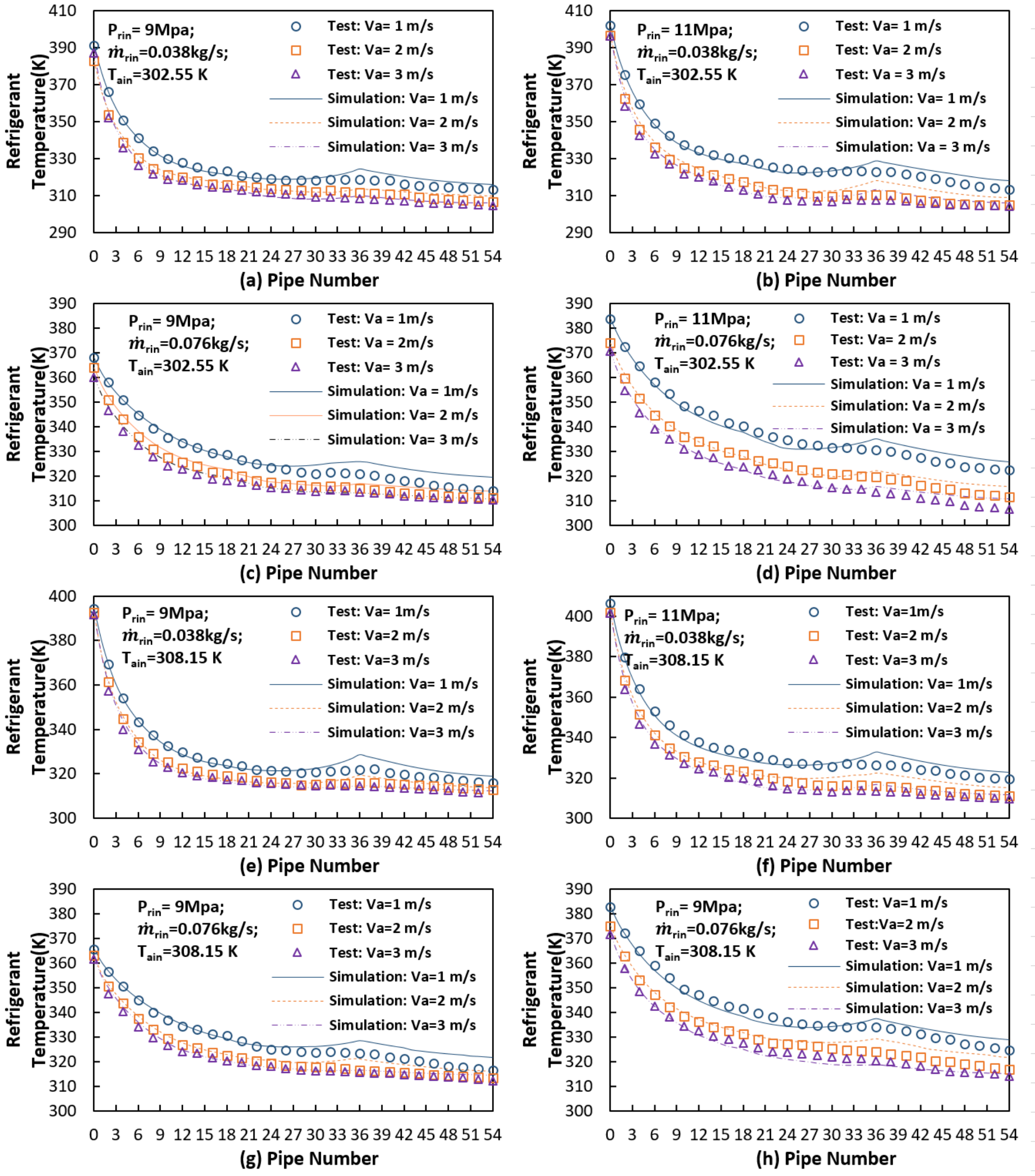

**Figure 4.14 Comparison of simulation results with test results [112] of different test conditions for refrigerant temperature profile along pipe flow direction.**

Under the condition of varied air inlet velocity only, the higher velocity leads to lower the refrigerant exit temperature. This is because, higher velocity can improve the heat transfer coefficient and thus heat transfer rate. At a specified refrigerant pressure, mass flow rate and similar refrigerant inlet temperature, the refrigerant temperature at any position at air inlet temperature of 302.55K is always lower than that at air inlet temperature of 308.15K. This is because higher temperature difference between surface and air leads to larger heat transfer rate and therefore lower refrigerant temperature.

Compared Figure 4.14(e) and Figure 4.14(f), when the refrigerant pressure was 11MPa, although the refrigerant inlet temperature is approximately 10K higher than the condition of 9MPa, their refrigerant exit temperatures are close. It can be summarized from Figure 4.14 that refrigerant temperature decreases with higher refrigerant pressure when other parameters are kept same. Consequently, increasing high side pressure will increase heating capacity. The COP trend of $CO_2$ transcritical cycle is different with traditional cycles, as there does not exist optimum COP in tradition cycles. As for a $CO_2$ transcritical cycle, when the optimum pressure is achieved, the maximum peak value of COP can be reached [114]. Higher refrigerant mas flow rate leads to lower refrigerant inlet temperature. Besides, it is seen from both modelling and experimental results that with increased refrigerant mass flow rate, the temperature of refrigerant decreased due to the conservation of energy. The lowest temperature discrepancies between the test and CFD results for refrigerant temperature profile along flow direction take place when air inlet velocity is 3 m/s. In addition, from Table 4.4 the approach temperature for overall 36 cases can be calculated. The lowest approach temperature can be reached to 3.35 K at higher airflow velocity with lower inlet temperature. It is proved that finned-tube $CO_2$ gas cooler is an alternative heat exchanger which can be used for the proposed biomass-$CO_2$ Transcritical Brayton Cycle.

Lower refrigerant exit temperature makes contribute to higher heating capacity of finned-tube gas cooler and better COP of refrigeration system. Figure 4.15 depicts that the heating capacity increases with increasing air frontal velocity and refrigerant pressure. In comparison of Figure 4.15(a) and 4.15(c), when air inlet temperature is at 302.55K, the heating capacity is always higher than that of air inlet temperature at 308.15K. In addition, heating capacity increases with the increase of refrigerant mass flow rate. For a certain refrigerant pressure at 9MPa, when the refrigerant mass flow rate increases from 0.038 kg/s to 0.076 kg/s, the heating capacities can be improved by 30.14%, 33.08% and 46.36% with air frontal velocity varies from 1,2 and 3 m/s respectively as shown in Figure 4.15(a) and 4.15(b). Similarly, the heating capacities can be improved by 27.88%, 29.2% and 29.98% as indicated in Figure 4.15(c) and 4.15(d). The highest heating capacity occurred at the condition that air inlet temperature is at 302.55K, $CO_2$ mass flow rate is at 0.076 kg/s and gas cooler pressure is at 11MPa. The varied operating conditions of the gas cooler can indirectly affect the performance efficiency of its associated system, as shown in Figure 4.16, assuming that the system evaporator exit temperature and pressure are 268.15K and 3.0459MPa respectively. Compressor inlet and outlet conditions are identical to those of the evaporator outlet and gas cooler inlet, respectively. In addition, the refrigerant enthalpy at the evaporator inlet and gas cooler exit are same. Therefore, the system cooling COP can be computed as follows:

$$COP = \frac{h_{revout} - h_{revin}}{h_{rcpout} - h_{rcpin}} \tag{4.17}$$

As depicted in Figure 4.16, similar effect can be found between the coil heating capacity and system cooling COP at different operating conditions of the gas cooler. The lower air inlet temperature and higher refrigerant mass flow rate can both benefit to the system efficiency. Meanwhile, it also verifies that the gas cooler pressure of 11MPa is close to the optimal pressure for the system operation.

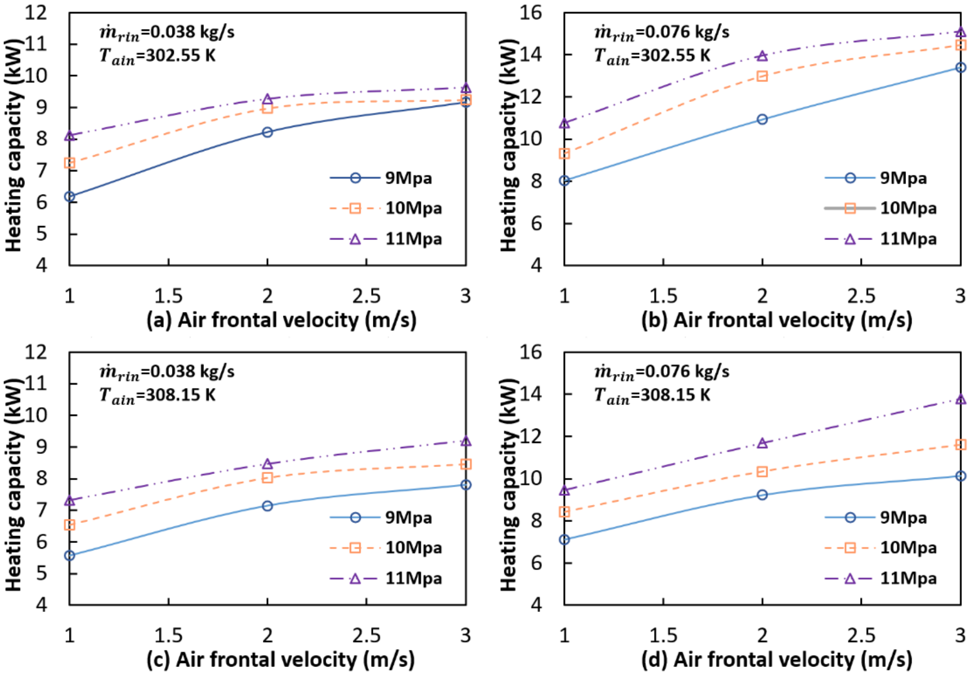

Figure 4.15 Heating capacity of different simulation conditions.

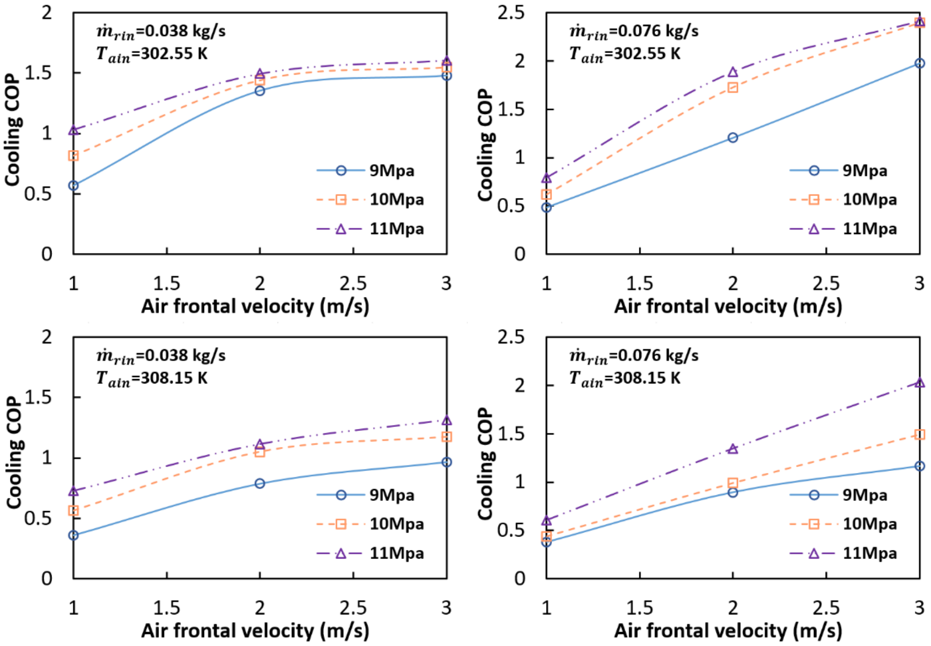

Figure 4.16 Cooling COP at different simulation conditions.

## 4.4 Model applications – effects of various inlet air flow patterns

Most of the research on finned-tube heat exchanger CFD modelling were based on uniform airflow velocity. There is a lack of research investigation and data for the analyses of airflow maldistribution effect on the $CO_2$ gas cooler performance. The validated model is thus used to investigate the effect of airflow velocity maldistribution on the performance of $CO_2$ finned-tube heat exchanger. As shown in Figure 4.17, four inlet air velocity profiles are studied in the CFD simulation: (a) uniform velocity profile ; (b) linear-up velocity profile; (c) linear-down velocity profile; (d) parabolic velocity profile. The four velocity profiles have the same average face velocity. The uniform airflow pattern is used as the baseline model. Each airflow pattern is studied for different Reynolds number ranges from 94.1 to 282.3. Airflow inlet functions for Figure 4.17 are displayed in Appendix C.

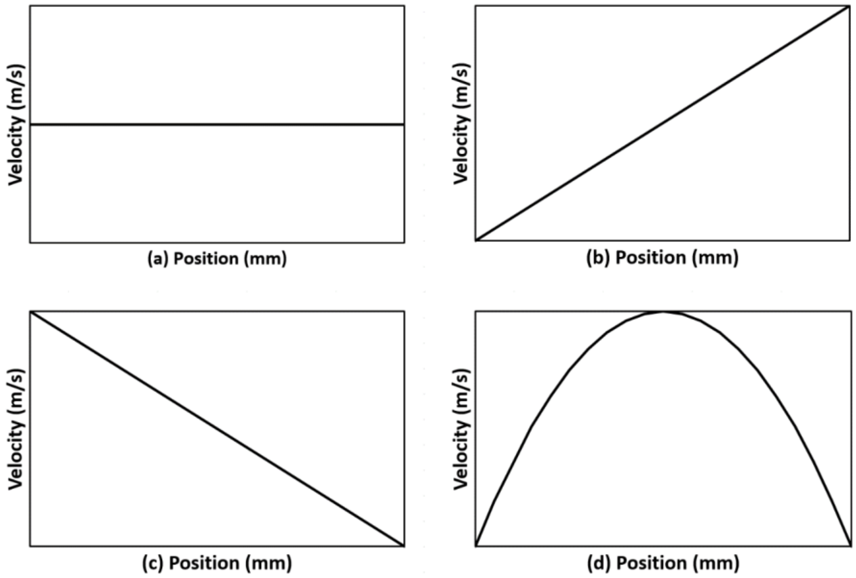

**Figure 4.17** Four different inlet air flow patterns: (a) uniform profile, (b) linear-up velocity profile, (c) linear-down velocity profile, (d) parabolic velocity profile.

### 4.4.1 Airflow temperature contours and velocity contours

Figure 4.18 shows the Comparison of streamlines of airflow at different air inlet conditions of uniform, linear-up, linear-down and parabolic. Although maldistribution airflow pattern has the higher local velocity than uniform airflow as shown in Figure 4.18, the heat exchange between air and $CO_2$ is not sufficient due to air in not distributed evenly. Figure 4.19 displays the temperature contours of a middle fin surface of the gas cooler under different air velocity profile conditions. It is seen that the fin surface of tube row nearing to the airflow entrance (bottom) has the lowest temperature. It should be noted that the thermal conduction between neighbor tube rows through fins can cause significant impact on the fin surface temperature. Since the refrigerant at the coil inlet has the highest temperature, the heat then spreads along the fins through thermal conductivity and affects the temperatures of other neighbor tubes, especially for linear-down airflow inlet profile, as shown in Figure 4.19(c). This is because that the low air flow rate through the coil can reduce the heat transfer and thus increase the fin surface temperature.

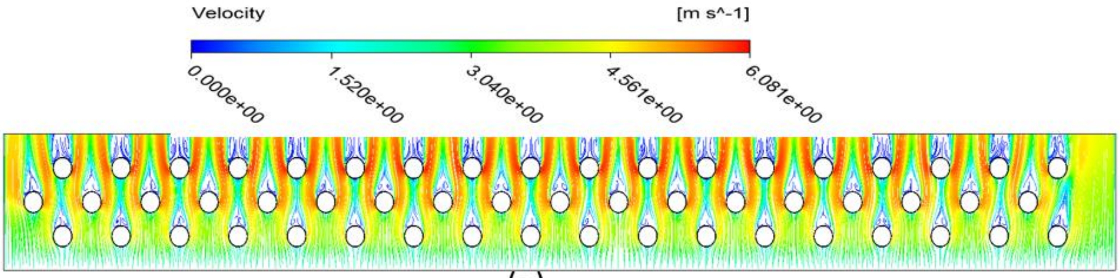

(a)

Uniform

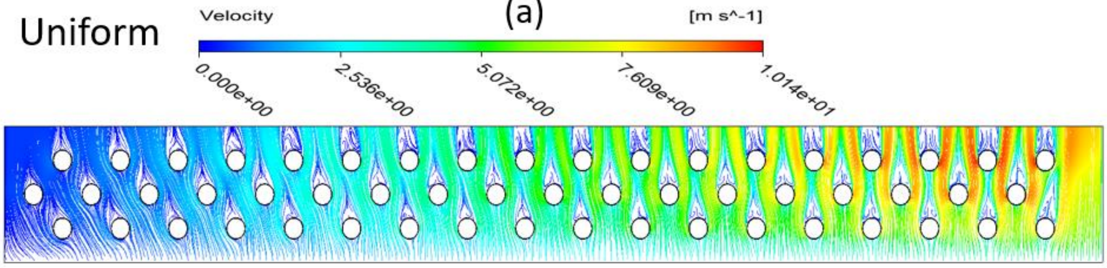

(b)

Linear-up

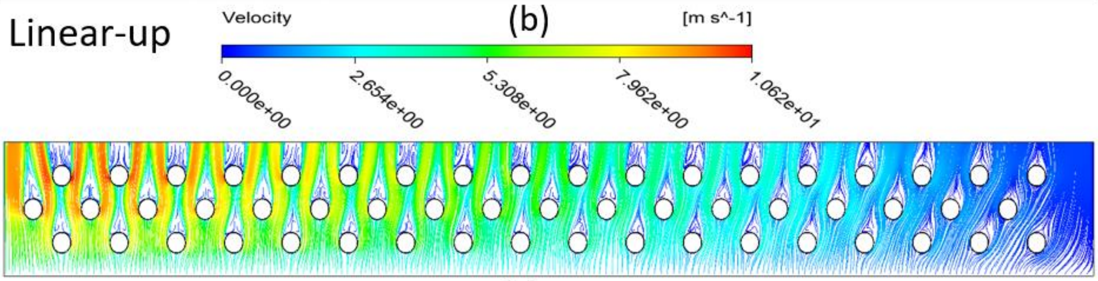

(c)

Linear-down

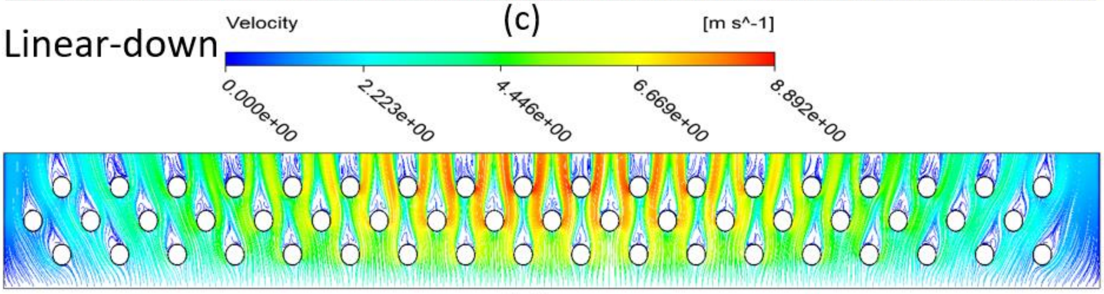

(d)

Parabolic

**Figure 4. 18 Streamlines of air at different airflow patterns. (operating condition: $T_{air,in}$ = 302.55K, $V_{air,inlet}$=2m/s, $m_{CO2}$ = 0.038kg/s, $P_{CO2,in}$ = 9MPa).**

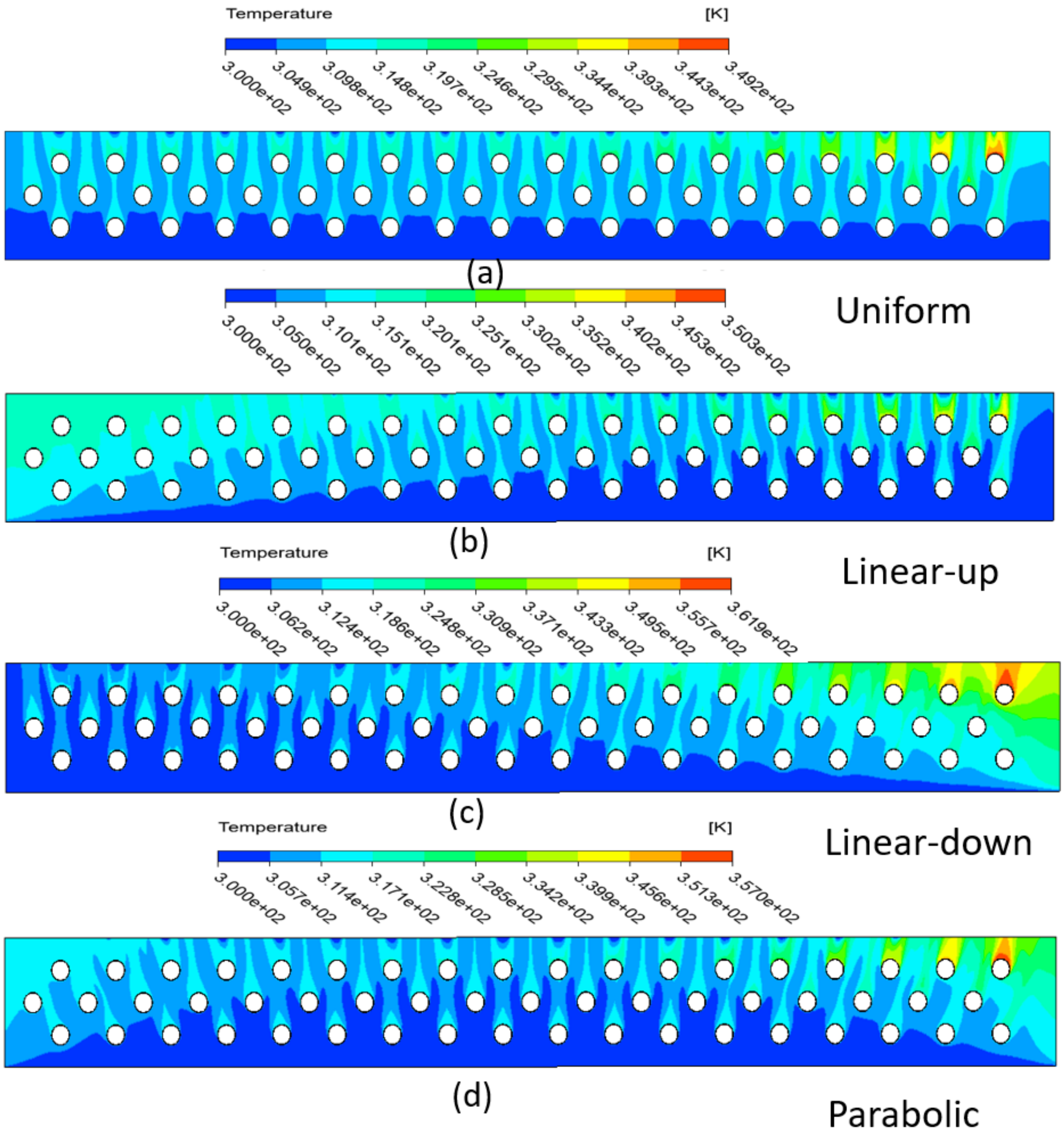

**Figure 4. 19 Temperature distribution of airflow at different airflow patterns. (operating condition: $T_{air,in}$ = 302.55K, $V_{air,inlet}$=2m/s, $m_{CO2}$ = 0.038kg/s, $P_{CO2,in}$ = 9MPa).**

### 4.4.2 Colburn j-factor and Fanning f-friction factor

There is an obvious trend that Colburn j-factor and Fanning f-factor decrease with higher Reynolds number. The j factor of linear-up airflow is always lower than that of uniform velocity profile with Reynolds number increasing. When air average inlet velocity is at 1 m/s, the j factor of linear-up velocity profile is 19.13% lower than that of uniform airflow as indicated in Figure 4.20(a). However, the j factors of linear-down airflow pattern are always higher compared with uniform airflow when air inlet average velocity varies from 1m/s to 3m/s. When air inlet average velocity reaches to 3m/s, the j factor of parabolic case is higher than that of uniform. Colburn j-factor is a dimensionless parameter and a function of heat transfer coefficient, airside heat transfer coefficients of linear-up, linear-down and parabolic cases increase from 38.57 to73.09 W/m$^2$K, 50.15 to 78.07 W/m$^2$K and 43.63 to 76.97 W/m$^2$K respectively with Reynolds number varying from 94.1 to 282.3. In comparison of the linear-down and linear-up velocity profiles, they have the similar heating capacity as shown in Figure 4.22(b), but the linear-up velocity profile generates higher air average temperature. Therefore, the average heat transfer coefficient of linear-up case is lower than that of linear-down case. Figure 4.20(b) indicates the difference of airside pressure drop between uniform and maldistribution airflows. The linear-down case has the highest pressure drop, which is 7.9%, 12.1% and 15.7% more than that of uniform case in terms of f factor when Reynolds numbers change from 94.1 to 282.3. Results are achieved based on plate fins, air non-uniform distribution could have more significant impact on raised lance fin gas cooler pressure

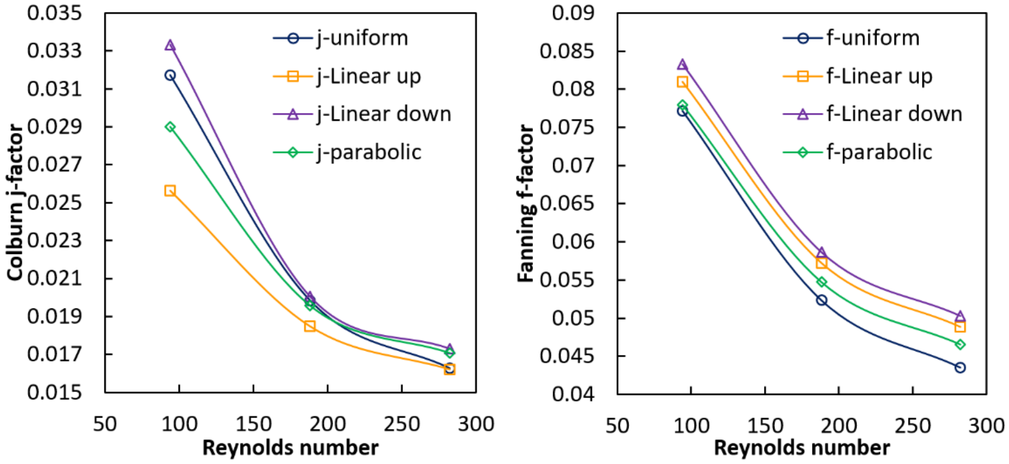

**Figure 4.20 Effects of air maldistribution on heat transfer coefficient and pressure drop: (a) Colburn j-factor, (b) Fanning f-friction. The results are based on refrigerant inlet pressure of 9Mpa, air inlet temperature of 302.55 k and refrigerant mass flow rate of**

drop. It is concluded that maldistribution air velocity profile always cause higher pressure drop. Fan power is the only energy required by airside, the high pressure drop requires high power of fan. The most important method to reduce fan power is to decrease pressure drop.

### 4.4.3 $CO_2$ temperature profile

The inlet airflow pattern can directly influence refrigerant temperature profile as shown in Figure 4.21. Although the airflow is non-uniform, most heat of refrigerant is rejected through the first-row of gas cooler similar to that with uniform airflow pattern. Non-uniform airflow patterns also cause reverse heat transfer, especially when air average velocity is at 1m/s. However, this phenomenon is greatly minimized due to the velocity characteristics of linear-up pattern, which means air velocity near high temperature pipes is larger such that the heat exchange is improved. Approach temperature is defined as the temperature difference between air inlet and refrigerant exit temperature, which has considerable impact on cooling capacity and heat transfer performance of heat exchanger. From Figure 4.22(b), it is known that the parabolic airflow pattern has higher heating capacity compared with linear-up and linear-down, while the performance with airflow linear-up and linear down is quite close. However, uniform case has the lowest approach temperature and thus highest heating capacity in all cases.

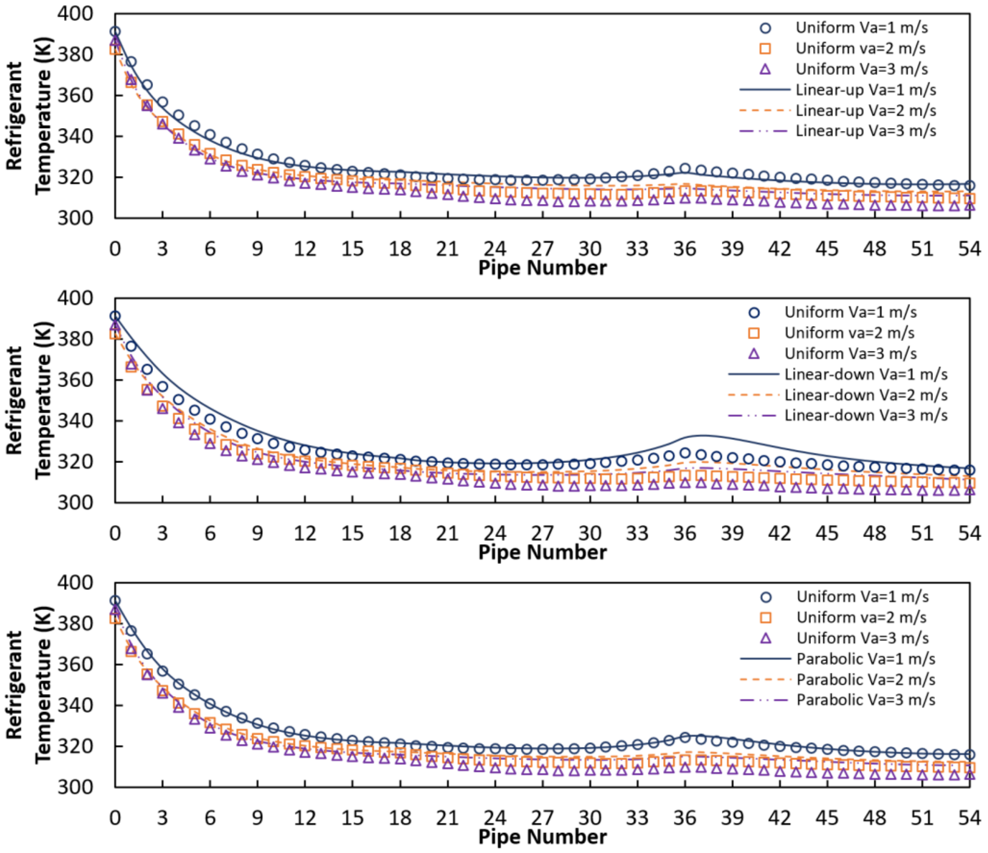

**Figure 4.21 Comparison of uniform airflow pattern and air maldistribution airflow pattern for refrigerant temperature profile along pipe flow direction: (a) linear-up, (b) linear-down, (c) parabolic. The results are based on refrigerant inlet pressure of 9MPa, air inlet temperature of 302.55k and refrigerant mass flow rate of 0.038 kg/s.**

### 4.4.4 Heating capacity and cooling COP

When Reynolds number varies from 94.1 to 282.3, the approach temperature differences between uniform velocity profile and parabolic and linear-down as well as linear-up are 0.479K, 2.948K and 4.471K respectively as shown in Figure 4.22(a). The influence of air maldistribution on heating capacity is not prominent when air average velocity is low, as shown in Figure 4.22 (b). Although the average heat transfer coefficient of linear-down velocity profile is the largest, the gas cooler performance is however the worst. This is because different airflow pattern causes different local heat transfer coefficient, affecting the heat transfer rate dramatically and thus the refrigerant temperature. For improving the performance of gas cooler, uniform airflow and high airside velocity can make the best contribution. When the refrigerant temperature and pressure evaporator exit are assumed as 268.15K and 3.0459MPa, the cooling COP of its associated system can also be calculated at the conditions of gas cooler air maldistribution, as shown in Figure 4.22 (c). Similar results can be obtained between the coil heating capacity and system cooling COP. Therefore, at a constant evaporating temperature, uniform air velocity profile has the highest system cooling COP compared with those with air maldistribution velocity profiles.

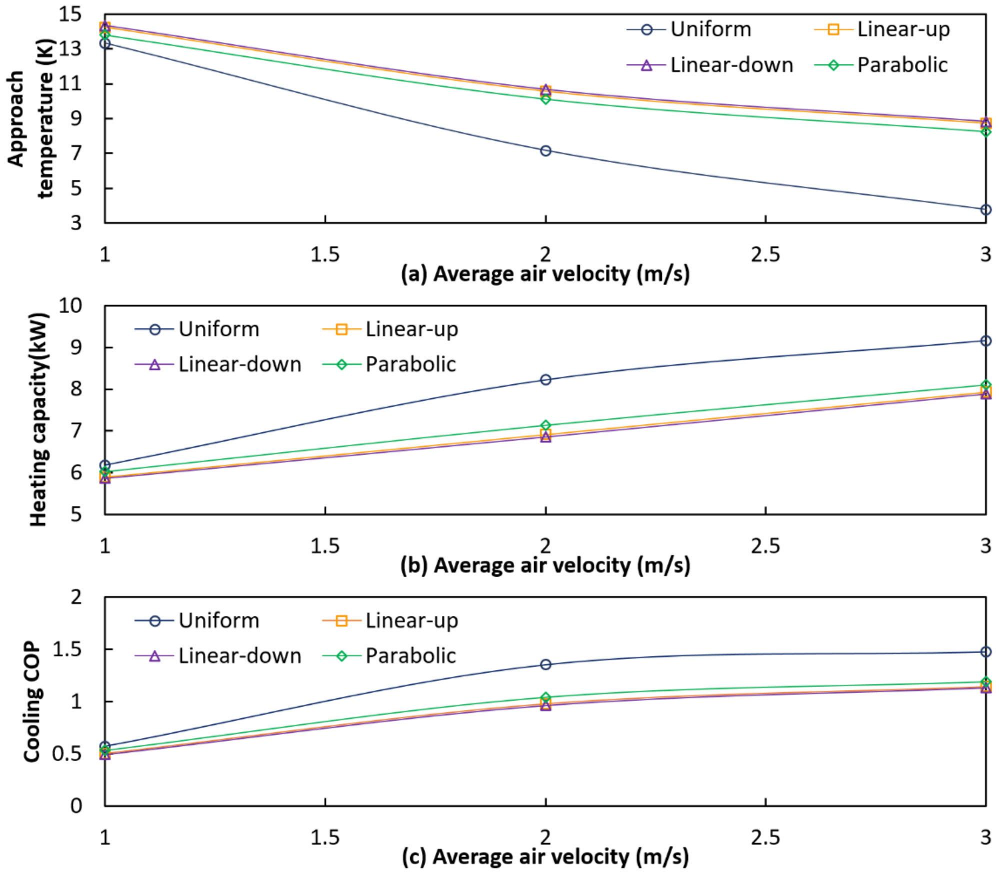

**Figure 4.22** Comparison of uniform airflow pattern and air maldistribution airflow pattern for gas cooler approach temperature and heating capacity: (a) approach temperature, (b) heating capacity, (c) cooling COP.

## 4.5 Summary

A 1D-3D coupled CFD model method for a fin-and-tube $CO_2$ gas cooler has been proposed and explained in this chapter. The proposed method provided additional and valuable results that other methods cannot be achieved. The present study has higher accuracy of results and less computation time. The model simulation results have been validated with experimental measurements and literature correlations at different test conditions. This validated model is used to investigate the effect of airflow velocity maldistribution and different operating conditions on the performance of $CO_2$ finned-tube gas cooler and its associated system efficiency.

This 1D-3D model not only allows to predict airside average heat transfer coefficient, airside pressure drop and the effect of different operating conditions on refrigerant temperature profile along pipe flow direction, but also it can obtain fin surface temperature distribution and air velocity distribution and their effects on the coil performance. Airside heat transfer coefficient increases with higher air inlet velocity, higher air inlet temperature as well as higher refrigerant pressure. Approximately 90% of the refrigerant temperature drop occurs in the first tube row of gas cooler due to the larger temperature difference between air and tube surfaces. Heating capacity of gas cooler and system Cooling COP are improved with the increase of refrigerant pressure (close to optimal pressure), air frontal velocity and refrigerant mass flow rate. Under the condition of only airflow pattern is the variable, uniform air velocity profile can produce the best performance of heating capacity and system cooling COP. Therefore, at a constant evaporating temperature, uniform air velocity profile has the highest COP of system compared with those at air flow maldistribution conditions.  Besides, there was an important finding that longitudinal heat conduction through fins leads to reverse heat transfer phenomenon, which negatively affects the performance of finned-tube gas cooler. According to the performance of the finned-tube gas cooler, it is a feasible gas cooler can be used in the proposed $CO_2$ Supercritical or Transcritical Brayton cycle for cooling $CO_2$. However, it is suggested that split fins can be applied to minimize the longitudinal heat conduction through fins and further improve the performance of this finned-tube type gas cooler.

The following **chapter 5** will carry out CFD simulations to investigate the effect of heat conduction through fins on performance of finned-tube $CO_2$ gas cooler. An effective method of split fins will be proposed. There are very few investigations with CFD modelling on the finned-tube $CO_2$ gas coolers with and without split fins. The optimal design of split fins and their effect on the heat exchanger performance need to be further investigated and clarified.

# Chapter 5 – Investigation of the Effect of Heat Conduction Through Fins on The Performance of Finned-tube $CO_2$ Gas Coolers

## 5.1 Introduction

This chapter will introduce the investigation of the effect of heat conduction through fins on the performance of finned-tube $CO_2$ gas coolers. The results of this simulation have been published as a journal paper in International Journal of Heat and Mass Transfer during my PhD study. Therefore, this chapter is a slightly modified version of Zhang et al. [115] published in International Journal of Heat and Mass Transfer. The longitudinal heat conduction along fins may result in reversible heat transfer between adjacent tubes, hence reducing the heat exchanger's capacity. To cope with this adverse effect, the heat exchanger design with split fins between tube rows can be applied although further verification and analysis are expected. Subsequently, detailed CFD models have been purposely developed and simulated for the $CO_2$ gas coolers with split fins to quantify the effect of the heat conduction through fins. At various operating conditions of both air and refrigerant sides, totally 36 cases were simulated to study the influence of air inlet velocity, air inlet temperature, $CO_2$ pressure and $CO_2$ mass flow rate as well as the heat conduction along fins on the performance of the finned-tube gas coolers with and without split fins.

The novel coupled one-dimensional (1D) and three-dimensional (3D) CFD model has been developed and explained for the finned-tube $CO_2$ gas cooler with or without split fins, which has been detailed explained in Chapter 3. For eliminating the heat conduction through fins, splitting fins are utilized on finned-tube gas cooler. The effects of heat conduction through fins on the performance of the $CO_2$ gas coolers with continuous and split fins are studied by CFD model. The longitudinal heat conduction along fins will degrade the capacity of gas cooler and also the efficiency of its associated refrigeration system. The research results can considerably contribute to the CFD modelling technique for finned-tube $CO_2$ gas coolers with and without split fins, as well as a better understanding of the effects of heat conduction through fins on heat exchanger and system performance. This provides essential strategies for the optimal design of finned-tube $CO_2$ gas coolers.

## 5.2 Design of split fins gas cooler and continuous fins gas cooler

As shown in Figure 5.1(a), the finned-tube $CO_2$ gas cooler in staggered arrangement under consideration consists of 3 depth tube rows along the airflow or longitudinal direction and each row has 18 tubes in the transverse direction. The air flows from bottom to top passing passages between fins and outer tubes while the $CO_2$ refrigerant flows through inner tubes numbered from ‘0’ (inlet) to ‘53’ (outlet) forming cross-counter flow arrangement with the airflow. The specifications of the gas cooler to be modelled are listed in Table 4.1. Conventionally, to simplify the installation process of the heat exchanger, a number of continuous fins are applied, as shown in Figure 5.1(a). In that case, significant heat could be transferred or conducted through the longitudinal fins between two adjacent tube rows. Based on the literature reviews, to enhance the heat exchanger performance, the continuous fins should be replaced with or cut into the split fins between two adjacent tube rows with the larger temperature differences. Correspondingly, as shown in Figure 5.1 (b), the continuous fins are split between the first and the second adjacent tube rows of the heat exchanger. To clarify, the $CO_2$ gas coolers with continuous fins and split fins are named as Gas cooler A and Gas cooler B respectively. The $CO_2$ gas coolers with the same tube circuitry arrangement but different fin designs are therefore modelled, evaluated and analyzed.

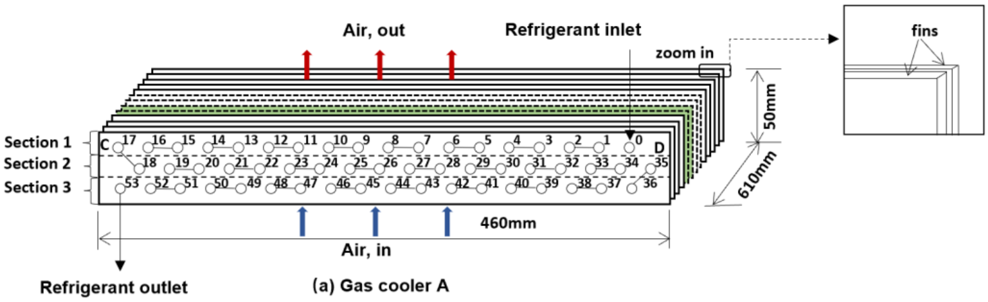

(a) Gas cooler A

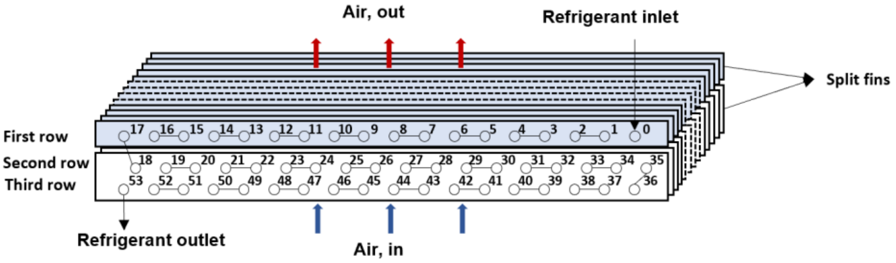

(b) Gas cooler B

Figure 5. 1 Schematic diagram of finned-tube $CO_2$ gas coolers with and without split fins.

## 5.3 CFD modelling description

In this study, the numerical analyses are carried out to investigate fluid heat transfers, pressure drops, temperature variations and heat conduction effects of the finned-tube $CO_2$ gas coolers. To cope with this issue, the overall heat exchanger CFD model is divided into two phase sub-models, namely, Phase I and Phase II models. The heat transfer of the airflow passing through the gas cooler is a combination of two parts including convection heat transfer along the fin surfaces and convection heat transfer through tube external walls. These two part heat transfers can be easily described in Phase I model with representatively one fin passage due to the symmetrical characters of fins along the tubes. Correspondingly, for the Phase I model, one coil element is purposely selected which is comprised of two neighbor fins and tube sections and air domain between them, as highlighted in green color in Figure 5.1(a). Based on such a simplification, airside heat transfer coefficients and pressure drops can be calculated at different operating conditions once the boundary parameters are determined. According to the geometric symmetry and same air flow pattern characteristics in each coil element, the entire heat exchanger is simplified as 10 coil elements to reduce computation time. In such a case, the Phase II model contains 10 fins without fluid domains to predict the performance of the whole gas cooler. The airside heat transfer coefficients of each grid achieved from Phase I model are assigned to the surface of fins and tubes of Phase II model and used as boundary conditions. In these two developed models, C language subroutines are written by Visual Studio 2017 and imported into Ansys Fluent 18.2 by User Define Function (UDF) to calculate the thermal-hydraulic performance of $CO_2$ refrigerant flow. The UDF is then linked with Fluent to achieve the matching and assignment of the heat transfer coefficient in each grid with the Phase II model. For each pipe, energy conversation equation needs to be applied and solved. The tube inner walls apply localized correlations of heat transfer coefficient and hydraulic calculations to predict the temperature, pressure and heat flux of refrigerant along the gas cooler.

Moreover, as the purpose of this study is to explore the effect of heat conduction through fins and reduce its negative influence, it is necessary to model the gas cooler with split fins. To achieve this, the material thermal conductivity value of meshed fins along the split line ('CD' in Figure 5.1(a)) is set to a value close to zero, hence preventing heat transfer from hotter to colder tubes across fin surfaces. Consequently, the gas cooler with continuous or split fins can be simulated using the same CFD models but with differing split line characteristics. Consequently, the performance of a gas cooler with split fins and a gas cooler with continuous fins can both be predicted under various operating conditions using this simple and novel modelling approach. These include the air inlet temperature ranging from 29.4 to 35 ˚C, airflow inlet velocity varying from 1 to 3 m/s, refrigerant pressure changing from 9 to 11 MPa and refrigerant mass flow rate ranging from 0.038 to 0.076 kg/s, detailed operating conditions can be seen in Table 4.4.

For fully developed $CO_2$ single-phase turbulent flow in tubes, Gnielinski's correlation [67] has been widely used for heat transfer calculations [111]. It can approximately predict 90% of the 800 experimental results with deviation less than 20% over a range of 3000 ≤ Re ≤ 5 ×10 6 , 0.5 ≤ Pr ≤ 2000 and L/d ≥10 [116] . The operating parameters in this study are within these ranges. It is noted that the accuracy of Gnielinski's correlation for the calculation of $CO_2$ heat transfer coefficient during its supercritical tube-side heat rejection process has been verified by other researchers. As an example, from the research results by Pettersen et al. [117] , the mean deviation between experiment results and the corresponding calculations with Gnielinski's correlation were 8% for 0.787 mm ID micro-tubes, showing fairly good agreement. However, Gnielinski's correlation could underpredict the heat transfer coefficient of supercritical $CO_2$ cooling processes in macro-tubes compared to experimental data, especially near pseudocritical region where thermophysical properties change rapidly. Dang and Hihara [118] conducted a comparison of $CO_2$ heat transfer coefficient between Gnielinski's correlation and experimental results for a 6 mm ID tube with pressure of 8 MPa, demonstrating that Gnielinski's model underpredicted the data by 30%. According to Olson's [119] report, Gnielinski's correlation underpredicted the data of supercritical

$CO_2$ by 11%–47% for a 10.9 mm ID tube with pressure varied from 7.4 to 13 MPa. From the research carried out by Oh and Son [69] , it is known that the mean deviation of $CO_2$ heat transfer coefficient between Gnielinski's correlation and experimental data for a 7.75 mm ID tube with pressure of 7.5–10 MPa was 36.2%. Nevertheless, Rossetti [120] proposed a CFD modelling of $CO_2$ gas cooler with 8.22 mm ID diameter tubes and pressure of 8 - 9.1 MPa, in which Gnielinski's correlation was used. The results showed that the predicted $CO_2$ exit temperature and heating capacity agreed fairly well with experimental data. In addition, according to the CFD simulation results by Sánchez et al. [121] , the uncertainty of $CO_2$ exit temperature was less than ±3 °C while Gnielinski's correlation was applied. The above-mentioned results indicate the feasibility of using Gnielinski's correlation in supercritical $CO_2$ cooling processes even though larger discrepancies could be caused in the region close to the critical point. On the other hand, since the total thermal resistance of the $CO_2$ gas cooler is normally dominated by that of air side, the discrepancy of $CO_2$ side heat transfer coefficient calculation will not significantly affect the overall heat transfer performance of the $CO_2$ gas cooler. Further, since the investigated $CO_2$ pressures in this paper are above 9 MPa which are somewhat above the critical point, the application of Gnielinski's correlation for the heat transfer calculation is thus acceptable. Furthermore, the bulk average properties are used to calculate the heat transfer coefficient.

Models are meshed by using hexahedral type elements. The boundary conditions used in this study are listed in Table 5.1 . In Phase I model, at the upstream boundary condition, airflow parameters with uniform inlet velocity and temperature are specified. The airside outlet pressure is set as zero to obtain the relative pressure drop between airflow inlet and outlet. As to the tube inner wall, $CO_2$ refrigerant side heat transfer coefficient and temperature are assigned by using UDF. No slip condition is applied to the fin side walls. Once the Phase Ⅰ model of gas cooler is solved, the airside heat transfer coefficient of each grid can be obtained and assigned to fin and tube external wall surfaces of Phase Ⅱ model as the boundary conditions. Therefore, in Phase Ⅱ model, heat transfer coefficients and temperatures of both airflow and $CO_2$ sides are applied as the boundary conditions.

**Table 5. 1 Boundary conditions.**

| Model | Boundary | Condition |
|---|---|---|
| Phase Ⅰ model | Airside inlet | $m_a = u \cdot \rho \cdot A, T = T_{a,in}$ |
| | Airside outlet | Pressure outlet, $P_{gauge} = 0$ |
| | Tube inner walls | HTC = $h_{CO2}, T = T_{CO2}$ |
| | Fin side walls | $u = v = w = 0, \frac{\partial T}{\partial x} = 0$ |
| Phase Ⅰ model | Fin surfaces | $HTC = h_{a,i}, T = T_a$ |
| | Fin side walls | $u = v = w = 0, \frac{\partial T}{\partial x} = 0$ |
| | Tube inner walls | HTC = $h_{CO2}, T = T_{CO2}$ |

The SIMPLE scheme is used to solve the coupling of pressure and velocity. All equations are solved by second order discretization scheme. Values of under-relaxation factors for pressure, density, momentum, energy are 0.3, 1, 0.7, 1 respectively. The convergence criteria of continuity, velocity and energy for Phase Ⅰ model are $10^{-10}$ , $10^{-10}$ and $10^{-13}$ respectively. The predetermined convergence of energy for Phase Ⅱ model is $10^{-13}$. The solution is iterated until convergence is achieved. In the post-processing stage, data extractions and result visualizations can be achieved.

## 5.4 Results and discussion

### 5.4.1 Pressure and velocity contours

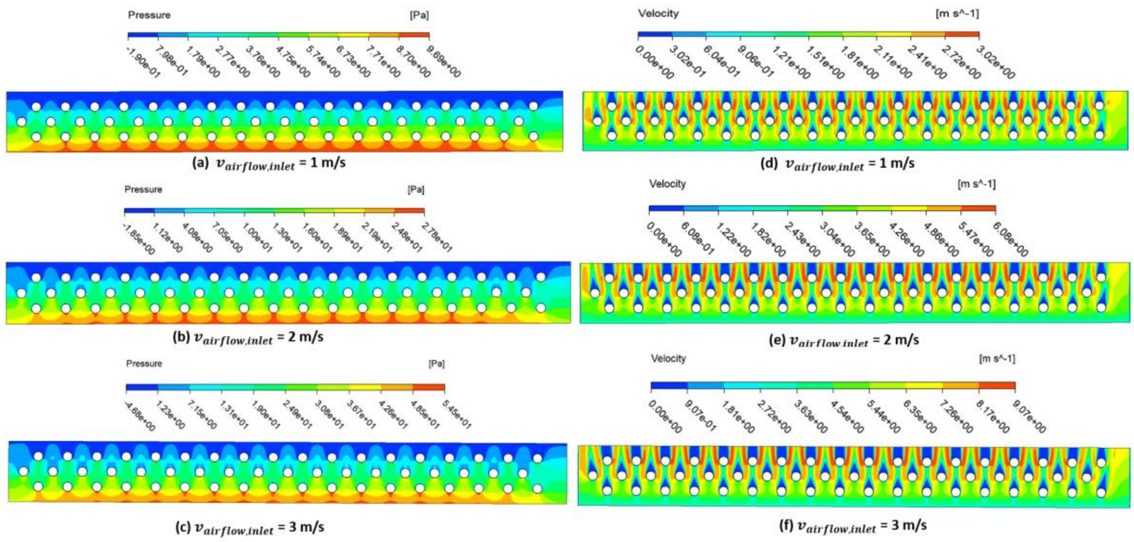

(a) $v_{airflow,inlet}$ = 1 m/s

(d) $v_{airflow,inlet}$ = 1 m/s

(b) $v_{airflow,inlet}$ = 2 m/s

(e) $v_{airflow,inlet}$ = 2 m/s

(c) $v_{airflow,inlet}$ = 3 m/s

(f) $v_{airflow,inlet}$ = 3 m/s

**Figure 5. 2 Temperature contours and velocity contours of airflow (operating condition: $T_{air,in}$ = 302.55K, $m_{CO2}$ = 0.038kg/s, $P_{CO2,in}$ = 9MPa).**

It is known from Figure 5.2 (a) (b) (c) that the pressure decreases along the flow direction of airflow, and higher airflow velocity higher pressure drop. For the airflow velocity distribution, it can be seen in Figure 5.2 (d) (e) (f). The higher inlet velocity contributes to higher airflow velocity in air domain and thus better heat exchange performance. The highest velocity occurs at the edge of first tube row.

### 5.4.2 Airside heat transfer coefficient

There are several factors can affect airside heat transfer coefficient, such as airside temperature, airside velocity and refrigerant flow rate. It is known that the higher air velocity leads to higher heat transfer coefficient. In contrast, the lower airflow temperature, the higher heat transfer coefficient due to the increase in temperature difference, as seen in Figure 5.3 (a). $CO_2$ also can influence the heat transfer coefficient of airflow; it increases with the increased $CO_2$ mass flow rate. Besides, the influence of $CO_2$ mass flow rate is more obvious at higher airflow velocity as shown in Figure 5.3 (b).

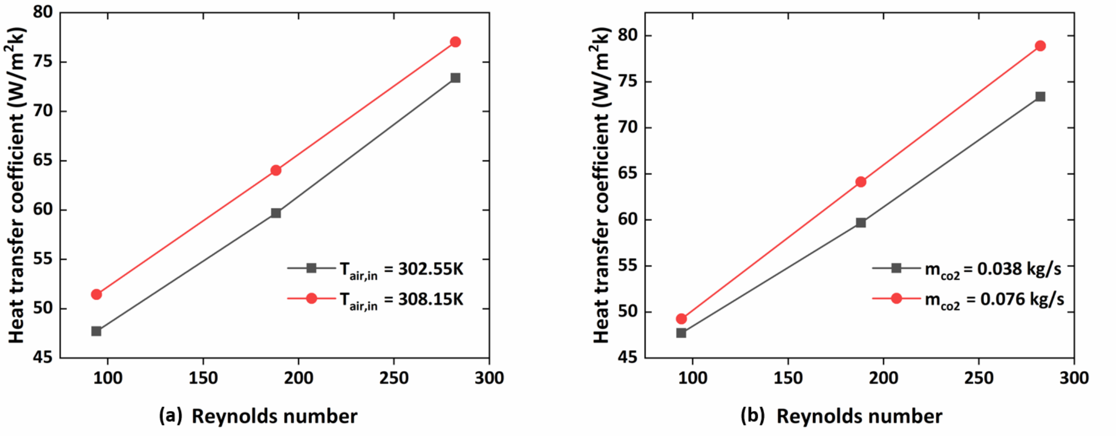

Figure 5. 3 Airflow heat transfer coefficient at different operating conditions.

### 5.4.3 Temperature contours of continuous and split fin surfaces

From the CFD model simulation, the temperature contours of fin surfaces for the coil with continuous and split fins at different air inlet velocity but at the same air inlet temperature are demonstrated in Figure 5.4. The effects of the split fins on the heat conduction through fins are clearly illustrated by the temperature distributions on the fin surfaces. For the coil with continuous fins as presented in Figure 5.4(a) (b) (c), the fin surface temperatures change smoothly starting from the external wall surface of refrigerant inlet tube ‘0’ to the external wall surface of refrigerant outlet tube ‘53’, as shown in Figure 5.1. These also indicate that greater heat will be conducted between the first and second tube rows due to the significant temperature difference between these two tube rows. However, the fin surface temperature differences between the second and the third tube rows are relatively small indicating less heat conduction through the fins. On the other hand, the heat conductions through fins are lessened with higher airflow velocity. Even so, to reduce the effect of heat conduction through the fins, it is more efficient to split the fins between the first and the second tube rows as shown in Figure 5.1(b). Subsequently, as shown in Figure 5.4 (d), (e) and (f), the heat conductions through fins between the first and the second tube rows are totally prevented such that the average fin surface temperature in the first tube row is slightly higher than that of coil with continuous fins. Meanwhile, the fin surface average temperatures along the second and the third tube rows of the coil with split fins are much lower than those of coil with continuous fins. Therefore, at the same operating condition, the average fin surface temperatures of the coil with split fins are relatively lower than those of coil without split fins. To quantify these, the variations of row average fin surface temperatures at different airflow velocities for gas coolers with continuous and split fins are calculated and shown in Figure 5.5. As depicted, for the coil with continuous fins, the row average fin surface temperatures decrease smoothly from row 1 to row 3 due to the higher refrigerant temperatures from row 1 and continuous heat conductions through fins. The higher airflow velocity contributes to lower fin surface temperature due to the enhanced heat transfer between high temperature fin surface and low temperature air flow. For the coil with split fins, the row average fin surface temperatures are not smooth anymore such that there is a big temperature drop from the row 1 fin surface temperature to row 2 fin surface temperature when airflow velocity is fixed. The fin average surface temperature of row 3 is much less than that of row 1. Subsequently, the reduced heat conduction through the fins due to the application of split fins will potentially decrease the refrigerant temperature at the heat exchanger outlet.

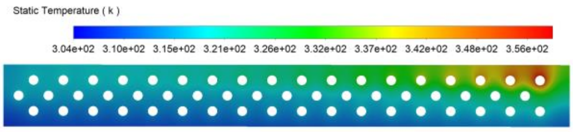

(a) Continuous fin, $u_a$= 1 m/s

(b) Continuous fin, $u_a$= 2 m/s

(c) Continuous fin, $u_a$= 3 m/s

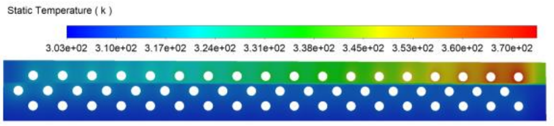

(d) Split fin, $u_a$= 1 m/s

(e) Split fin, $u_a$= 2 m/s

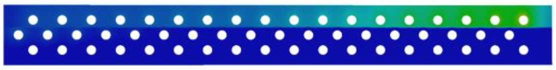

(f) Split fin, $u_a$= 3 m/s

Figure 5. 4 Temperature distribution of fin surfaces for the gas coolers with and without split fins (operating condition: $T_{air,in}$ = 302.55K, $m_{CO2}$ = 0.038kg/s, $P_{CO2,in}$ = 9MPa).

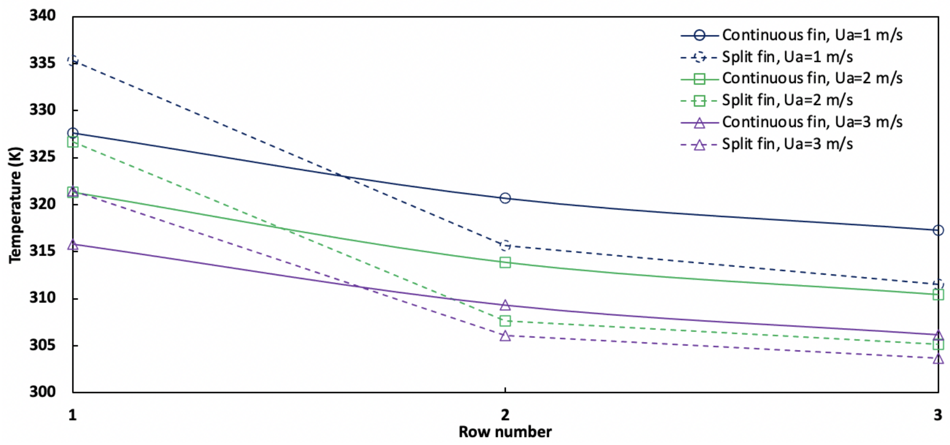

Figure 5. 5 Variations of row average fin surface temperatures at different airflow velocities for the gas coolers with continuous and split fins.

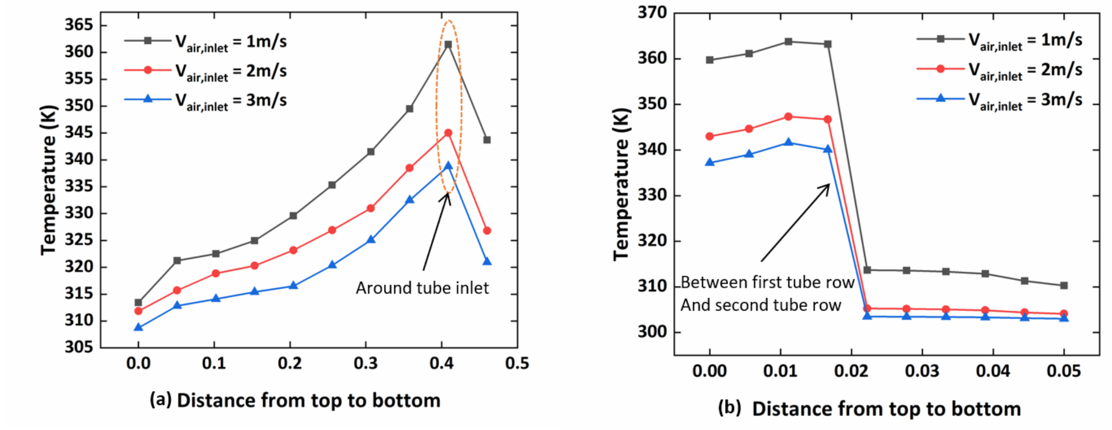

Figure 5. 6 Temperature profile of Line A and line B at different air inlet velocity (operating condition: $T_{air,in}$ = 302.55K, $m_{CO2}$ = 0.038kg/s, $P_{CO2,in}$ = 9MPa).

Figure 5.6 shows the temperature profile of line A and line B (location of lines are shown in Figure 4.12). By comparing with non-split fin, split fin has higher temperature around tube inlet at same operating condition due to heat is block in the section of first tube row by minimizing longitudinal heat condition. The effects of split fins can be more easily observed in Figure 5.6 (b), temperature around second tube row are dramatically decreased and thus higher heat transfer rate between airflow and $CO_2$.

### 5.4.4 Refrigerant temperature profiles for the coil with or without split fins

The $CO_2$ temperature profiles along the tube circuit for the coil with or without split fins at different operating conditions can be predicted by this CFD model and shown in Figure 5.7. The effects of heat conduction between adjacent tubes through fins on the $CO_2$ temperature profiles are clearly demonstrated particularly for the coil without split fins. From the simulation results, it is observed that the refrigerant temperature drops dramatically along the first tube row with tubes numbered from ‘0’ to ‘17’ for both gas coolers. This can be explained that the large temperature difference between $CO_2$ refrigerant and surrounding airflow along the first tube row leads to higher heat release from the refrigerant side to airflow side. However, for the gas cooler with continuous fins, the refrigerant temperature increases gradually from tube ‘27’ until tube ‘36’ due to the effect of longitudinal heat conduction through the fins. This can be explained that the reversed heat conduction through fins from high temperature tube row reheats $CO_2$ refrigerant to a higher temperature value before it is cooled down again by the low temperature airflow through the third tube row. This reversed heat conduction phenomenon is more prominent when the airflow velocity is at a lower value of 1 m/s. By contrast, for the coil with split fins, the longitudinal fin heat conduction between the first and second tube rows is avoided leading to a smoother refrigerant temperature decrease along the refrigerant flow path. The maximum temperature difference at tube '36' between two gas coolers is up to 18.9 °C, which occurs under the operating condition of airflow inlet velocity at 1m/s. It should also be noted that the $CO_2$ temperatures for gas cooler B in the first tube row ('0' to '17') are always higher than those corresponding values of gas cooler A. This is because that heat from the first-row fins of gas cooler B can only dissipate within the first row.

For the coil with or without split fins, the $CO_2$ exit temperature decreases with the increase of airflow inlet velocity, which indicates that the lower airflow velocity cannot offer higher heat transfer coefficient and therefore better thermal-hydraulic performance. The $CO_2$ exit temperature difference between split gas cooler and non-split gas cooler reaches the maximum value when the airflow inlet velocity is down to 1m/s. Under identical air inlet velocity of 1m/s and air inlet temperature conditions of 302.55K and 308.15K, the $CO_2$ exit temperatures can be reduced in average by 4.22K and 3.99 K respectively by splitting fins. Another interesting observation from the simulation results is that at the same operating condition of airflow, the refrigerant temperature decreases more at higher refrigerant pressure. For instance, by comparing Figure 5.7 (a) and (b) for the gas cooler with split fins, $CO_2$ temperature drop is from 10.22 K to 14.78 K respectively when the refrigerant pressure increases from 9 MP to 11MPa. On the contrary, the higher refrigerant mas flow rate leads to the less refrigerant exit temperature decrease when spilt fins are applied.

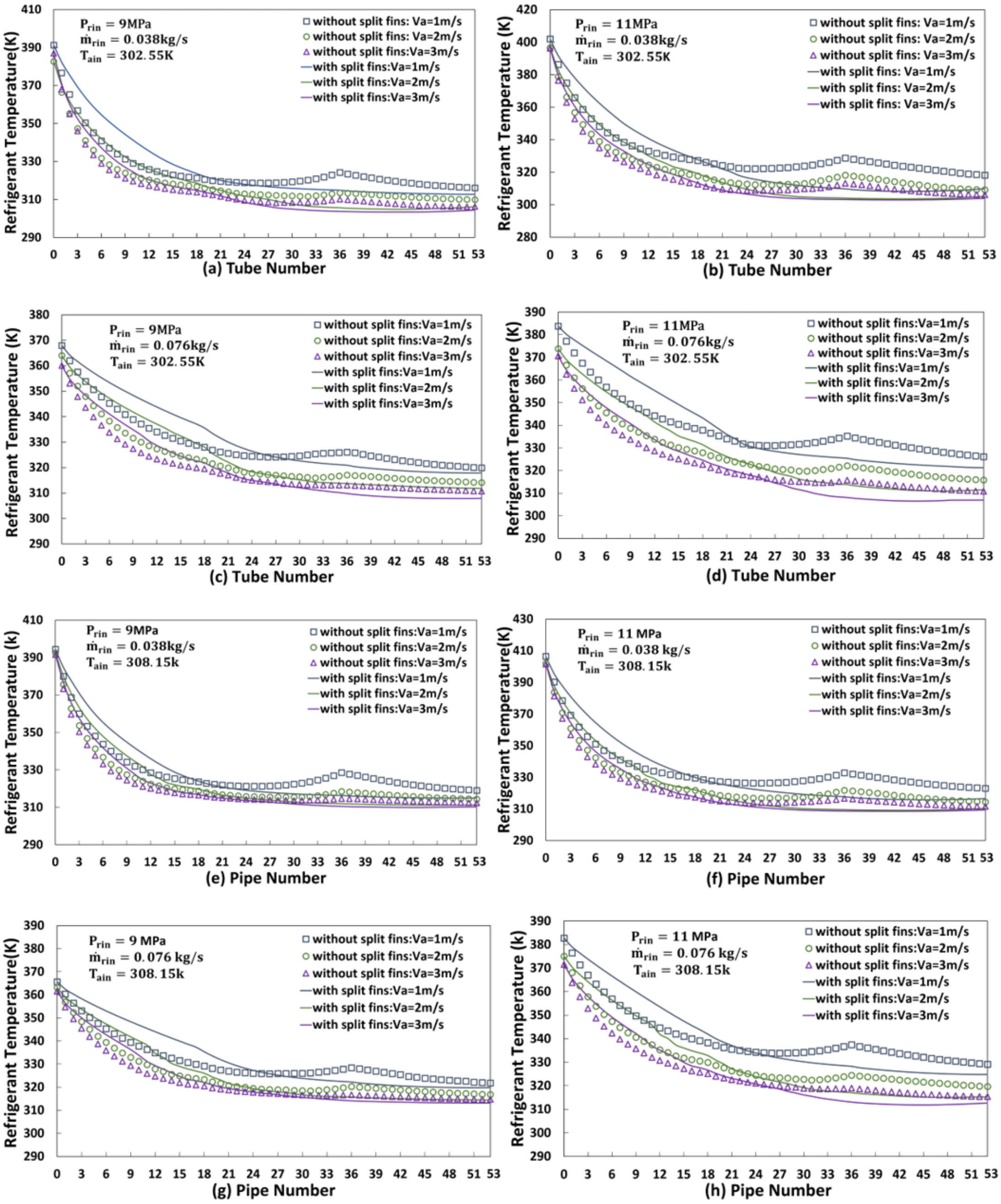

Figure 5. 7 Comparison of refrigerant temperature profiles along pipe flow direction at different operating conditions for the gas coolers with and without split fins.

For all 36 simulated cases, the $CO_2$ exit temperature decrease is in a range of 1.5K to 7.5K when the split fins are applied to the gas cooler. correspondingly, the approach temperature is also reduced at various extents for the coil with split fins due to the blocked heat conduction from the first tube row through fins. The simulation results demonstrate that the heat conduction through fin has important effect on the $CO_2$

temperature profile along the tube circuit while the gas cooler performance can be greatly improved with the design and implement of split fins.

The comparison in approach temperature of gas cooler with and without split fins is shown in Figure 5.8, operating conditions of different cases can be seen in Table 4.4. the lower approach temperature the better thermal match between airflow and refrigerant and thus higher system performance. It is known that the higher velocity and lower temperature of airflow contributes to lower approach temperature. Approach temperature can be reduced significantly by using split fins, the lowest approach temperature is 1.47 K of split-fins gas cooler. And the maximum reduction of approach is 7.5 K. Results also proved that split finned-tube $CO_2$ gas cooler is a promising heat exchanger, which can be used as $CO_2$ gas cooler in the proposed biomass-$CO_2$ Transcritcial Brayton Cycle.

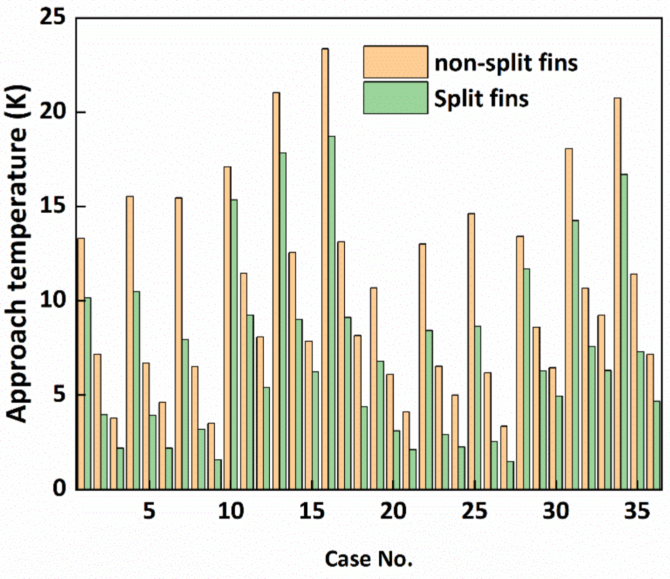

Figure 5. 8 Comparison of approach temperature at different operating conditions for the gas coolers with and without split fins.

### 5.4.5 Heating capacity and cooling COP for the coil with continuous and split fins

It is known that the lower refrigerant exit temperature can contribute to higher heating capacity of the gas cooler and thus better COP in its associated refrigeration system. The coil heating capacities at different operating conditions are therefore simulated for the gas cooler with and without split fins, as shown in Figure 5.9. As depicted, the higher airflow velocity and higher refrigerant mass flow rate lead to increased heating capacity for both gas coolers. In addition, at the same operating condition, as expected, the heating capacity of gas cooler with split fins is always higher than that of gas cooler without split fins particularly at lower air flow velocity. This is contributed by the reduced heat conduction through fins for the coil with split fins and subsequent decreased $CO_2$ exit temperature. Compared to Figure 5.9 (a) and (c), the higher airflow inlet temperature leads to lower coil heating capacity due to reduced temperature difference between refrigerant and airflow sides.  Quantitively, for all circumstances, there are respectively 22% and 10% maximum and average increase rates of heating capacity for gas cooler B when split fins are applied, as seen in Figure 5.10. In addition, at lower air inlet velocity and temperature, the advantages of split finned-tube gas cooler become more obviously compared to those of non-split gas cooler.

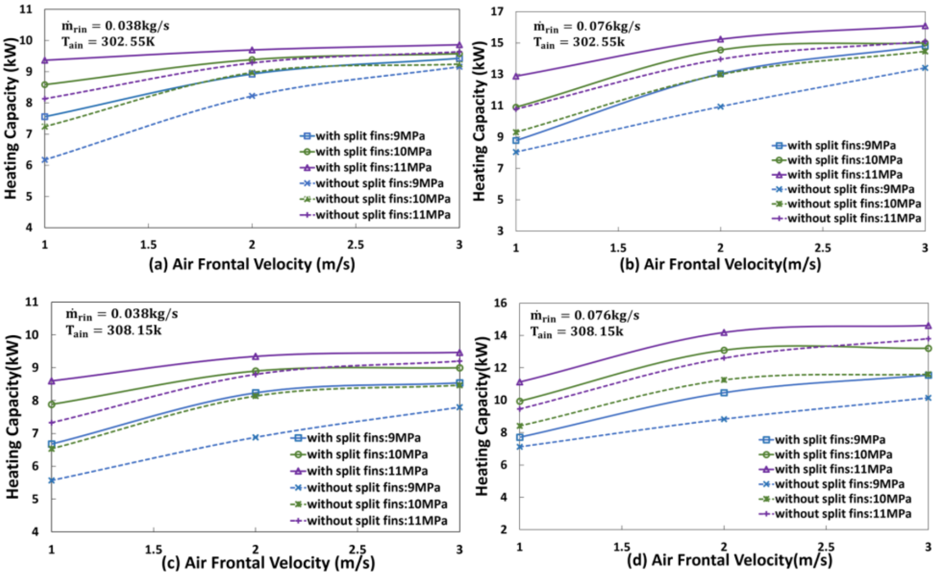

**Figure 5. 9 Comparison of heating capacity at different operating conditions for the gas coolers with and without split fins.**

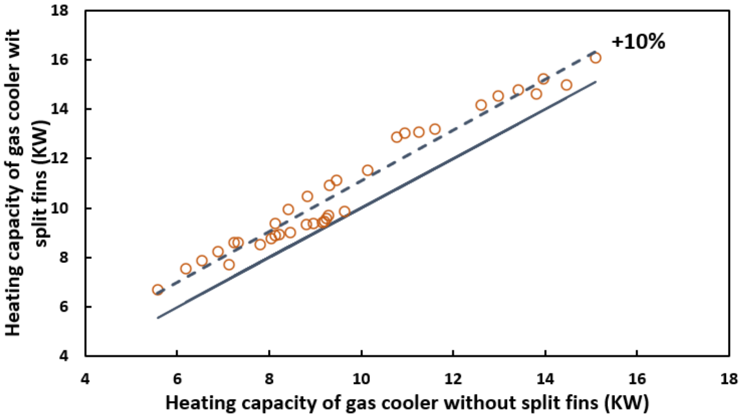

**Figure 5. 10 Improvements of heating capacity by splitting fins.**

The effectiveness of finned-tube gas cooler is defined as the ratio of actual heat transfer to the maximum heat transfer. Effectiveness as a dimensionless parameter evaluates the effect of heat conduction through fins on performance of heat transfer. Table 5.2 and table 5.3 show the improvement of effectiveness by splitting fins. Results indicate that higher air inlet velocity contributes to higher effectiveness. With the increase of air inlet temperature, effectiveness of gas cooler can be reduced. Besides, effectiveness can be significantly increased by the method of split fins. The maximum improvement of 22.28% can be achieved.

**Table 5. 2 Effectiveness of gas cooler with and without split fins ($T_{air,in}$ = 302.55K)).**

| $V_{air}$ (m/s) | $m_{co_2}$ (kg/s) | ε of gas cooler A | | | ε of gas cooler B | | | %improvement | | |
|---|---|---|---|---|---|---|---|---|---|---|
| | | 9 (MPa) | 10 (MPa) | 11 (MPa) | 9 (MPa) | 10 (MPa) | 11 (MPa) | 9 (MPa) | 10 (MPa) | 11 (MPa) |
| 1 | 0.038 | 0.619 | 0.710 | 0.786 | 0.757 | 0.841 | 0.906 | 22.285 | 18.548 | 15.202 |
| 2 | 0.038 | 0.861 | 0.907 | 0.922 | 0.935 | 0.948 | 0.964 | 8.547 | 4.622 | 4.500 |
| 3 | 0.038 | 0.940 | 0.938 | 0.960 | 0.967 | 0.972 | 0.982 | 2.906 | 3.602 | 2.365 |
| 1 | 0.076 | 0.459 | 0.512 | 0.576 | 0.501 | 0.599 | 0.689 | 9.218 | 17.061 | 19.538 |
| 2 | 0.076 | 0.641 | 0.755 | 0.797 | 0.763 | 0.846 | 0.870 | 19.095 | 12.002 | 9.138 |
| 3 | 0.076 | 0.807 | 0.866 | 0.882 | 0.891 | 0.898 | 0.940 | 10.357 | 3.730 | 6.562 |

**Table 5. 3 Effectiveness of gas cooler with and without split fins ($T_{air,in}$ = 308.15K).**

| $V_{air}$ (m/s) | $m_{co_2}$ (kg/s) | ε of gas cooler A | | | ε of gas cooler B | | | %improvement | | |
|---|---|---|---|---|---|---|---|---|---|---|
| | | 9 (MPa) | 10 (MPa) | 11 (MPa) | 9 (MPa) | 10 (MPa) | 11 (MPa) | 9 (MPa) | 10 (MPa) | 11 (MPa) |
| 1 | 0.038 | 0.605 | 0.678 | 0.739 | 0.726 | 0.818 | 0.867 | 19.974 | 20.673 | 17.337 |
| 2 | 0.038 | 0.756 | 0.867 | 0.908 | 0.905 | 0.949 | 0.965 | 19.680 | 9.374 | 6.220 |
| 3 | 0.038 | 0.860 | 0.905 | 0.953 | 0.941 | 0.961 | 0.980 | 9.467 | 6.280 | 2.844 |
| 1 | 0.076 | 0.463 | 0.501 | 0.548 | 0.502 | 0.592 | 0.645 | 8.290 | 18.156 | 17.615 |
| 2 | 0.076 | 0.586 | 0.698 | 0.771 | 0.694 | 0.812 | 0.868 | 18.443 | 16.320 | 12.552 |
| 3 | 0.076 | 0.681 | 0.744 | 0.868 | 0.775 | 0.847 | 0.918 | 13.912 | 13.869 | 5.856 |

The effect of split fins on the gas cooler heating capacity will thus affect the cooling COP of its associated refrigeration system, as shown in Figure 5.11, assuming that the system evaporator exit temperature and pressure are 268.15 K and 3.0459 MPa respectively. The states of compressor inlet and outlet are the same as the evaporator outlet and gas cooler inlet respectively.

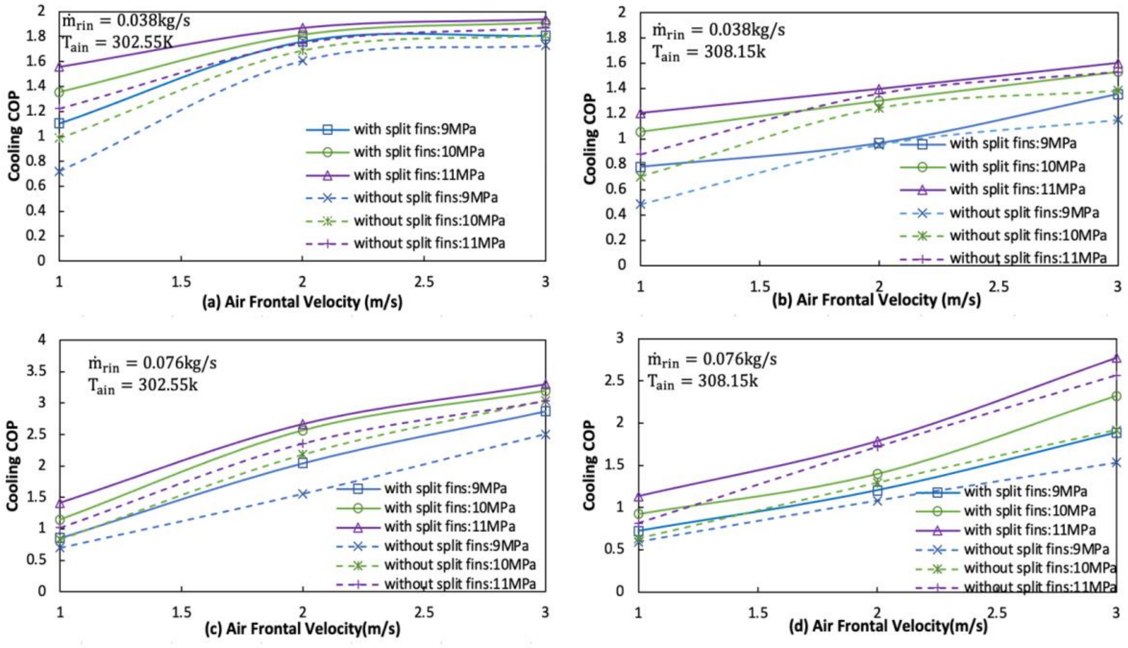

**Figure 5. 11 Variations of cooling COP at different operating conditions for gas coolers with and without split fins.**

As depicted in Figure 5.9, similar effect can be found between the coil heating capacity and system cooling COP at different operating conditions of the gas cooler with or without split fins. The lower air inlet temperature and higher refrigerant mass flow rate can both benefit to the system efficiency. Meanwhile, the cooling COP of the coil with split fins is always higher than that of coil without split fins at any operating condition.

### 5.4.6 Effect of split fins on the performance of coil with different circuitry arrangement

As demonstrated and explained from previous sections, the performance of the gas cooler and its associated system can be greatly improved if split fins are applied to the coil. This is mainly contributed to the significant reduction of heat conduction through fins from the first tube row to the second and the third tube rows due to the larger temperature difference. As seen from Figure 5.7, the average $CO_2$ temperature in the first tube row (tube numbers from ‘0’ to ‘17’) is much larger than that of the second tube row (tube numbers from ‘18’ to ‘35’). By contrast, the average $CO_2$ temperature in the third tube row (tube numbers from ‘36’ to ‘53’) is quite close to that of the second tube row. Subsequently, it is the most effective to split the fins between the first and the second tube rows, as shown in Figure 5.1. It can be imaged that if the average temperature difference between two adjacent tube rows is not significant, the application of split fins between them in the coil might not be effective and necessary. To verify this, in this study, the tube circuitry arrangement of the coil shown in Figure 5.1 is modified and depicted in Figure 5.12 in which the refrigerant flows in turn between the first and the second tube rows before flowing into the third tube row.

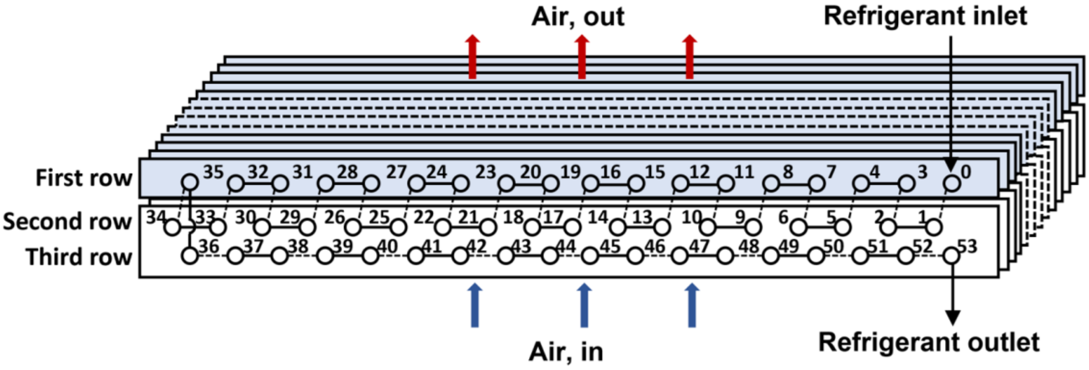

Figure 5. 12 Schematic diagram of the $CO_2$ gas cooler with split fins and modified tube circuitry arrangement (gas cooler C).

With the developed CFD model, the refrigerant temperature profiles along refrigerant flow direction at different operating conditions for the gas coolers with and without split fins are predicted and shown in Figure 5.13. As depicted in Figure 5.13, at each specific operating condition, the average refrigerant temperatures between the first and the second tube rows are quite close. It is also observed that the refrigerant temperature changes wavily from inlet to tube number ‘21’ due to the refrigerant flows in turn between the first and the second tube rows and the different airflow temperatures around these two rows. Consequently, at each operating condition, the refrigerant temperature decreases smoothly in general along the tube circuit until it reaches close to the refrigerant exit for the coil with or without split fins. There are some degrees of refrigerant temperature increases from tube ’50’ to tube ‘53’ because of the heat conduction through the fins from high temperature tubes of ‘1’, ‘2’, ‘5’ and ‘6’ in the second tube row. It thus implies that the split fins between the second and the third row might be more effective for the tube circuitry arrangement shown in Figure 5.12.

The ineffective split fins between the first and the second tube rows for this tube circuitry arrangement can also be demonstrated for their effects on the coil heating capacity, as shown in Figure 5.14. As depicted, at a specific operating condition, the heating capacity is slightly increased when the split fins are applied as shown in Figure 5.12. In average, the heating capacity increase is only about 2% (Figure 5.15) comparing to the 10% increase when the split fins are applied in the coil shown in Figure 5.1. The simulation results further verify that the split fins should be applied between two adjacent tube rows with the largest temperature difference so that the consequent heat conduction through fins can be prevented.

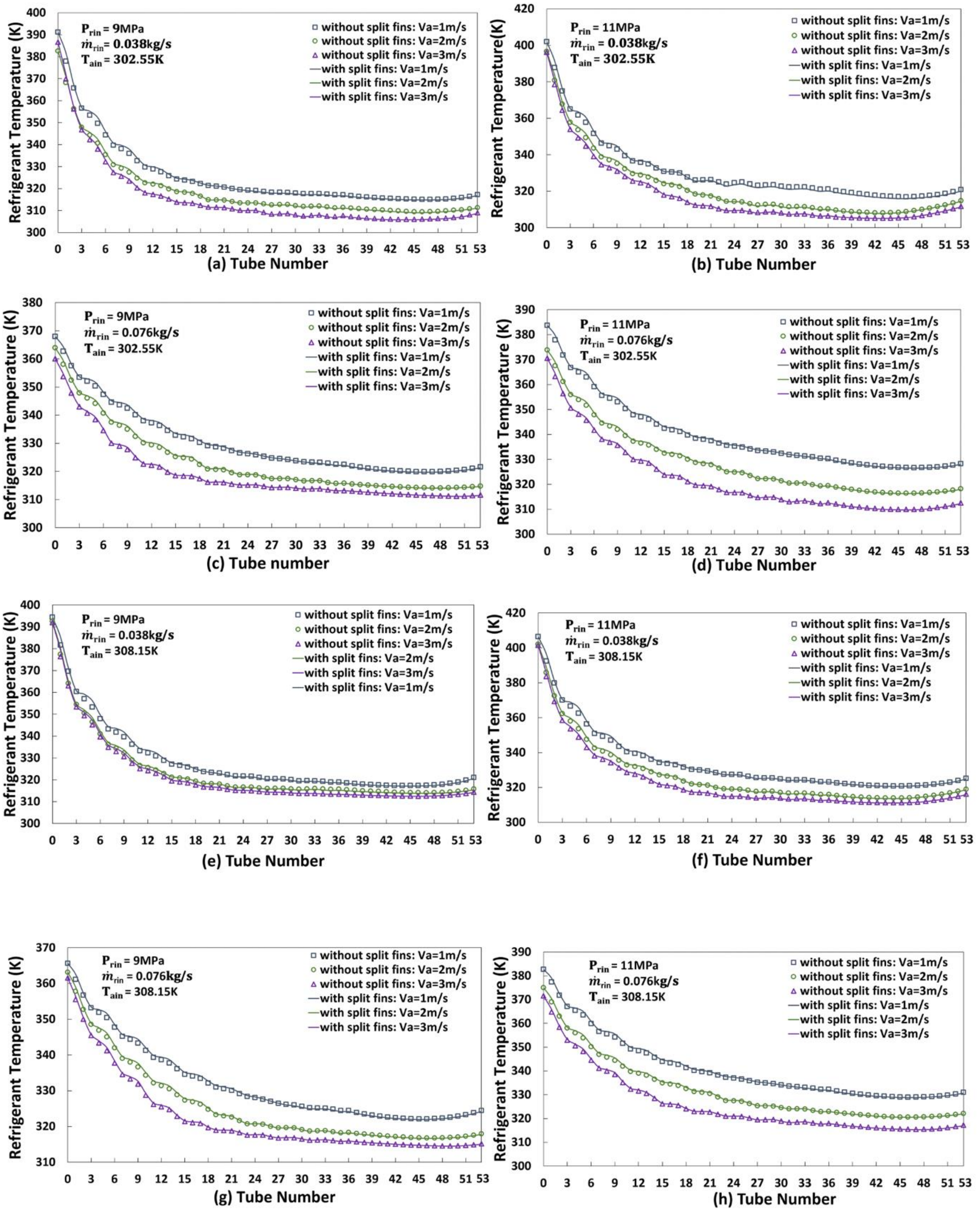

**Figure 5. 13 Refrigerant temperature profiles along refrigerant flow direction at different operating conditions for the gas coolers with and without split fins.**

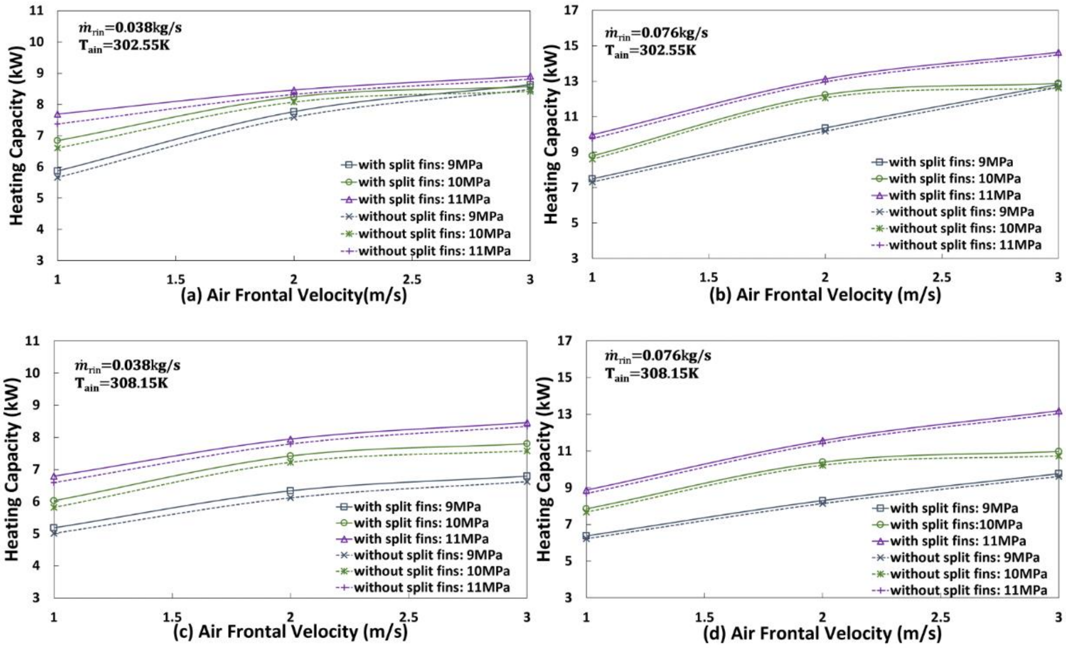

Figure 5. 14 Heating capacity at different operating conditions for the gas coolers with and without split fins.

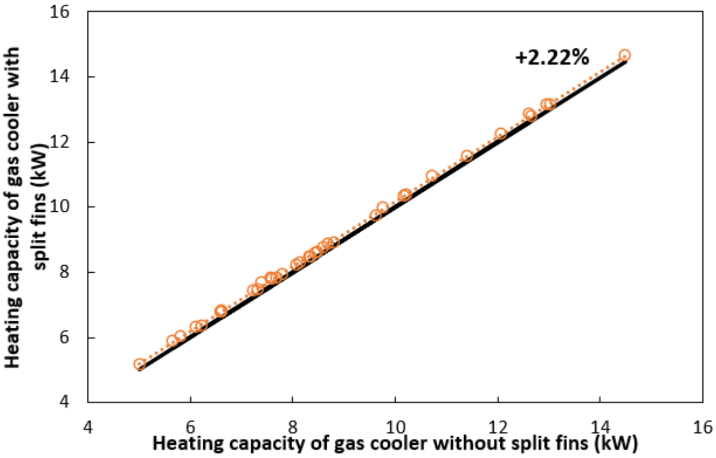

Figure 5. 15 Improvements of heating capacity by splitting fins.

## 5.5 Summary

In order to investigate the effect of heat conduction through fins on the performance of a finned-tube $CO_2$ gas cooler and the cooling COP of its associated transcritical refrigeration system, a new 1D-3D CFD model for the $CO_2$ gas cooler with continuous and split fins has been developed, validated and simulated at different operating conditions. The simulation findings reveal that heat conduction via the fins does exist in the $CO_2$ gas cooler and that it can have a negative impact on the heating capacity and system cooling COP. To cope with these negative impacts, an effective method is to apply split fins in the gas cooler design which has been verified and demonstrated by the developed CFD model.

Heat conduction through fin surfaces should not be neglected for the finned-tube $CO_2$ gas cooler due to large temperature difference between two adjacent tube rows. It is observed that heat is dissipated smoothly through the whole fin surfaces for the coil with continuous fins. On the contrary the heat dissipation is limited and restricted for the coil with split fins. Splitting fins is therefore necessary and an effective method to eliminate most of the heat conduction along fins. The refrigerant flow temperature profile from refrigerant inlet to outlet undergoes smooth decrease along the tube circuit for the coil with split fins. By contrast, for the coil with continuous fins, the refrigerant flow can be reheated in the middle way before it reaches the coil exit due to the negative effect of heat conduction through fins.

$CO_2$ supercritical shell-and-tube gas heater, as another important component which influences performance of biomass-$CO_2$ power generation system significantly, **Chapter 6** will carry out a CFD simulations for this specific $CO_2$ gas heater to investigate the effects of different parameters on its performance and associated biomass-$CO_2$ transcritical Brayton Cycles.

# Chapter 6 - Design Optimization of Shell-and-tube Supercritical $CO_2$ Gas Heater in the Biomass-$CO_2$ Power Generation System

## 6.1 Introduction

Due to the supercritical $CO_2$ flows though the gas heater, shell-and-tube heat exchanger is an appropriate heat exchanger used in this biomass-$CO_2$ transcritical Brayton Cycle system. However, the $CO_2$ gas heater operational efficiency needs to be further improved with high efficient thermal hydraulic behaviors and optimal structural designs.

A well-developed CFD model can be employed and developed for the heat exchangers with different designs and operating conditions, which will be a very useful tool for the optimizations. Such a modelling strategy allows researchers to investigate deeply the fluid flow dynamics and heat transfer behaviors before any further actions are to be taken. Compared to cost intensive experimental investigation and design, a validated CFD model is a more cost-effective and valuable method to perform the optimal design for the heat exchangers.

The conventional shell-and-tube heat exchangers have been investigated experimentally and theoretically for performance evaluations and design optimization. The investigated heat exchangers are mostly applied in industrial processes or refrigeration and heat pump systems while the working fluids are commonly steam, water or different types of refrigerants. In addition, the heat exchangers were normally investigated independently of their associated systems such that their impacts with different operations and designs on the system performances were not quite clear. Due to there are very few investigations on the design and operation of an actual high-temperature biomass flue gas heated supercritical $CO_2$ shell-and-tube gas heater with CFD model and their effects on the associated system performance. Subsequently, in this chapter, detailed CFD models for the $CO_2$ supercritical gas heater has been developed, validated, and simulated at different design and operating conditions. The effects of the heat exchanger designs and operations on a transcritical biomass-$CO_2$ power generation system are also investigated. The research outcomes can be applied for the optimal designs of the heat exchanger and system controls.

## 6.2 System description

The schematic diagram of an integrated biomass unit and $CO_2$ power generation system is presented in Figure 6.1. Each component has been detailed outlined in chapter 3. The high temperature flue gas from the biomass combustion heater passes through the $CO_2$ gas heater to heat the supercritical $CO_2$ fluid directly to a high temperature. The $CO_2$ is then expanded in the turbine simulator to generate power before releasing heat to the recuperator. After that, the $CO_2$ at a subcritical pressure further releases heat through the gas cooler-2 before entering the transcritical compressor to be pressured up. It then absorbs heat through the recuperator before being heated again by the gas heater. The cycle thus repeats. Some important system design parameters include flue gas temperature at 800 °C and mass flow rate at 0.12 kg/s, $CO_2$ turbine inlet temperature at 500°C, pressure at 120 bar and mass flow rate at 0.1272 kg/s, and $CO_2$ turbine outlet pressure at 50.871 bar. Based on this designed operating condition, the $CO_2$ gas heater is singled out and analyzed purposely.

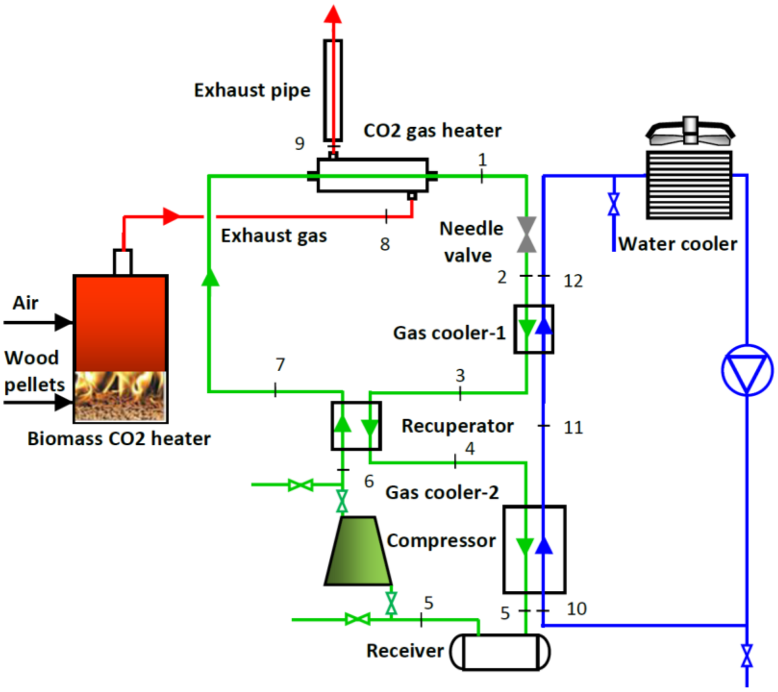

Figure 6. 1 Schematic diagram of integrated biomass unit and $CO_2$ power generation system.

## 6.3 Numerical methodology

### 6.3.1 Physical model

A three-dimensional (3D) geometrical model of the counterflow type supercritical $CO_2$ gas heater has been developed by SOLIDWORKS 2019, as shown in Figure 6.2. Biomass flue gas flows on the shell side while $CO_2$ flows through the tubes. To simplify the modelling process, airflow is selected to represent the biomass flue gas. As depicted, the $CO_2$ gas heater consists of 2 baffles and 13 inner tubes with tube length of 3.472m each, while the diameters of shell pipe and tube are 101.6 mm and 13.7 mm respectively. For investigating comprehensively, the performance of this specific STHX, different operating conditions including varied $CO_2$ mass flow rate, $CO_2$ pressure, flue gas mass flow rate and flue gas temperature are simulated.

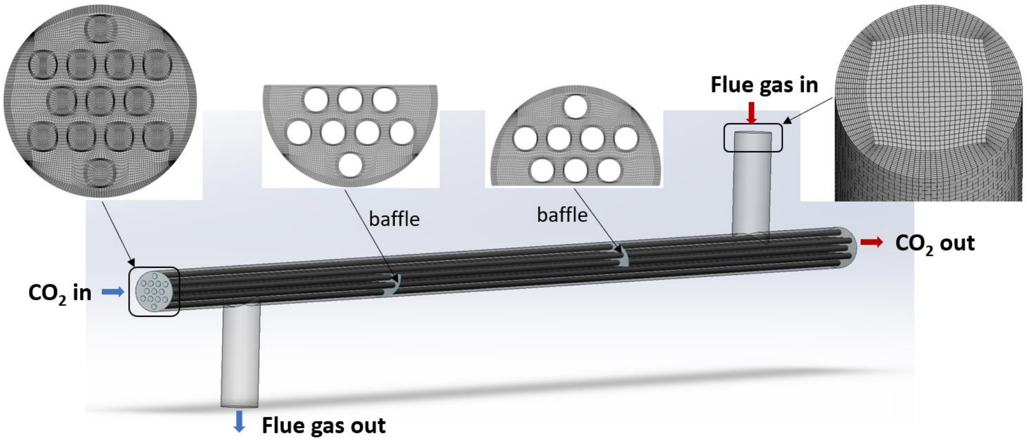

Figure 6. 2 The physical and mesh model of the simulated shell-and-tube heat exchanger.

### 6.3.2 Turbulence model

Due to the turbulent flow involved in this study, turbulence effects should be considered by utilizing an appropriate turbulence model. Subsequently, the Realizable k-ε model is selected for the model development and simulation since it provides superior and accurate performance calculations for rotation, separation and recirculation flows. Besides, such a k-ε model requires less computational time than that of k-ω turbulence model [97]. These have been verified by previous research results from literatures. Yang et al. [122] in their study compared the calculations of fluid pressure drops and heat transfer coefficients on a shell-and-tube heat exchanger by using three different turbulence models. It was found that the realizable k-ε model provided more accurate results by comparing with experimental data. Similar conclusions could also be found in the study of Ozden and Tari [98] in which the realizable k-ε model was applied to predict the fluid pressure drops and heat transfer coefficients of a STHX and obtained more accurate results compared to those with standard k-ε and Sparalt-Allmaras models. Therefore, the Realizable k-ε model has been used for all the simulations in this study.

### 6.3.3 Governing equations

The governing equations for continuity, momentum, energy conservation, turbulent kinetic energy and turbulent energy dissipation equations are described as the following equations.

Continuity equation:

$$\frac{\partial \rho}{\partial \mathrm{t}} + \frac{\partial \rho u_i}{\partial x_i} = 0 \tag{6.1}$$

Momentum equation:

$$\rho \frac{\partial u_i}{\partial \mathrm{t}} + \rho \frac{\partial u_i u_j}{\partial x_i} = -\frac{\partial P}{\partial x_i} + \mu \frac{\partial^2 u_i}{\partial u_j^2} \tag{6.2}$$

Energy equation:

$$\rho c_p \frac{\partial \mathrm{T}}{\partial \mathrm{t}} + \frac{\partial \rho u_i T}{\partial x_i} = \frac{\partial^2 T}{\partial x_i^2} \frac{K}{c_p} \tag{6.3}$$

Turbulent kinetic energy equation:

$$\frac{\partial}{\partial t}(\rho k) + \frac{\partial}{\partial x_j}\left(\rho k u_j\right) = \frac{\partial}{\partial x_j}\left[(\mu + \frac{\mu_t}{\sigma_k}) \frac{\partial k}{\partial x_j}\right] + \Gamma - \varepsilon \tag{6.4}$$

Turbulent energy dissipation equation:

$$\frac{\partial}{\partial t}(\rho \varepsilon) + \frac{\partial}{\partial x_j}\left(\rho \varepsilon u_j\right) = \frac{\partial}{\partial x_j}\left[(\mu + \frac{\mu_t}{\sigma_\varepsilon}) \frac{\partial \varepsilon}{\partial x_j}\right] + C_1 \Gamma \varepsilon - C_2 \frac{\varepsilon^2}{k + \sqrt{\nu \varepsilon}} \tag{6.5}$$

where $\Gamma = \mu_t \left(\frac{\partial u_i}{\partial x_j} + \frac{\partial u_j}{\partial x_i}\right) \frac{\partial u_i}{\partial x_i}, \mu_t = \rho C_\mu \frac{k^2}{\varepsilon}$.

The model constants $C_1, C_2, \sigma_k, \sigma_\varepsilon$ are defined as following values:

$$C_1 = 1.44 \quad C_2 = 1.9 \quad \sigma_k = 1.0 \quad \sigma_\varepsilon = 1.2$$

### 6.3.4 Data reduction

The total heat transfer rates of shell and tube sides can be calculated in Eq.6.6 and Eq.6.7 respectively.

$$Q_s = \dot{m}_s\left(h_{s,in} - h_{s,out}\right) \tag{6.6}$$

$$Q_t = \dot{m}_t\left(h_{t,out} - h_{t,in}\right) \tag{6.7}$$

The average heat transfer rate can thus be determined by Eq.6.8:

$$Q_{av} = \frac{Q_s+Q_t}{2} \tag{6.8}$$

The overall heat transfer coefficient of the heat exchanger based on the outer surface area of tubes can be expressed as the following equation:

$$U = \frac{Q_{av}}{F\times L\times N_t\times\pi d_o\times\Delta T_m} \tag{6.9}$$

where, F is a correction factor to counterflow calculation for the heat exchanger, $\Delta T_m$is the logarithmic mean temperature difference (LMTD) obtained by inlet and outlet fluid temperatures of both shell and tube sides.

$$\Delta T_m = \frac{(T_{s,in}-T_{t.out})-(T_{s,out}-T_{t.in})}{ln(T_{s,in}-T_{t.out})-ln(T_{s,out}-T_{t.in})} \tag{6.10}$$

The shell side fluid flow heat transfer coefficient can be determined by Eq.6.11

$$HTC_s = \frac{1}{\frac{1}{U}-\frac{1}{HTC_t}\frac{d_o}{d_i}-\frac{d_o}{2k}ln\frac{d_o}{d_i}} \tag{6.11}$$

where $h_t$ is the tube side heat transfer coefficient calculated by CFD.

The friction factors of tube and shell sides can be obtained by Eq. 6.12 and Eq. 6.13 respectively.

$$f_t = \frac{\Delta P_t d_i}{2\rho u_m^2 L} \tag*{6.12}$$

$$f_s = \frac{2\Delta P_s D_e (\frac{\mu_b}{\mu_{wall}})^{0.14}}{(N_b+1) D_s \rho u_m^2} \tag*{6.13}$$

where $\mu_b$ is the viscosity of the shell-side fluid at bulk temperature, and $\mu_{wall}$ is the viscosity of the tube-side fluid at wall temperature.

In this study, the calculated tube side heat transfer coefficients from the CFD model are compared with that of Petukhov-Kirillow correlation as Eq.6.14 [123].

$$Nu = \frac{(f/2) Re Pr}{12.7\sqrt{\frac{f}{2}}\left(Pr^{\frac{2}{3}}-1\right)+1.07} \tag*{6.14}$$

In Eq.(14) , it requires the value of friction coefficient $f$:

$$f = (1.58\, ln(Re) - 3.28)^{-2} \tag*{6.15}$$

As explained previously, it is known that Kern and Bell-Delaware methods are the most reliable means to calculate shell side heat transfer coefficients and pressure drops of a STHX, which are thus used to validate the CFD model developed by this study:

$$\frac{h_{Kern,s} D_e}{k} = 0.36 \left(\frac{D_e G_s}{\mu}\right)^{0.55} \left(\frac{c_p \mu}{k}\right)^{\frac{1}{3}} (\frac{\mu_b}{\mu_{wall}})^{0.14} \tag*{6.16}$$

$$f_{Kern,s} = \exp(0.576 - 0.19\, ln(Re_s)) \tag*{6.17}$$

$$HTC_{Bell-Delaware,s} = h_{id} J_c J_l J_b J_s J_r \tag*{6.18}$$

where $J_c, J_l, J_b, J_s, J_r$ are correction factors.

The ideal heat transfer coefficient, $HTC_{id}$ for pure cross flow is given by:

$$HTC_{id} = j_i C_{ps} (\frac{m}{A_s})(Pr)^{-\frac{2}{3}}(\frac{\mu_s}{\mu_{s,w}})^{0.14} \quad 6.19$$

$$\Delta P_{Bell-Delaware,s} = \Delta P_c + \Delta P_w + \Delta P_e \quad 6.20$$

### 6.3.5 Grid independency test

The CO$_2$ gas heater was meshed in Ansys ICEM CFD 19.2 with hexahedral type elements as indicated in Figure 6.2. To ensure the accuracy of this CFD simulation results, grid independency test was conducted by comparing pressure drop and heat transfer coefficient calculations of shell side for different numbers of grid cells, as shown in Figure 6.3. Four different meshes of 2,286,926, 2,632,068, 3,057,565 and 3,418,240 were performed to achieve the optimized grid number. It is found that the relative difference of fluid shell side pressure drops and heat transfer coefficient calculations between mesh numbers of 3,057,565 and 3,418,240 are less than 1%. Taking into account the compromise between the model accuracy and computational time, the model with 3,057,565 cells is used for the entire simulation cases.

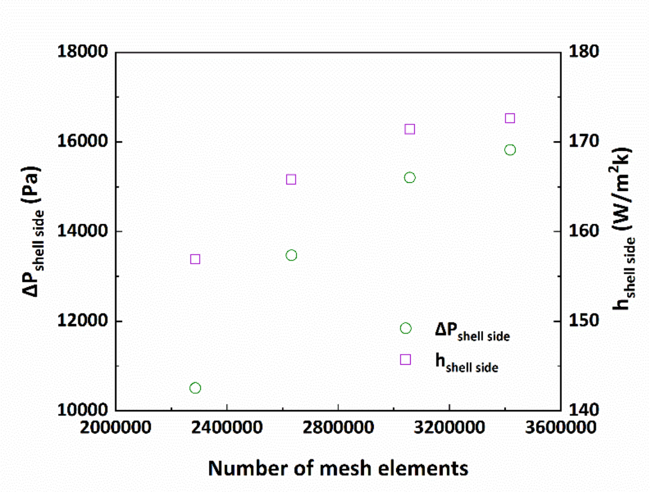

Figure 6. 3 Variations of pressure drop and heat transfer coefficient of shell side with different mesh sizes.

### 6.3.6 Boundary conditions

For both shell and tube sides, fluid temperatures and velocities are applied as inlet boundary conditions. Meanwhile fluid outlet boundary conditions are set as pressure outlets. The model simulation operating conditions are specified in Table 6.1. Correspondingly, the fluid pressure is set to atmospheric pressure for the shell side outlet while the fluid pressures of tube side outlet vary from 8 to 28 MPa. The biomass flue gas temperatures vary from 873.15 to 1273.15 K while its mass flow rates are in the range of 0.08 to 0.16 kg/s. Meanwhile, the $CO_2$ fluid mass flow rates change from 0.08 to 0.16 kg/s and temperature from 495 to 745 K. To investigate the effect of different operating parameters on performance of this STHX, in each simulation, only one variable is changed, and all other parameters are kept as constant design values as indicated in Table 6.1. The $CO_2$ and airflow thermophysical properties of density, viscosity, specific heat capacity and thermal conductivity are all functions of temperature and pressure, which are obtained from REFPORP 8.0 software. The functions are written with C program under the platform of Visual Studio 2017. These thermophysical properties are then defined by User Define Function (UDF) in ANSYS Fluent 19.2. The Simple scheme is selected for coupling the pressure and velocity fields. The convergence criterion is set with energy residual less than $10^{-7}$ and all other residuals less than $10^{-3}$.

**Table 6. 1 Simulated operating conditions.**

| Biomass flue gas | | Carbon dioxide | | |
|---|---|---|---|---|
| Temperature (K) | Mass flow rate (kg/s) | Temperature (K) | Mass flow rate (kg/s) | Pressure (MPa) |
| 873.15~1273.15 | 0.08~0.16 | 495~745 | 0.08~0.16 | 8~28 |
| 1073.15(design) | 0.12(design) | 595(design) | 0.1272(design) | 12 (design) |

## 6.4 Model results and validations

### 6.4.1 Validations

Before carrying out detailed CFD simulations, one simulated case based on designed operating conditions was conducted and the results were compared with empirical correlations. As Kern and Bell-Delaware methods are two most commonly used routines to calculate shell side pressure drop and heat transfer coefficient of a shell-and-tube heat exchanger, the CFD simulation results of shell side heat transfer and hydraulic parameters were thus compared with those calculated by Kern and Bell-Delaware methods, as shown in Figure 6.4(a). Both simulation and correlation results show that the heat transfer coefficient and pressure drop of flue gas increase with higher Reynolds number. Meanwhile, as depicted, the maximum deviations between simulation results and calculations by Kern method for flue gas heat transfer coefficient and pressure drop are 2.1% and 25% respectively while the maximum deviations between simulation results and calculations by Bell-Delaware for flue gas heat transfer coefficient and pressure drop are 4.6% and 7.6% each. Although all the deviations are within acceptable ranges, the CFD mode simulations match relatively well with those calculated by the Bell-Delaware method. This could also present another evidence of the applicability of the Bell-Delaware method for the STHX at the specified design conditions.

For the tube side heat transfer coefficients and pressure drops, as shown in Figure 6.4 (b), the comparisons are made between the CFD simulations and the calculation results by the well-acknowledged empirical correlations from Petukhov-Kirillow [123]. As depicted, the higher Reynolds number of $CO_2$ flow results in higher heat transfer coefficient and pressure drop of tube side. The maximum deviations are 4.9% and 4% for tube side heat transfer coefficient and tube side pressure drop respectively. The simulation results show good agreement with the empirical correlations. In addition, at the designed operating condition, the calculated heat exchanger heating capacity is 34.24 kW by the CFD model, compared to 26.86 kW from the manufacturer’s data. The comparison results can demonstrate the reasonable accuracy of the developed CFD model. As a result, it can be concluded that the validated model can predict accurately the heat transfer and hydraulic behaviors  of the $CO_2$ gas heater.

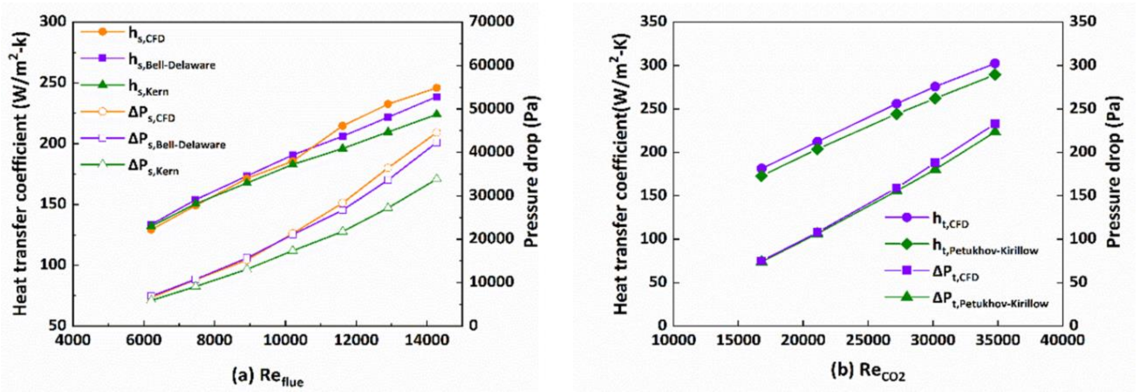

(a) $Re_{flue}$ (b) $Re_{CO2}$

**Figure 6. 4 Comparisons of shell and tube side heat transfer coefficients and pressure drops with empirical correlations.**

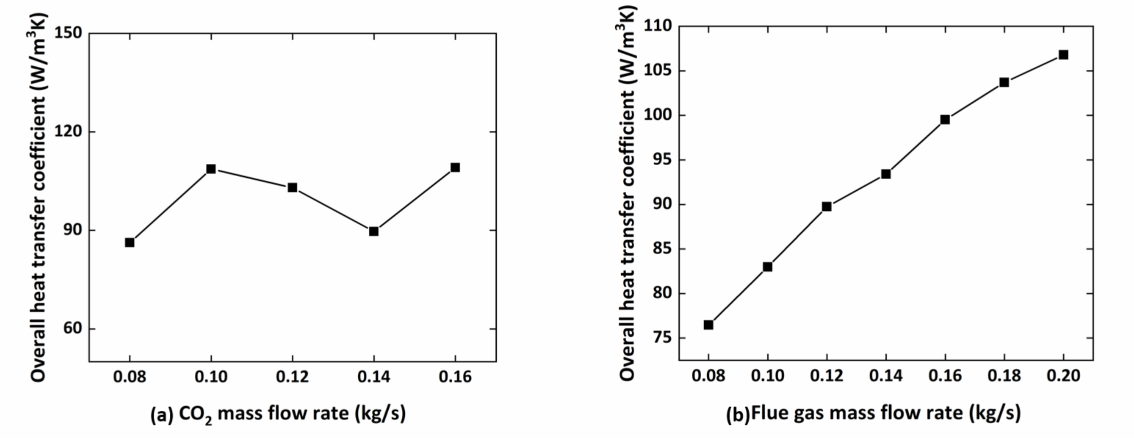

(a) $CO_2$ mass flow rate (kg/s) (b)Flue gas mass flow rate (kg/s)

**Figure 6. 5 Overall heat transfer coefficient at different flue gas mass flow rate and $CO_2$ mass flow rate ($T_{flue}$ = 1073.15K, $P_{CO2}$ = 12 MPa).**

Figure 6.5 show the overall heat transfer coefficient. With the increase of $CO_2$ mass flow rate, overall heat transfer coefficient fluctuates around a stable value of 100 $W/m^2K$

as seen in Figure 6.5 (a). In contrast, with the increased in flue gas mass flow rate from 0.08 kg/s to 0.2 kg/s, overall heat transfer coefficient increased from 77 $W/m^2K$ to 107 $W/m^2K$, as seen in Figure 6.5 (b).

### 6.4.2 Temperature contours

From the CFD simulation results, temperature contours of the shell-and-tube heat exchanger at central plane under different flue gas mass flow rates are shown in Figure 6.6. The effects of shell side fluid mass flow rates on temperature distributions are clearly illustrated. It can be observed that at each mass flow rate, the temperature of flue gas decreases gradually from its inlet to outlet, and meanwhile the temperature of $CO_2$ increases progressively from its inlet to outlet. The higher flue gas mass flow rate is, the higher temperatures are at both flue gas outlet and $CO_2$ outlet. This is due to the higher velocity of flue gas improves the heat exchanger performance between hot and cold fluids, and thus the fluid heat transfer coefficient on shell side can be enhanced. In quantity, as shown in Figure 6.4, when the shell side mass flow rate increases from 0.08 kg/s to 0.16 kg/s , correspondingly Renault number $Re_{flue}$ changes from 6211 to 27444, the shell side fluid heat transfer coefficient growths from 129.3 $W/m^2K$ to 214.7 $W/m^2K$. The logarithmic mean temperature difference (LMTD) is also an important factor for heat exchanger design which is a driving force for heat transfer from hot fluid to cold fluid. The LMTDs are calculated as 214.6 K, 225.9 K and 230 K at the conditions of flue gas mass flow rates of 0.08 kg/s, 0.12 kg/s and 0.16 kg/s respectively. However, the higher shell side fluid mass flow rate leads to larger pressure drops. Subsequently, the flue gas pressure drops are 6569.97 Pa, 15205.20 Pa and 28353.50 Pa respectively corresponding to those three different flue gas mass flow rates. As such, the increment rate of pressure drop is much higher than that of shell side heat transfer coefficient. It is known that the higher pressure drop is, the higher power consumption of exhaust fan will be. Therefore, there should exist an optimal flue gas mass flow rate which can not only improve the performance of heat exchanger but also avoid consuming excess energy for exhaust fan.

The temperature contours of two cross sections just after those two baffles along the flue gas flow direction at flue gas flow rates of 0.08 kg/s, 0.12 kg/s and 0.16 kg/s are shown in Figure 6.7. As depicted, at each flue gas flow rate, the flue gas temperatures at the opening area of each baffle cross section is much higher than those of blocked area of the same cross section.

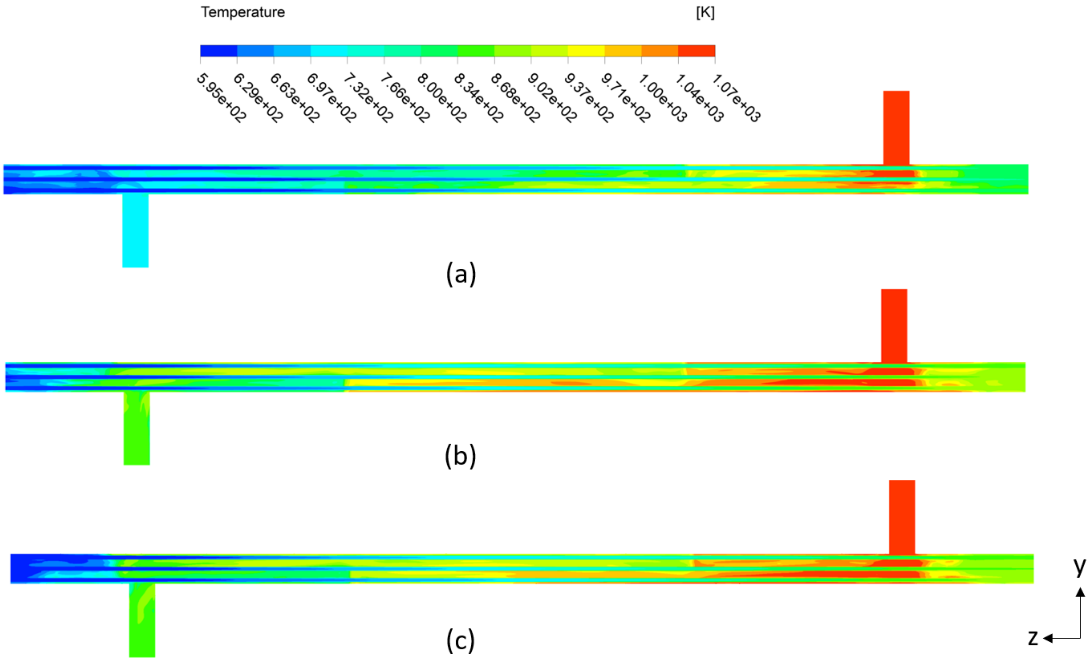

(a)

(b)

(c)

**Figure 6. 6 Temperature contours of the gas heater at central x-axial plane for flue gas mass flow rate: (a) 0.08 kg/s; (b) 0.12 kg/s; (c) 0.16 kg/s. ($T_{flue\ gas}$=1073.15 K,$m_{CO2}$=0.1272 kg/s, $P_{CO2}$=12 MPa)**

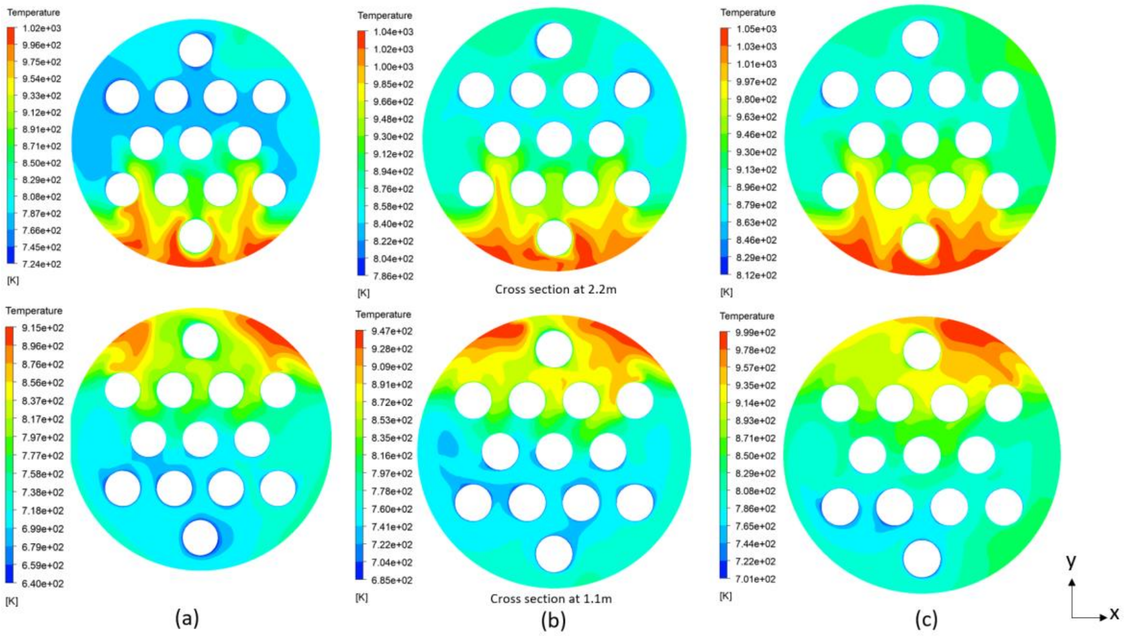

**Figure 6. 7 Temperature contours of flue gas at cross sections of 1.1m and 2.2m along the shell tube direction for flue gas mass flow rate: (a) 0.08 kg/s; (b) 0.12 kg/s; (c) 0.16 kg/s. $T_{\text{flue gas}}$=1073.15 K, $m_{CO2}$=0.1272 kg/s, $P_{CO2}$=12 MPa).**

The detailed flue gas and $CO_2$ temperature profiles averaged at each cross section along shell length direction (starting from $CO_2$ flow inlet) are simulated and shown in Figure 6.8. As demonstrated, the $CO_2$ fluid temperature increases smoothly from its inlet to the outlet except for a short distance between $CO_2$ flow inlet and flue gas outlet due to the stagnant flue gas over there. However, although the flue gas temperature gradually decreases from its inlet to outlet ports, but it is abruptly dropped at two sections just behind those two baffles located at 1.1 m and 2.2 m along the shell length direction, which can be explained by the results shown in Figure 6.7. With the increase of flue gas velocity, the flue gas temperature at each cross section is relatively higher. Besides, the flue gas temperatures close to two stagnant ends are relatively lower than those in the mainstream nearby. In addition, the higher the flue gas mass flow rate is, the hotter the $CO_2$ flow can be heated. This is because that the higher flue gas flow rate can enhance the heat transfer on the shell side and thus the heating capacity of the heat exchanger.

Subsequently, the $CO_2$ flow outlet temperatures are 793.58 K, 838.9 K and 868.63 K at flue gas mass flow rates of 0.08 kg/s, 0.12 kg/s and 0.16 kg/s respectively. Correspondingly, the flue gas outlet temperatures are 755.5 K, 812.7 K and 852.46 K each.

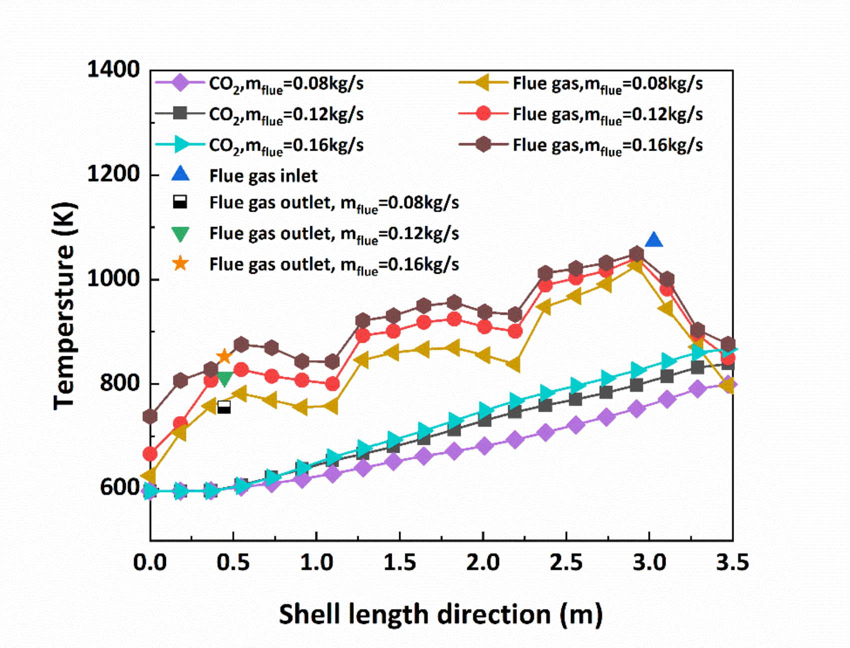

**Figure 6. 8** $CO_2$ and flue gas temperature profiles along shell length direction at different flue gas mass flow rate.

### 6.4.3 Velocity distributions and streamlines

Figure 6.9 shows the velocity distributions of flue gas at its inlet and outlet cross-section planes with those three different flue gas mass flow rates. It can be observed that vortexes can be formed behind tubes at the inlet of flue gas flow. As depicted, the higher velocities occur at the areas between tubes across the second tube row from the top. With the flue gas flows perpendicularly through the tube bundles, its velocity is reduced gradually and is distributed unevenly, as such the flue gas velocity reaches to the lowest at the bottom zones of those cross sections. This in turn reduces the local heat transfer between shell and tubes since the increased number of tubes in the flue gas flow direction prevents sufficient flue gas flow through the tube bundles. In addition, the velocity at the bottom zones on the inlet cross-section plane is less influenced by flue gas mass flow rate since the flue gas tends to flow along the tubes to the direction of flue gas outlet. However, with the increase of flue gas mass flow rate, the velocity at the bottom zones on the outlet cross-section plane is affected more due to the position of flue gas outlet which can thus enhance the local heat transfer there.

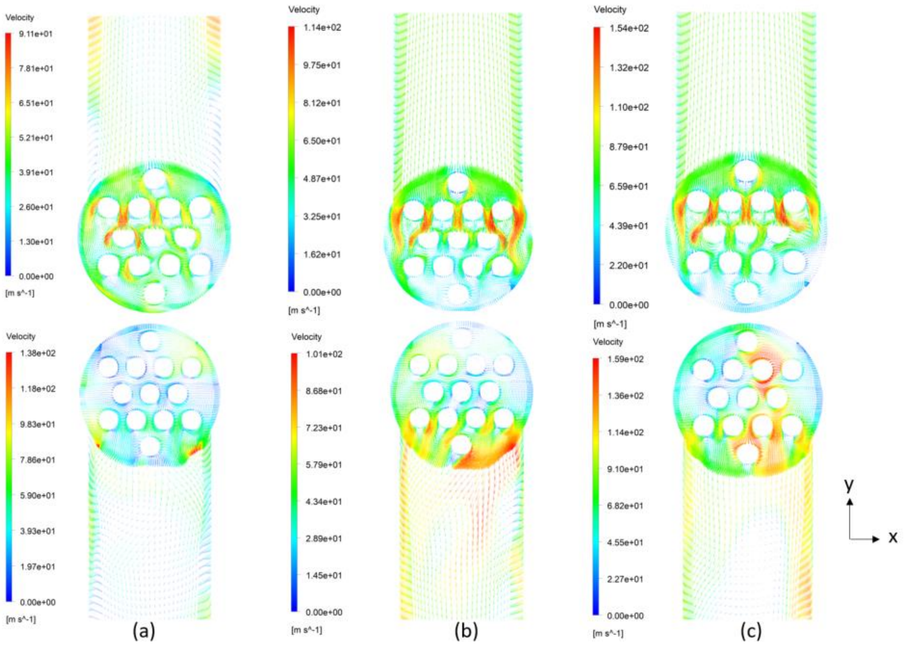

(a) (b) (c)

**Figure 6. 9 Velocity distributions at inlet and outlet planes at flue gas mass flow rate of: (a)0.08 kg/s; (b) 0.12 kg/s; (c) 0.16 kg/s. ($T_{\text{flue gas}}$=1073.15 K, $m_{CO2}$=0.1272 kg/s, $P_{CO2}$=12 MPa)**

The streamlines of flue gas flow through the tube bundles along shell are shown in Figure 6.10. For the heat exchanger, baffles are used to suspend the tube bundles and direct shell side fluid flow along the tubes. The highest flue gas velocity occurs in the cross areas of baffles due to the reductions of flue gas cross flow areas. Recirculation zones are therefore formed when flue gas flow passes across each baffle. The flue gas velocities in these zones are relatively low since part of the flue gas flow is stagnated and separated from the main flue gas stream flowing through the tube bank. Although the baffles are able to improve heat transfer behaviors, the shell side fluid pressure drop will be inevitably increased, and therefore the subsequent pumping power demand. Furthermore, there are two stagnated regions for the shell-side flue gas flow in which one is between $CO_2$ fluid inlet and flue gas outlet and another is between the flue gas inlet and $CO_2$ fluid outlet. The flue gas temperatures in these two stagnated regions are relatively low such that the heat transfers between the flue gas and $CO_2$ fluid in these two regions are insignificant. To enhance the heat transfer, it is thus suggested that the locations of flue gas inlet and outlet ports be installed as close as possible to each heat exchanger end.

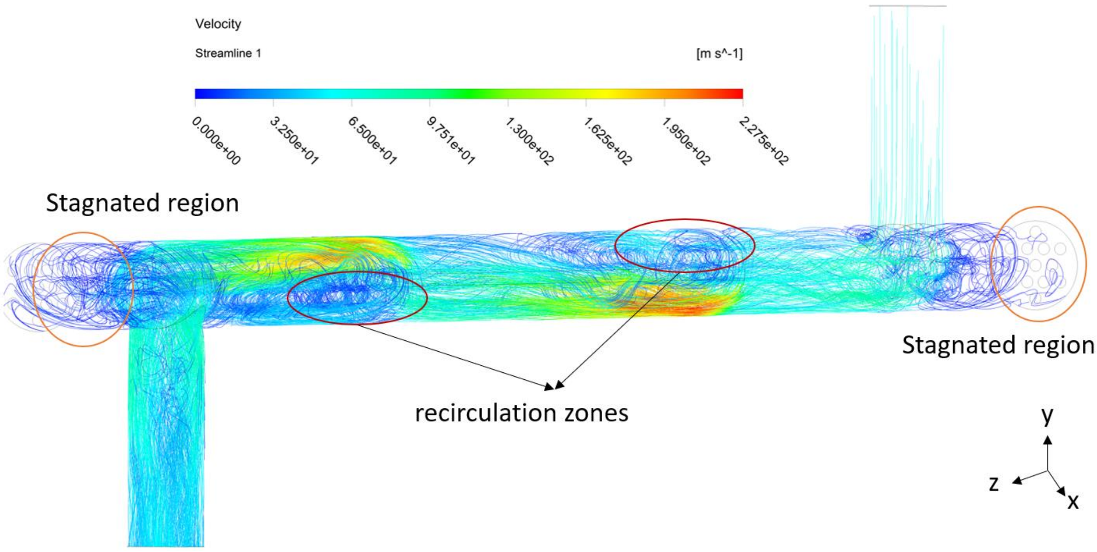

**Figure 6. 10 Velocity streamlines of shell side flue gas. ($m_{flue}$=0.12 kg/s, $T_{flue\ gas}$=1073.15 K, $m_{CO2}$=0.1272 kg/s, $P_{CO2}$=12 MPa)**

For more detailed understanding of the flue gas velocity distribution, Figure 6.11 shows the flue gas velocity with different mass flow rate. Due to the long length and few baffles of this shell-and-tube heat exchanger, the lower flue gas mass flow rate, more turbulent in shell tube and also the lower velocity.

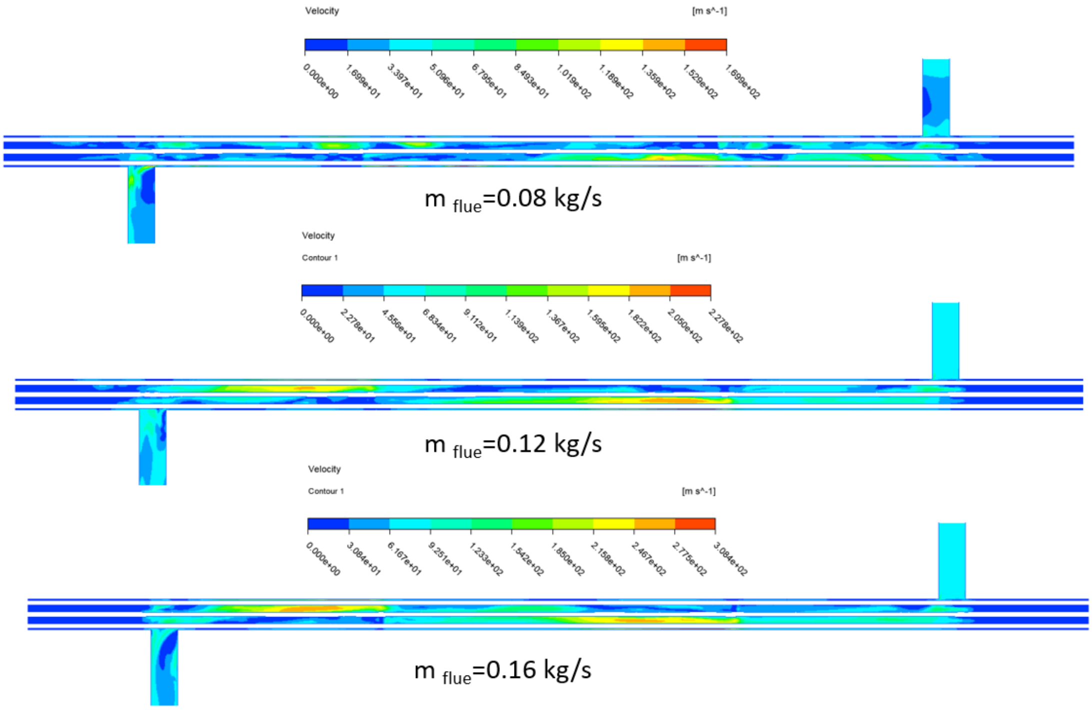

**Figure 6. 11 Velocity of flue gas at the mid-plane of STHX at different airflow mass flow rate ($T_{flue\ gas}$=1073.15 K, $m_{CO2}$=0.1272 kg/s, $P_{CO2}$=12 MPa).**

### 6.4.4 $CO_2$ outlet temperature at different conditions

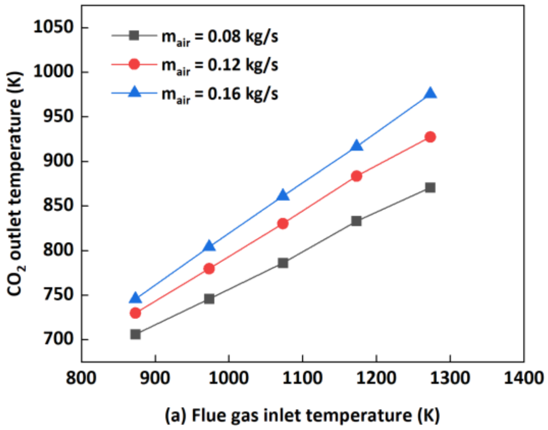

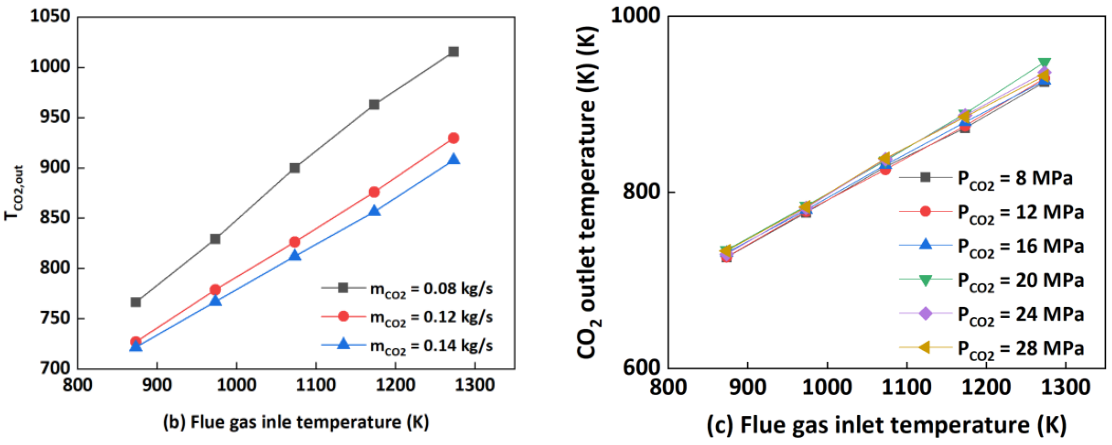

**Figure 6. 12** $CO_2$ outlet temperature with (a) different flue gas mass flow rate (b)different $CO_2$ mass flow rate (c) different turbine inlet pressure.

The variations of $CO_2$ outlet temperature with different air mass flow rate, $CO_2$ mass flow rate and turbine inlet pressure are shown in Figure 6.12. When the airside mass flow rate is the only variable, $CO_2$ outlet temperature can be effectively increased by higher air mass flow rate. Consequently, the system thermal efficiency can be enhanced. Similar trends can be found in Figure 6.12 (b) and Figure 6.12 (c). At constant values of air inlet temperature, $CO_2$ inlet temperature and $CO_2$ mass flow rate, $CO_2$ outlet temperature at any position on curves is higher for higher shell side fluid mass flow rate. It also can be observed that higher air mass flow rate has stepper curves, which means air mass flow rate has pronounced impact on $CO_2$ outlet temperature when air temperature is higher.

The effects of $CO_2$ gas heater designs and operations on the performance of its associated system are also investigated. To facilitate such an investigation, based on the CFD modeling simulation results, the $CO_2$ outlet temperature with the functions of $CO_2$ inlet temperature , flue gas mass flow rate, $CO_2$ pressure at turbine inlet and flue gas temperature were correlated as polynomial expressions and are listed in Eq. 6.21, Eq. 6.22 and Eq. 6.23. Due to different operating conditions lead to different $CO_2$ outlet temperature. Eq.6.21 is the function to calculate CO₂ outlet temperature with different flue gas mass flow rate. The corresponding correlative coefficients of $c_1 \sim c_6$ of Eq.6.21 are listed in Table 6.2, Eq.6.22 can be used to calculate CO₂ outlet temperature at different turbine inlet pressure (CO₂ pressure in gas heater). The corresponding correlative coefficients of $c_1 \sim c_6$ of Eq.6.22 are listed in Table 6.3. Eq.6.23 is the formular to calculate CO₂ outlet temperature when flue gas temperature is a variable. The correlative coefficients of $c_1 \sim c_6$ of Eq.6.23 are listed Table 6.4.

$$T_{CO2,out} = c_1 * T_{co2,in}^2 + c_2 * T_{co2,in} + c_3 * T_{co2,in} * \dot{m}_{flue} + c_4 * \dot{m}_{flue} + c_5 * \dot{m}_{flue}^2 + c_6 \tag{6.21}$$

$$T_{CO2,out} = c_1 * T_{co2,in}^2 + c_2 * T_{co2,in} + c_3 * T_{co2,in} * P_{CO2} + c_4 * P_{CO2} + c_5 * P_{CO2}^2 + c_6 \tag{6.22}$$

$$T_{CO2,out} = c_1 * T_{co2,in}^2 + c_2 * T_{co2} + c_3 * T_{co2} * T_{air} + c_4 * T_{air} + c_5 * T_{air}^2 + c_6 \tag{6.23}$$

**Table 6. 2 Coefficients of $c_1 \sim c_6$ in Eq. 6.21.**

| $\dot{m}_{flue}$ (kg/s) | $c_1$ | $c_2$ | $c_3$ | $c_4$ | $c_5$ | $c_6$ |
|---|---|---|---|---|---|---|
| 0.08 | 1.08E-05 | 0.3082086 | 0.000782 | 0.000280851 | 0.005645 | 0.434771 |
| 0.1 | 1.08E-05 | 0.2572843 | 0.000672 | 0.000280843 | 0.003945 | 0.434724 |
| 0.12 | 1.05E-05 | 0.2092301 | 0.00057 | 0.000280859 | 0.002981 | 0.434587 |
| 0.14 | 1.07E-05 | 0.2041829 | 0.000465 | 0.00028084 | 0.002293 | 0.434733 |
| 0.16 | 1.06E-05 | 0.1922788 | 0.00038 | 0.00028084 | 0.001845 | 0.434744 |
| 0.18 | 1.06E-05 | 0.193391 | 0.00034 | 0.000280841 | 0.001476 | 0.434754 |
| 0.2 | 1.08E-05 | 0.2700277 | 0.000667 | 0.00028084 | 0.000798 | 0.434758 |

Table 6. 3 Coefficients of $c_1 \sim c_6$ in Eq. 6.22.

| $P_{co2}$ (MPa) | $c_1$ | $c_2$ | $c_3$ | $c_4$ | $c_5$ | $c_6$ |
|---|---|---|---|---|---|---|
| 8 | 0.00034418 | 0.01435 | 3.51E-05 | 0.036705 | 0.000435 | 0 |
| 12 | 0.00034594 | 0.024892 | 3.51E-05 | 0.036361 | 0.000431 | 0 |
| 16 | 0.00034594 | 0.024892 | 3.51E-05 | 0.036361 | 0.000431 | 0 |
| 20 | 0 | 0.117314 | 0.000286 | 0.03598 | 0.000358 | 0 |
| 24 | 0.00013974 | 0.067759 | 0.000151 | 0.036271 | 0.000414 | 1.81E-08 |
| 28 | 8.4241E-08 | 0.091059 | 0.000289 | 0.035994 | 0.00037 | 1.81E-08 |

Table 6. 4 Coefficients of $c_1 \sim c_6$ in Eq. 6.23.

| $T_{flue}$ (K) | $c_1$ | $c_2$ | $c_3$ | $c_4$ | $c_5$ | $c_6$ |
|---|---|---|---|---|---|---|
| 873.15 | 1.04E-05 | 0.17316 | 0.0003 | 0.000281 | 0.00059 | 0.434486 |
| 1073.15 | 1.39E-06 | 0.62705 | 2E-05 | 0.359649 | 3.92E-05 | 0.999402 |
| 1273.15 | 5.23E-06 | 0.364155 | 2E-05 | 0.496062 | 4.01E-05 | 0.99914 |

## 6.5 Model applications

### 6.5.1 Structural design optimization

According to the simulation results of the $CO_2$ gas heater in section 6.4.3 shown in Figure 6.10, there are two stagnate regions for the shell-side flue gas in which one is between the $CO_2$ fluid inlet and flue gas outlet ports, and another is between the flue gas inlet and $CO_2$ fluid outlet ports. To enhance the heat transfer in these two regions, relocating the flue gas inlet and outlet port positions could be an effective approach, as shown in Figure 6.13. To differentiate the two types of shell-and-tube heat exchangers, the original $CO_2$ gas heater is referred as STHXA in this section, while the optimized gas heater is named as STHXB.

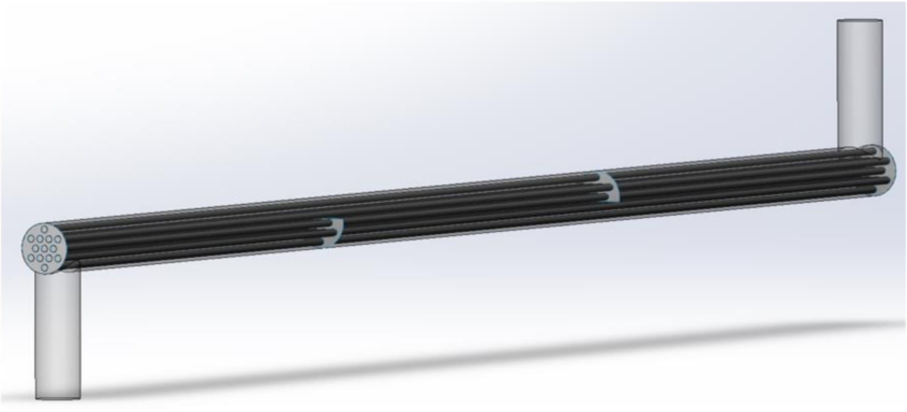

Figure 6. 13 Geometry for the relocated pipe ports of $CO_2$ gas heater (STHXB).

### 6.5.2 Temperature and streamline distributions

In order to study the effects of alternative geometry designs, STHXB is also modelled and simulated with CFD. Figure 6.14 shows the comparisons of temperature contours at flue gas central lanes for both STHXA and STHXB. It can be easily seen that by repositioning the flue gas inlet and outlet ports, the reduced temperatures of flue gas at both ends of shell side from STHXA are eliminated effectively. Therefore, sufficient heat exchange area can be achieved in the optimized heat exchanger of STHXB. Figure 6.15. also proves this point that the flue gas temperature profile of STHXB is slightly lower than that of STHXA in the middle region but is much higher at the regions close to two ends. Meanwhile the $CO_2$ temperature profile on the tube side is higher for the STHXB indicating the increased heating capacity. Correspondingly, the LMTD of STHXB is calculated as 203 K compared to 225.9 K of STHXA. The lower temperature difference leads to better heating capacity and less irreversibility of heat transfer process.

By comparing Figure 6.10 and Figure 6.16, it is clear that STHXB has vaster turbulent flow than that of STHXA due to the higher velocity of flue gas, and hence higher Reynolds number when inlet and outlet ports are relocated. Additionally, it is noticed that the regions behind baffles are not used effectively for the heat transfer, as the baffles tend to alternate the direction of flue gas flow. However, by increasing the number of baffles or decreasing the baffle spacing, the recirculation zones could be successfully minimized.

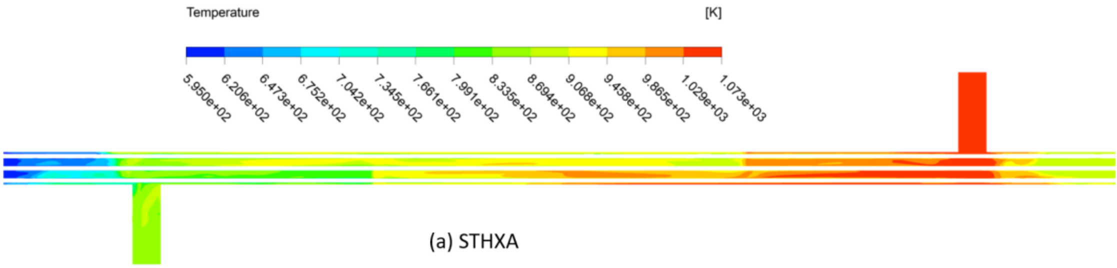

(a) STHXA

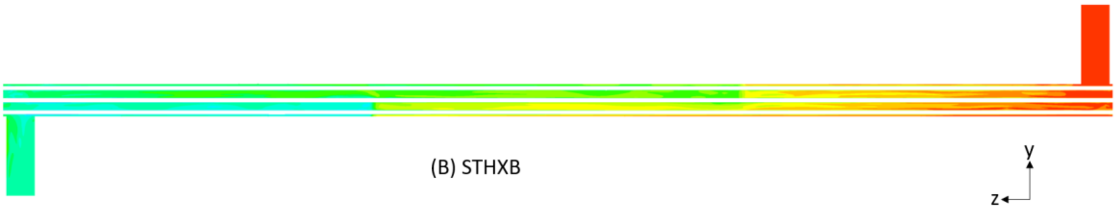

(B) STHXB

**Figure 6. 14 Temperature contours at central x-axial plane of: (a) STHXA; (B) STHXB. (Operating conditions: $T_{\text{flue gas}}$ = 1073.15 K, $m_{\text{flue gas}}$ = 0.12 kg/s ,$m_{CO2}$ = 0.1272 kg/s, $P_{CO2}$ = 12 MPa)**

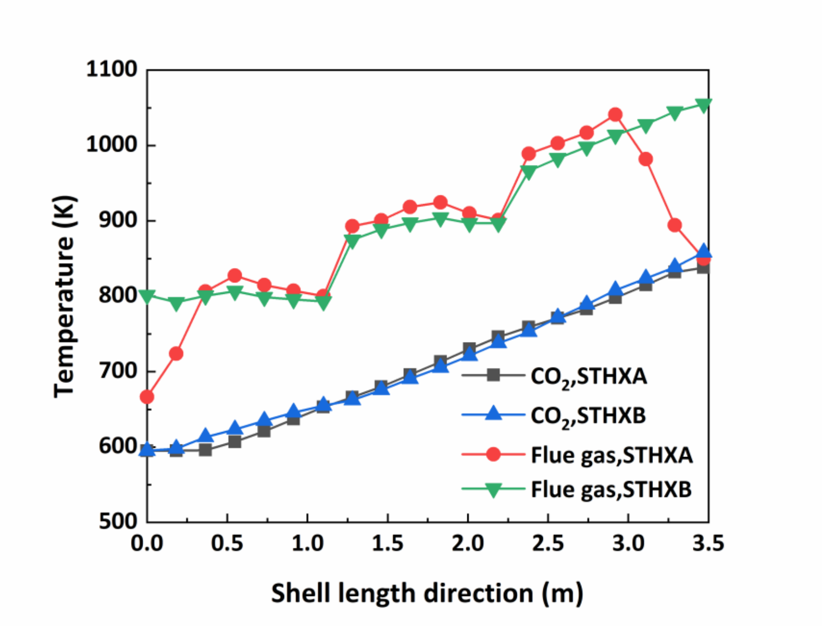

**Figure 6. 15 Comparison of $CO_2$ and flue gas temperature profiles for STHXA and STHXB. (Operating conditions: $T_{\text{flue gas}}$ = 1073.15 K, $m_{\text{flue gas}}$ = 0.12 kg/s, $m_{CO2}$ = 0.1272 kg/s, $P_{CO2}$ = 12 MPa)**

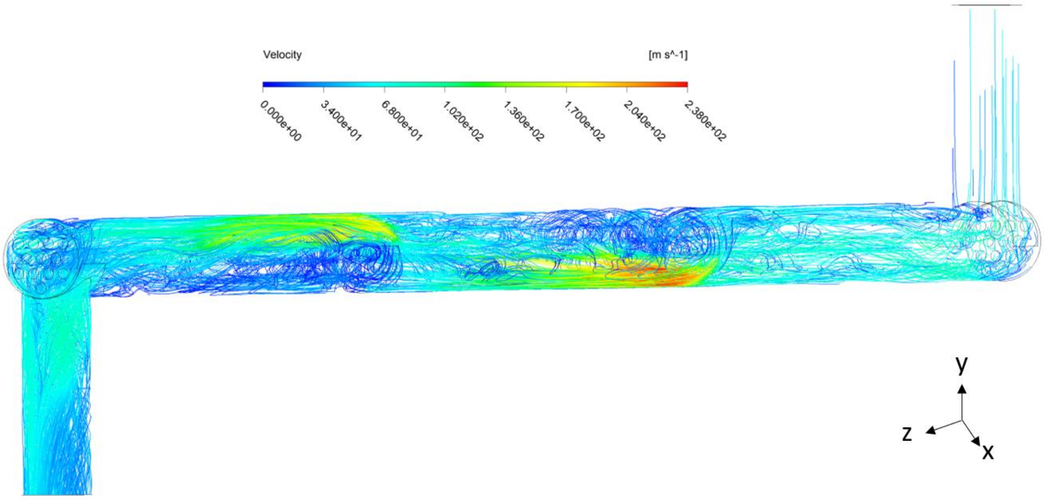

**Figure 6. 16 velocity streamlines of shell side flue gas of STHXB. (Operating conditions: $T_{flue\ gas}$ = 1073.15 K, $m_{flue\ gas}$ = 0.12 kg/s, $m_{CO2}$ = 0.1272 kg/s, $P_{CO2}$ = 12 MPa)**

### 6.5.3 Performance improvement for the heater

Thermal hydraulic performances were evaluated and compared for both STHXA and STHXB by the developed models. For each model simulation, there is only one variable, and all other parameters are kept at their deigned values as listed in Table 6.1. As shown in Figure 6.17(a), the shell side heat transfer coefficient and pressure drop both increase with higher flue gas mass flow rate. In quantity, for the heat transfer coefficients, the values for STHXB are averagely 15.6% higher than those for STHXA at a range of flue gas mass flow rates, while the maximum increment of 25% occurs at 0.12 kg/s of flue gas mass flow rate. For the pressure drop, the STHXB is averagely 14% higher than that for STHXA while both heat exchangers show more pressure drop increase with further increased flue gas flow rate.

The effectiveness of the shell-and-tube heat exchanger can be calculated as the ratio of actual heating capacity to the maximum heating capacity at a fixed operating condition as described in Eq. 6.24:

$$\varepsilon = \frac{Q_{actual}}{Q_{max}} = \frac{Q_{actual}}{(mc_p)_{\min}(T_{flue,in} - T_{CO2,in})} \qquad 6.24$$

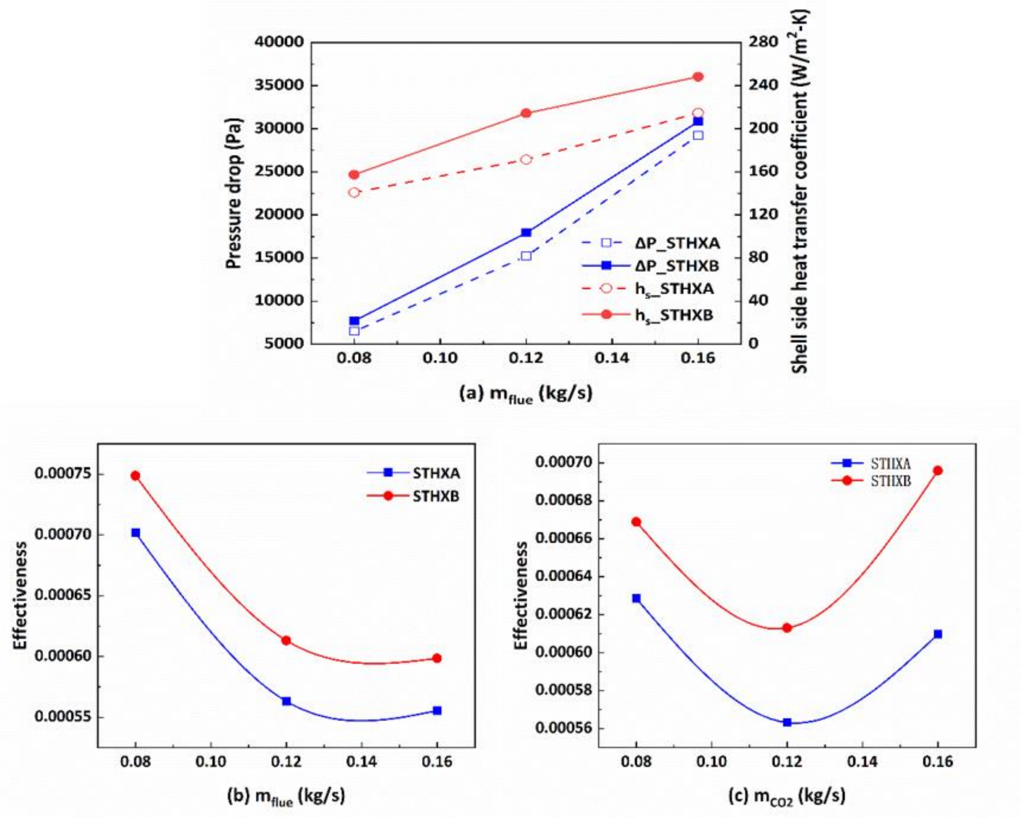

Figure 6. 17 Comparisons of heat transfer coefficient, pressure drop and effectiveness of STHXA and STHXB.

As illustrated in Figure 6.17 (b), with the increase of flue gas mass flow rate, the effectiveness of either STHXA or STHXB decreases but the decrease rate is slowed down when the flue gas is higher than 0.12 kg/s. However, the effectiveness of STHXB is always higher than that of STHXA and the average increment is 7.8% when STHXB is applied. Figure 6.17(c) demonstrates the variations of effectiveness with increased mass flow rate of $CO_2$. When the $CO_2$ mass flow rate increases from 0.08 kg/s to 0.12 kg/s, the effectiveness for either STHXA or STHXB decreases. With further increasing $CO_2$ mass flow rate to 0.16 kg/s, the effectiveness for each heat exchanger increases. This is because the thermal capacitance of $CO_2$ side increases until it overlaps the value of shell side. The average effectiveness of STHXB is averagely 9.8% higher than that of STHXA, as shown in Figure 6.15(c).

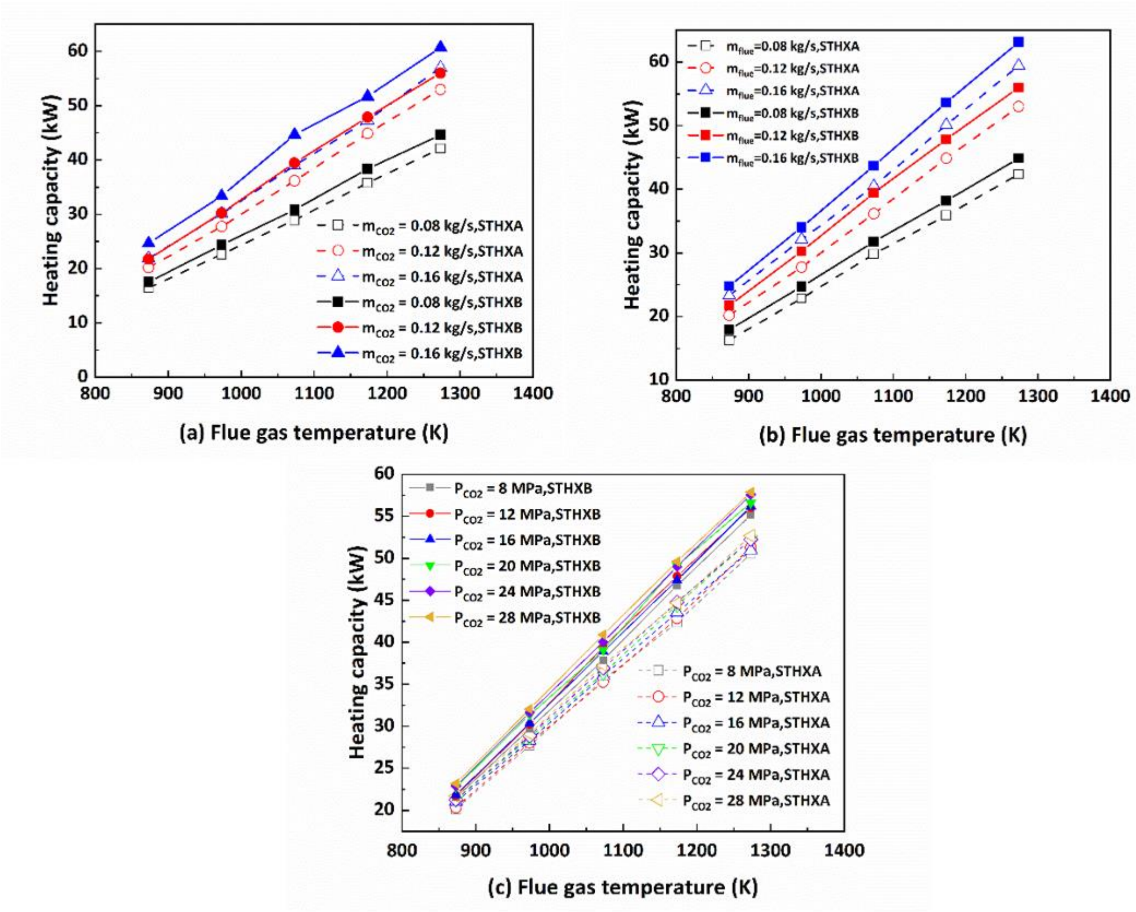

Figure 6. 18 Comparisons of heating capacity for STHXA and STHXB.

As shown in Figure 6.18, the heating capacities of STHXA and STHXB are compared under various operating parameters. It is shown that the heating capacity for both heat exchangers increases with higher $CO_2$ mass flow rate, more flue gas mass flow rate, and increased flue gas temperature . At a constant operating parameter, the heating capacity of STHXB is always greater than that of STHXA. The average percentage increase in heating capacity of STHXB is 7.2% with respect to STHXA when flue gas temperature and flow rate are varied, as illustrated in Figure 6.18 (a). Similarly, the heating capacity can be improved by 9.2% for STHXB compared to STHXA when flue gas temperature and

$CO_2$ mass flow rate are changed, as depicted in Figure 6.18(b). It can be seen in Figure 6.18(c), the heating capacity can be enhanced averagely by 5.9% for STHXB compared to STHXA when flue gas temperature and $CO_2$ pressure are changed. However, for each heat exchanger, the effect of $CO_2$ pressure on the heating capacity is relatively insignificant compared to the effects of other operating parameters. Therefore, it can conclude that the STHXB performs better than STHXA in terms of heat transfer coefficient, effectiveness and heating capacity at a fixed operating condition.

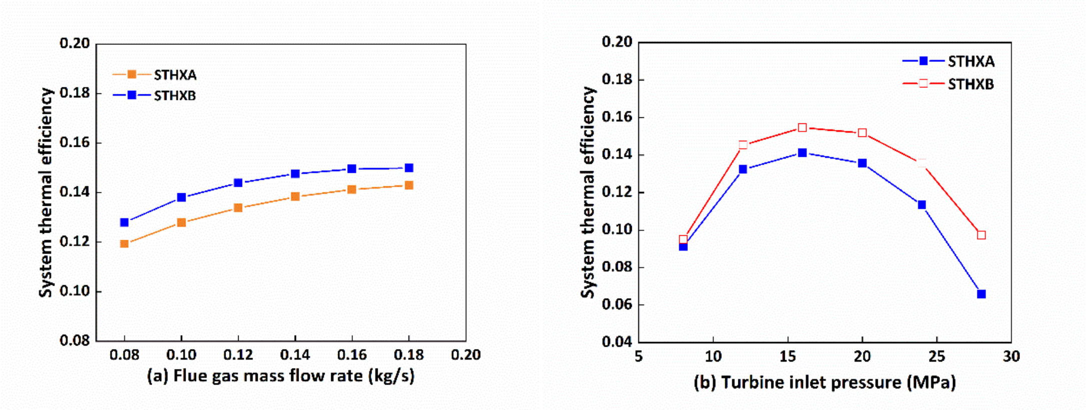

(a) Flue gas mass flow rate (kg/s)

(b) Turbine inlet pressure (MPa)

Figure 6. 19 Comparisons of thermal efficiency for STHXA and STHXB.

As depicted in Figure 6.19(a), the higher flue gas flow rate will increase the system thermal efficiency for the integrated STHXA or STHXB due to the increased gas heater heat capacity. However, similar to its effect on heat capacity, the increase extent of the thermal efficiency is reduced when the flue gas flow rate is further increased. Although the $CO_2$ pressure doesn’t affect much to the gas heater heat capacity, there is an optimal $CO_2$ pressure to maximize the system thermal efficiency. This is due to the opposite effects of the $CO_2$ pressure at the turbine inlet on the turbine power generation and compressor power consumption when the $CO_2$ pressure at the turbine outlet is fixed. The detailed calculations can be seen in the next chapter. The simulation results can instruct well to the controls of gas heater and its associated system. Again, the performance of associated system can also be better when the STHXB is integrated. When the flue gas mass flow rate is the only variable, the average thermal efficiency can be approximately 6% higher for the system with the STHXB.

## 6.6 Summary

Detailed 3D CFD model for a shell-and-tube supercritical $CO_2$ gas heater utilized in a biomass-$CO_2$ power generation system has been developed and validated. Realizable k-ε model was adopted for model simulations. The validated model was then applied to predict the thermal-hydraulic performance of the heat exchanger and its associated system at different operating conditions and structural designs. It is observed from the simulation results that the locations of flue gas inlet and outlet ports can significantly affect the heat transfer of the heat exchanger. New designed of this shell-and-tube gas heater (STHXB) was carried out and compared with the original one (STHXA), results showing that the performance of $CO_2$ gas heater can be effectively improved by replacing from STHXA to STHXB.

**Chapter 7** will present thermodynamic analysis of biomass-$CO_2$ Transcritical Brayton Cycles by integrating the results of CFD simulations of $CO_2$ gas heater. System performance will be evaluated at different heat source temperature, heat source mass flow rate, turbine inlet and outlet pressure, and heat sink temperature.

# Chapter 7- Thermodynamic Analysis of Biomass-$CO_2$ Transcritical Brayton Cycles Combined with CFD Simulations.

## 7.1 Introduction

The performance of the shell-and-tube heat exchanger at varied operating conditions and structural designs can indirectly influence the thermal efficiency of its associated biomass-$CO_2$ power generation system. Accurate results of $CO_2$ outlet temperature of shell-and-tube heat exchanger can be achieved by using CFD modelling method. To fully understand the operations and controls of the tested system, a thermodynamic model for biomass-$CO_2$ Brayton cycle has been developed by the Engineering Equation Solver (EES) software integrated with results of CFD $CO_2$ gas heater model. EES is a general equation-solving program that can solve different equations numerically. One of the biggest advantages of EES is that the high accuracy thermodynamic and transport property database for different substances can be directly used in solving equations. Besides, EES recognizes equations automatically and meanwhile group equations, making the simulation procedure simplified and keeping the solution high efficiency. A theoretical study based on energy and exergy analysis of system will be presented to investigate the effects of turbine inlet pressure, turbine outlet pressure, heat source mass flow rate, heat source temperature and heat sink temperature. Figure 7.1(a) shows the simplified layout of the biomass-$CO_2$ transcritical Brayton cycle. $CO_2$ is heated up to highest cycle temperature at point ‘1’ after the gas heater, the $CO_2$ is expanded in the turbine to generate electricity point ‘1’ to ‘3’. Then the $CO_2$ releases heat through recuperator to point ‘4’ and be furthered cooled down by gas cooler-2 to point ‘5’. In addition to reduce $CO_2$ temperature, recuperator can also preheat the compressed $CO_2$ before it re-enters into gas heater, as shown from point ‘6’ to ‘7’. The last step is to adiabatically compress $CO_2$ through the compressor, from point ‘5’ to ‘6’. The point numbers in T-S diagram (Figure 7.1 (b)) are same as the numbers in Figure 7.1 (a) The cycle then repeats.

### 7.1.1 Assumptions

- The system operates under steady state.
- The kinetic and potential energies are neglected for the $CO_2$ flowing through the system components.
- These is no pressure drop for the $CO_2$ flowing through the recuperator or the second gas cooler.
- Mass flow rate of cooling water is 0.15 kg/s.
- Temperature difference between compressor inlet and cooling water is 10 K.
- Isentropic efficiency of turbine and effectiveness of recuperator are both assumed as 0.7.
- Compressor isentropic efficiency and volumetric efficiency are calculated based on performance data from manufacturer [124], as seen in Eq 7.9 and Eq 7.10.
- The dead state of pressure is assumed as atmospheric pressure of 1.013 bar and ambient temperature is assumed to be the temperature of heat sink $T_c$.

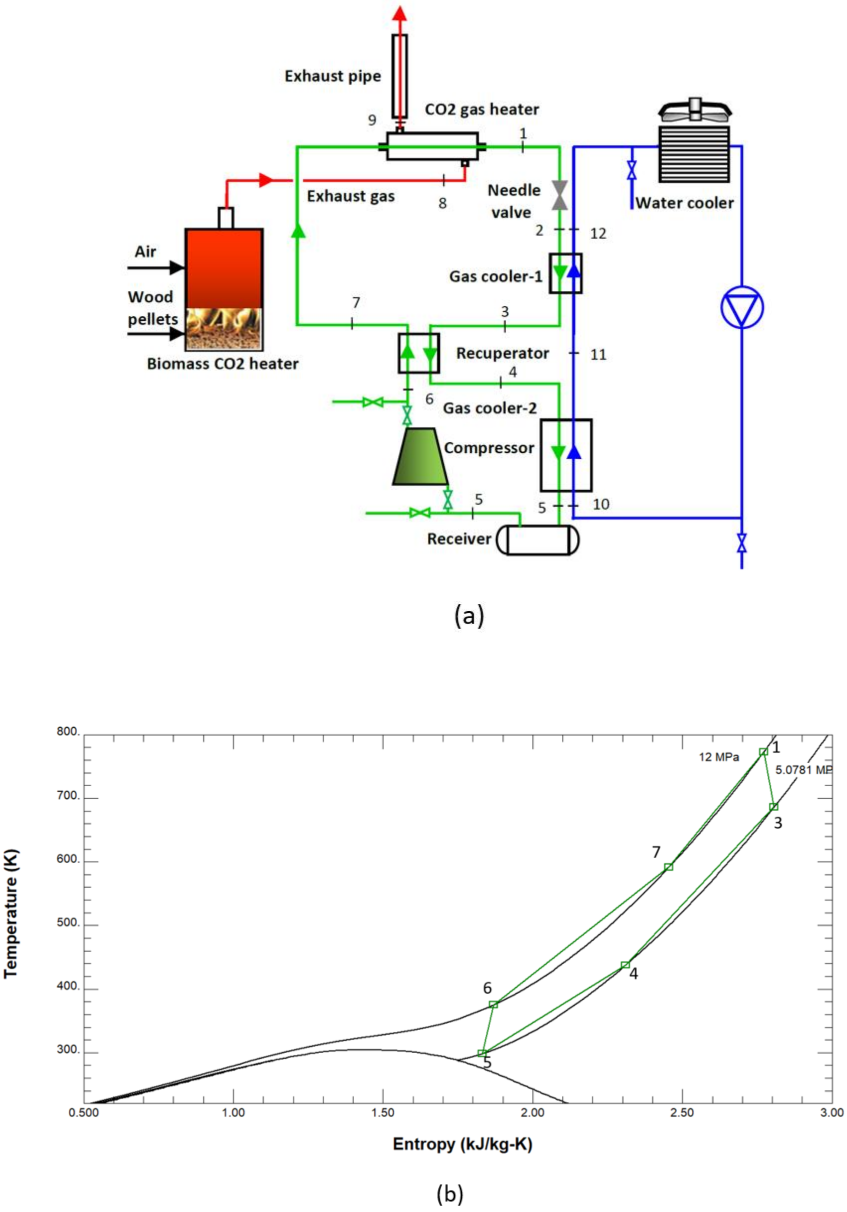

Figure 7. 1 (a) System layout, (b) T-S diagram of the simulated biomass-$CO_2$ transcritical Brayton cycle.

### 7.2.2 Operating conditions for simulations

Detailed simulation conditions are listed in Table 7.1. Biomass flue gas inlet temperature varies from 600 ˚C to 1000 ˚C, and its mass flow rate changes from 0.08 kg/s to 0.2 kg/s. For the water temperature (heat sink) of gas cooler -2 changes between 15 ˚C and 19 ˚C, and its mass flow rate 0.15 kg/s. For each simulation, there is only one variable and others will keep constant.

Table 7. 1 Operating conditions for thermodynamic simulations.

| Biomass flue gas | | Cooling water | | Turbine inlet | Turbine outlet |
|---|---|---|---|---|---|
| $T_{flue}$ | $m_{flue}$ (kg/s) | $T_{water}$ (K) | $m_{water}$ (kg/s) | $P_{in}$ (Mpa) | $P_{out}$ (Mpa) |
| 873.15-1273.15 (1073.15 when constant) | 0.08-0.2 (0.12 when constant) | 288.15-292.15 (288.15 when constant) | 0.15 | 8-28 (12 when constant) | 1.432-5.0871 (5.0871 when constant) |

## 7.2 Energy calculations

- Heat capacity of $CO_2$ gas heater:

$$Q_{gh} = \dot{m}_{CO2}(h_1 - h_7) \tag{7.1}$$

- Turbine power generation:

$$W_t = \dot{m}_{CO2}(h_1 - h_3) \tag{7.2}$$

The isentropic efficiency of turbine is defined in following way:

$$\eta_t = \frac{h_1 - h_3}{h_1 - h_{3,s}} \tag{7.3}$$

- Recuperator:

As the definition of effectiveness is the ratio of the actual amount of heat transferred to the maximum amount of heat, it can be calculated by:

$$\varepsilon_{rec} = \frac{h_3 - h_4}{Q_{rec,max}} = \frac{h_7 - h_6}{Q_{max}} \tag{7.4}$$

$$Q_{rec,max} = min\begin{Bmatrix} \dot{m}_{CO2}(h_3 - h_4), assuming\ T_4 = T_6 \\ \dot{m}_{CO2}(h_7 - h_6), assuming\ T_7 = T_3 \end{Bmatrix} \tag{7.5}$$

- Heat capacity of $CO_2$ gas cooler:

$$Q_{gc} = \dot{m}_{CO2}(h_4 - h_5) \tag{7.6}$$

- Compressor power consumption:

$$W_{comp} = \dot{m}_{CO2}(h_6 - h_5) \qquad 7.7$$

- The isentropic efficiency of compressor is defined in following way:

$$\eta_{comp} = \frac{h_{6,s} - h_5}{h_6 - h_5} \qquad 7.8$$

- The isentropic efficiency of compressor can be expressed as:

$$\eta_{isentropic} = -0.0141{r_p}^2 + 0.0793r_p + 0.5603 \qquad 7.9$$

- The volumetric efficiency of compressor can be obtained by:

$$\eta_{isentropic} = -0.059r_p + 0.9458 \qquad 7.10$$

- The cycle net efficiency for this closed Brayton cycle is defined as useful energy output divided by total energy input as shown in following equation:

$$\eta_{th} = \frac{W_{net}}{Q_{in}} = \frac{W_t - W_{comp}}{Q_{gh}} \qquad 7.11$$

## 7.3 Exergy calculations

The second law of thermodynamics is capable of indicating the maximum possible efficiency of system. Due to entropy generation, various thermodynamic losses occur in power generation system. Exergy analysis is used to describe these losses which is based on the second law of thermodynamics. Therefore, it is important to calculate exergy loss or irreversibility of each component and further improve the system by operations and controls. The exergy at each state can be calculate as:

$$\dot{E}_\iota = \dot{m}_i[(h_i - h_0) - T_0(S_i - S_0)] \qquad 7.12$$

- Gas heater

$$\dot{E}_{in} = \dot{m}_{CO2}(h_1 - h_7)(1 - \frac{T_c}{T_r}) \tag{7.13}$$

$$\dot{E}_{l,gh} = E_{in} - \dot{m}_{CO2}[(h_1 - h_7) - T_0(S_1 - S_7)] \tag{7.14}$$

- Turbine

$$\dot{E}_{l,t} = \dot{m}_{CO2}[(h_1 - h_3) - T_0(S_1 - S_3)] - W_t \tag{7.15}$$

- Recuperator

$$\dot{E}_{l,rec} = \dot{m}_{CO2}[(h_3 - h_4) - T_0(S_3 - S_4) + (h_6 - h_7) - T_0(S_6 - S_7)] \tag{7.16}$$

- Gas cooler

$$\dot{E}_{l,gc} = \dot{m}_{CO2}[(h_4 - h_5) - T_0(S_4 - S_5)] \tag{7.17}$$

- Compressor

$$\dot{E}_{l,comp} = W_{comp} - \dot{m}_{CO2}[(h_6 - h_5) - T_0(S_6 - S_5)] \tag{7.18}$$

The second law efficiency of cycle can be obtained by:

$$\eta_{ex} = \frac{W_{net}}{E_{in}} = \frac{W_t - W_{comp}}{E_{in}} \tag{7.19}$$

## 7.4 Performance Analysis

### 7.4.1 Effects of biomass flue gas temperature at different turbine inlet pressure

This study aims to investigate effects of different parameters. These include turbine inlet pressure, turbine outlet pressure, heat source temperature, heat source mass flow rate and heat sink temperature. Figure 7.2 shows the variations of gas heater capacity, compressor power consumption, turbine power generation and $CO_2$ mass flow rate with different flue gas temperature and $CO_2$ turbine inlet pressure. From Figure 7.2 (a) it is known that the $CO_2$ mass flow rate drcreases with the increase of turbine inlet pressure.

This is because with the increase of pressure ratio, the volumeric efficiency decreased, and pumping ability of compressor is reduced. $CO_2$ gas heater capacity has a slightly drcrease trend with higher turbine inlet pressure due to the decrease of $CO_2$ mass flow rate. Higher heat source temperature higher heat capacity of gas heater. With the pressure ratio increasing, turbine power generation is also increased. The increment will be decreased with turbine inlet pressure is furthure increased as seen in Figure 7.2 (c). Turbine power generation also can be increased by increasing the turbine inlet temperature by enhance the temperature of heat source. However the increase of pressure ratio leads to higher power consumption of compressure due to large pressure different betweeen compressor inlet and outlet, as depicted in Figure 7.2 (d). Heat source temperarure can not influence the compressor power.

The exergy loss and efficiencies of system with different turbine inlet pressure and heat source temperature are shown in Figure 7.3. As seen in Figure 7.3 (a), with the increase of turbin power generation, exergy loss of turbine is also increased. Similar trend also can be observed for gas cooler exergy loss. Exergy loss of gas cooler is the highest in system at higher turbine inlet pressure. This is because more heat need to be released to ambient with higher pressure ratio at constant compressor inlet temperature. In contrast, the exergy loss of recuperator can be reduced by increasing turbine inlet pressure due to the differece of specific heat of turbine out and compressor out are minimized.

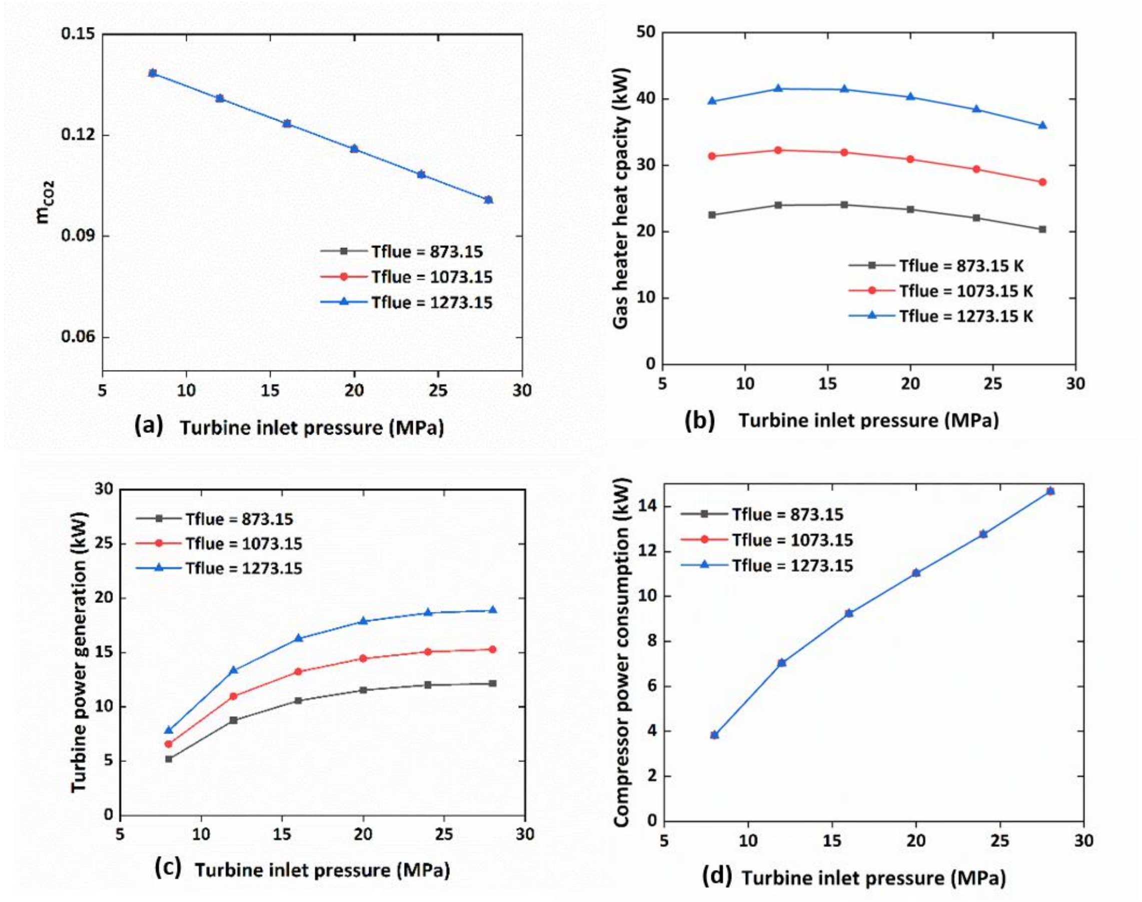

Figure 7. 2 Variation of (a) $CO_2$ mass flow rate (b) $CO_2$ gas heater capacity (c) turbine power (d) compressor power with different heat source temperature and turbine inlet pressure.

Thermal efficiency is the ratio of net work and energy input. Net work is the difference between turbine power generation and compressor power consumption. Although higher pressure ratio contributes to higher turbine power, the higher power can be consumed by compressor. Therefore, the thermal efficiency initially increases with the increase in $CO_2$ inlet pressure ratio and then decreases with the future increase as shown in Figure 7.3 (b). Higher heat source temperature makes higher thermal efficiency of system. There is optimal value of pressure ratio which can maximize the thermal efficiency. The higher heat source temperature, the higher value of optimal pressure ratio. Exergy efficiency also increases first and then decreases with higher turbine inlet pressure as seen in Figure 7.3 (c). It can be noticed that both thermal efficiency and exergy efficiency can be dropped below zero, this is because if the turbine inlet pressure is too high, turbine power generation will be overwhelmed by the power consumption of compressor.

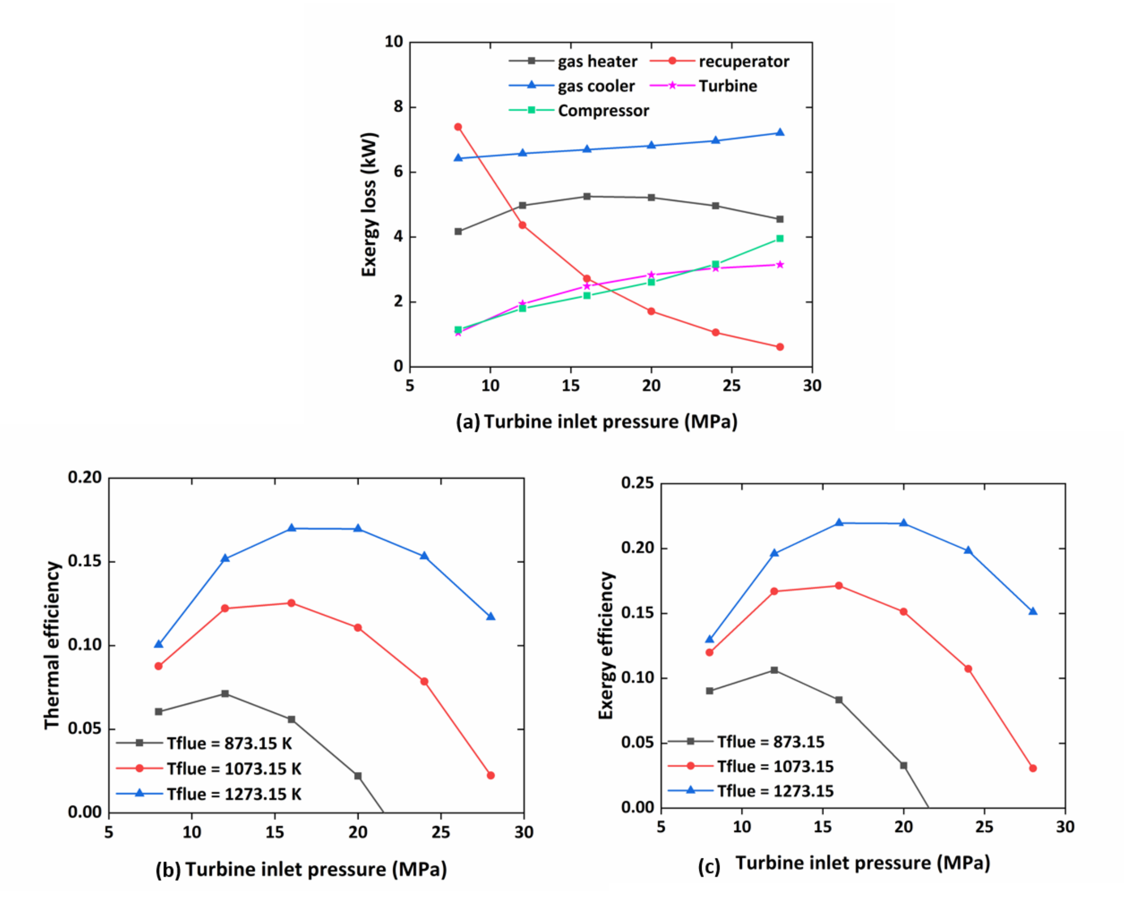

**Figure 7. 3** Variation of (a) energy loss (b) thermal efficiency (c) exergy efficiency with different heat source temperature and turbine inlet pressure.

### 7.4.2 Effects of biomass flue gas mass flow rate at different turbine inlet pressure

As indicated in Figure 7.4 (a), the higher flue gas mass flow rate can significantly increase the heat capacity of gas heater due to the heat transfer is improved. The increment could be decreased when the flue gas mass flow rate is high. As to the turbine power generation as shown in Figure 7.4 (b), higher heat source mass flow rate contributes to higher turbine power output, which is more obvious when $CO_2$ turbine inlet pressure is high. However, the flue gas mass flow rate does not influence the compressor power consumption. Therefore, the thermal efficiency and exergy efficiency can be increased with the increase of flue gas mass flow rate as shown in Figure 7.4 (c) and Figure 7.4 (d).

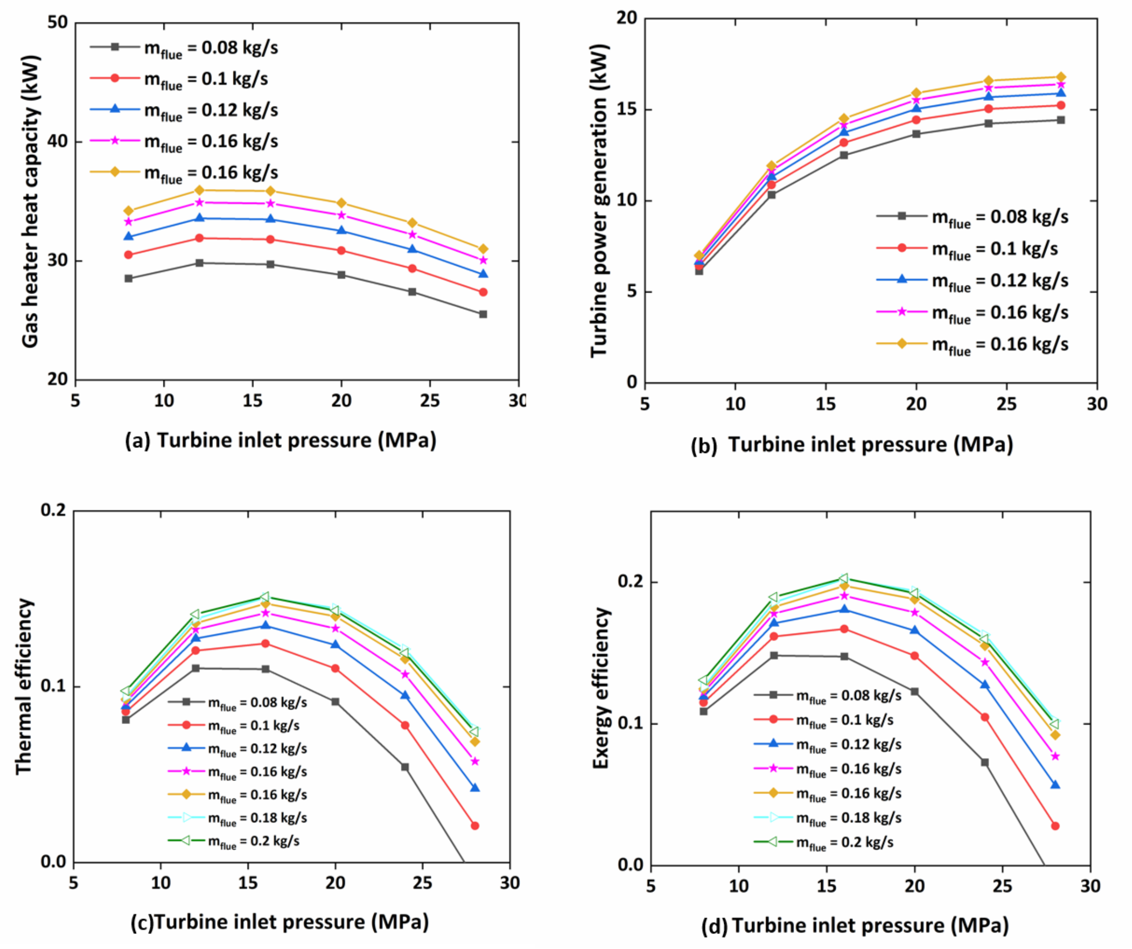
(a) Turbine inlet pressure (MPa)
(b) Turbine inlet pressure (MPa)
(c)Turbine inlet pressure (MPa)
(d) Turbine inlet pressure (MPa)

Figure 7. 4 Variation of (a) $CO_2$ gas heater capacity (b) turbine power (c) thermal efficiency (d) exergy efficiency with different mass flow rate of heat source and turbine inlet pressure.

### 7.4.3 Effects of cooling water mass flow rate at different turbine inlet pressure

Figure 7.5 demonstrates the effects of heat sink temperature on gas heater capacity, $CO_2$ mass flow rate, thermal efficiency and exergy efficiency. It can be seen in Figure 7.5 (a), higher heat sink temperature leads to lower $CO_2$ mass flow rate which is influenced by the decreased density of $CO_2$. The higher heat sink temperature, the lower gas heater capacity due to the lower mass flow rate of $CO_2$. Therefore, lower temperature at turbine inlet can be caused, and lower turbine power output. Heat sink temperature does not affect the power consumption of compressor. Consequently, the thermal efficiency and exergy efficiency are also decreased with the increase of heat sink temperature.

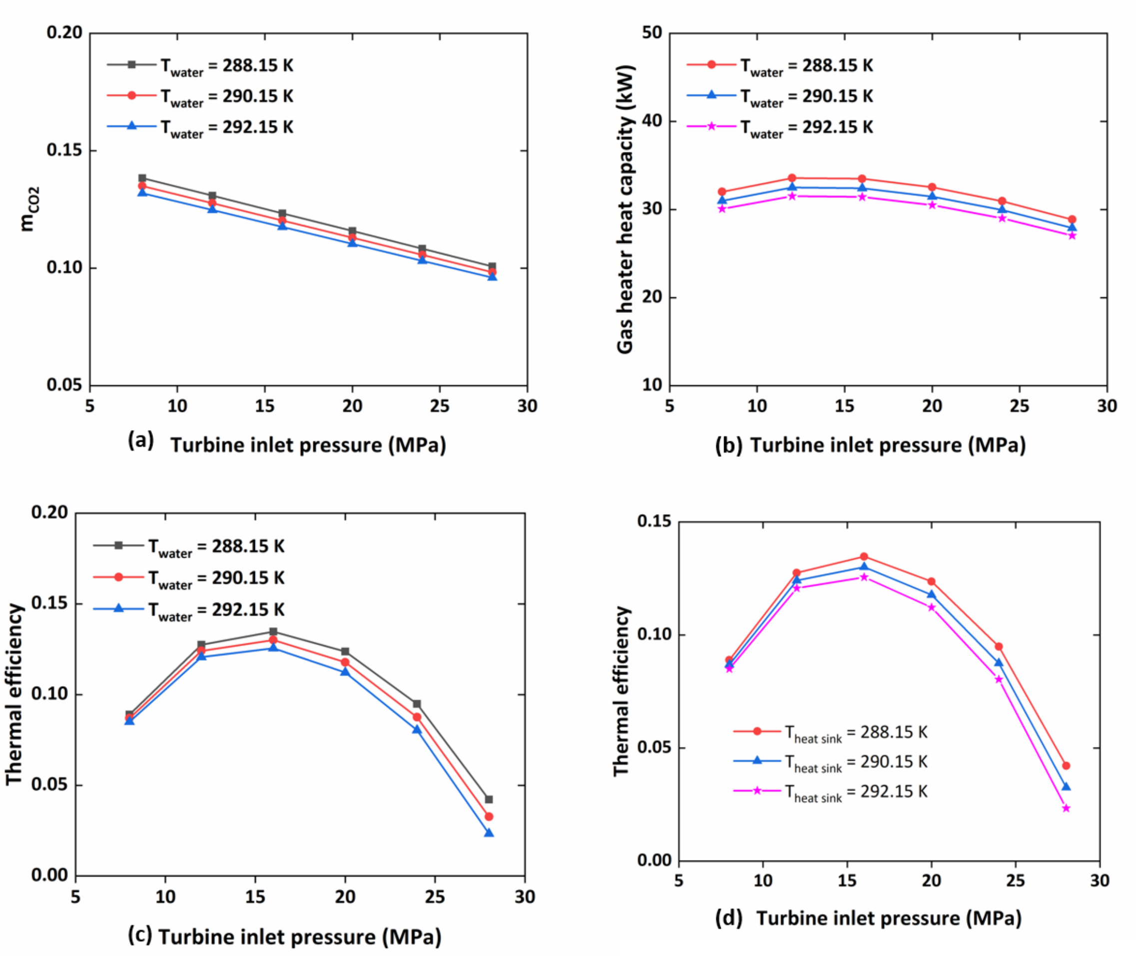

Figure 7. 5 Variation of (a) $CO_2$ gas heater capacity (b) $CO_2$ mass flow rate (c) thermal efficiency (d) exergy efficiency with different mass flow rate of heat source and turbine inlet pressure.

### 7.4.4 Effects of heat source temperature at different turbine outlet pressure.

As seen in Figure 7.6 (a), $CO_2$ mass flow rate increases with higher turbine outlet pressure due to the volumetric efficiency is increased. $CO_2$ gas heater capacity is increased with turbine pressure outlet as the $CO_2$ mass flow rate increases, as shown in Figure 7.6 (b). As for the turbine power generation, turbine outlet pressure can greatly increase the power generation when the outlet pressure is relatively lower as seen in Figure 7.6 (c). With the increase of turbine outlet pressure, the power consumption of compressor initially decreases, and then increases with further increase turbine outlet pressure. The decreasing is because of the compressor ratio reduction, and the increasing is because of the increase in $CO_2$ mass flow rate.

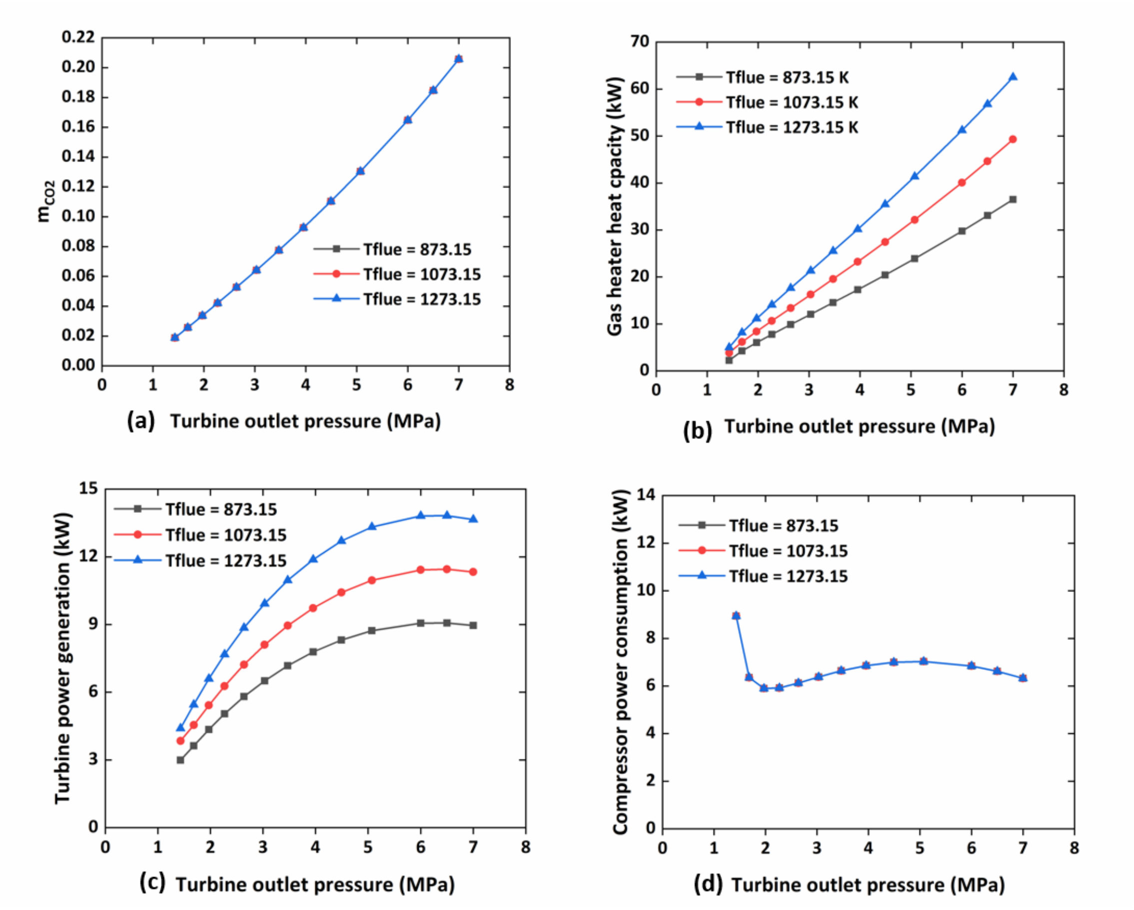

Figure 7. 6 Variation of (a) $CO_2$ mass flow rate (b) $CO_2$ gas heater capacity (c) turbine power (d) compressor power with different heat source temperature and turbine outlet pressure.

Exergy losses of different components were analyzed as shown in Figure 7.7 (a). Gas cooler has the highest exergy loss with the increase of turbine outlet pressure, which initially decreases and then increases due to it is affected by the parameter of compressor inlet. It should be note that exergy loss of recuperator is increased continuously with the increase in turbine outlet pressure, this is because the difference of heat specific between turbine outlet and compressor outlet is increased. Thermal efficiency and exergy efficiency are both related to power net work, according to the results of power generation and power consumption, there exits an optimal pressure ratio which cam maximize the thermal efficiency and exergy efficiency, as demonstrated in Figure 7.7 (b) and Figure 7.7(c).

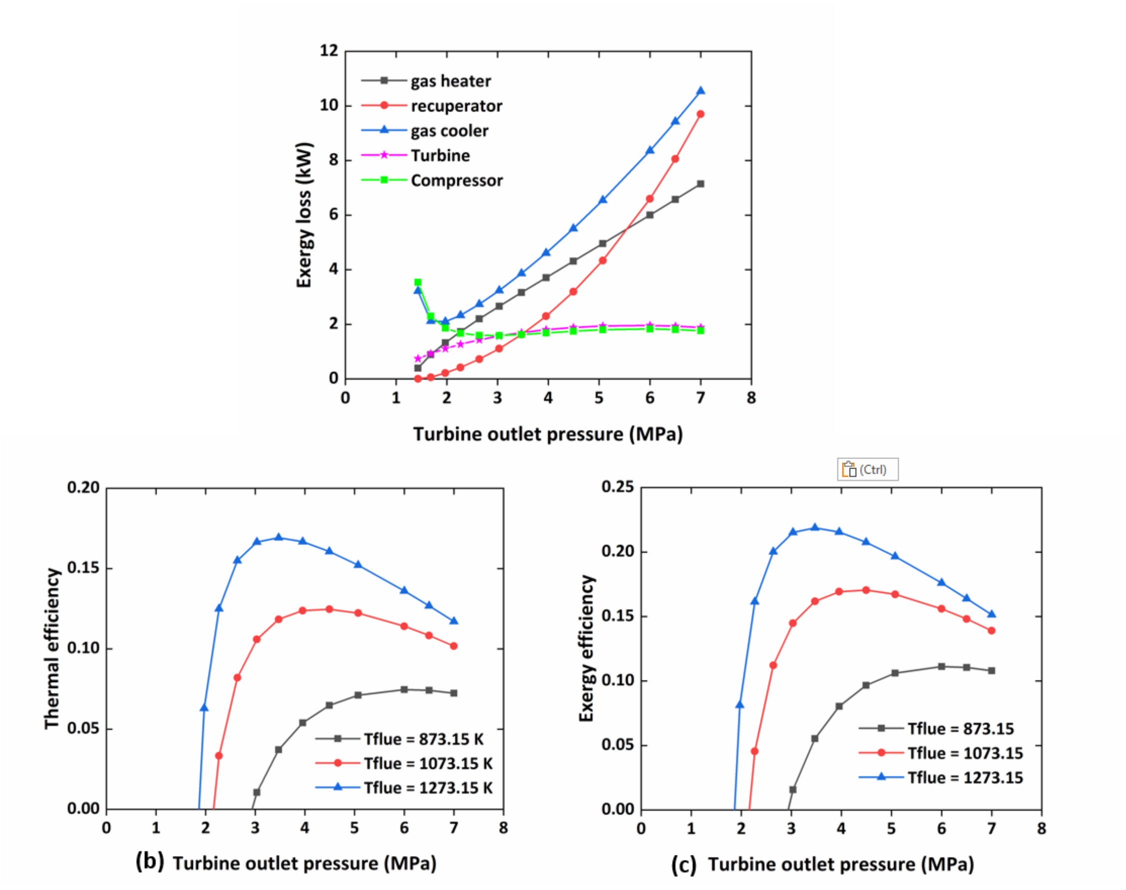

**Figure 7. 7 Variation of (a) energy loss (b) thermal efficiency (c) exergy efficiency with different heat source temperature and turbine outlet pressure.**

## 7.5 Summary

Thermodynamic simulations of proposed biomass-$CO_2$ transcritical Brayton cycle were carried out with the combination of $CO_2$ gas heater CFD simulation results. System performance at different operating conditions were evaluated. Simulation results showed that higher turbine inlet pressure leads to higher turbine power output and compressor energy consumption. Therefore, thermal efficiency and exergy efficiency increase at lower turbine inlet pressure, and when the difference between power generation and power consumption, efficiencies will be decreased. There exists an optimal value of pressure ratio to maximize the efficiencies of system. This conclusion also can be known from the study of turbine outlet pressure. In addition, the higher heat source mass flow rate and the lower temperature of heat sink contribute to higher thermal efficiency and exergy efficiency of this system.

**Chapter 8** will summarize the results of this thesis and provides recommendations for future work.

# Chapter 8 - Conclusions and Recommendations for Future Work

It is critical to investigate more sustainable and high-efficiency power generation systems considering rising population, economic development, increasing demand, and environmental impacts. $CO_2$ Brayton Cycle is a promising power generation system for converting biomass into a useful heat source. For further improving the performance of the proposed system, optimizations of heat exchangers by CFD simulations and understanding of system controls by thermodynamic analysis were carried out.

For investigating the feasibility of the finned-tube $CO_2$ gas cooler used in the proposed biomass-$CO_2$ Brayton Cycle and better understanding the performance of this type of heat exchanger, detailed and novel 1D–3D CFD simulations were carried out to analyze its performance as well as explore the optimizations. Shell-and-tube gas heater as an important component that can significantly influence the performance of the system due to it direct influences on the heat input of the whole system. A 3D CFD model was carried out to investigate the performance and optimization of the specific shell-and-tube $CO_2$ gas heater. In order to precisely evaluate the system performance, the thermodynamic model carried out by EES was combined with the results of gas heater CFD simulations.

## 8.1 CFD simulations of finned-tube $CO_2$ gas cooler

The outcomes of model simulations have been validated using experimental data from published literature and empirical correlations under various operating conditions. The validated model is then used to examine the impact of airflow maldistribution under varying operating conditions on the performance of a $CO_2$ finned-tube gas cooler and its associated system efficiency. The most important findings of this study are as follows:

- The proposed method produces additional and valuable results that cannot be obtained by other methods. The results of the present investigation are more precise and require less computing time.
- This novel 1D-3D model not only able to evaluate the airside heat transfer coefficient and airside pressure drop, but also can predict the $CO_2$ side heat transfer coefficient and it temperature profile along its flow direction. In addition, this model can be used for different applications such as investigations of the airflow velocity maldistribution effects.
- The airside heat transfer coefficient increases with increasing air inlet velocity, temperature, and refrigerant pressure.
- For both the uniform airflow velocity profile and the non-uniform velocity profile, the airside pressure drops increases as the air inlet average velocity increases. Reducing pressure drop is an effective method to decrease the fan's power consumption.

- Due to the greater temperature difference between the air and tube surfaces, approximately 90% of the temperature decrease of the $CO_2$ happens in the first tube row of the gas cooler.

- It was found that longitudinal heat conduction through fins can reversely affect the $CO_2$ temperature profile. This is due to the heat is transferred from the hotter tube to colder tube across fin surfaces. The phenomenon of reverse heat transfer can be reduced by a pattern of linear-up airflow. However, its heating capacity is inferior to that of a pattern of uniform airflow.

- With an increase in refrigerant pressure (close to optimal pressure), air frontal velocity, and refrigerant mass flow rate, the heating capacity of a gas cooler and the cooling coefficient of performance (COP) of the system are enhanced. Under the situation that the airflow pattern is varied, a uniform air velocity profile can produce the optimum heating capacity and system cooling coefficient of performance (COP). At a constant evaporating temperature, a system with a uniform air velocity profile has a greater coefficient of performance (COP) than one with air flow maldistribution.

- According to results of the approach temperature, it was proved that finned-tube $CO_2$ gas cooler is a feasible option to be used in proposed biomass-$CO_2$ transcritical Brayton Cycle.

- This CFD model is a handy tool to better analyze and control of finned-tube $CO_2$ gas cooler as well as its associated system.

## 8.2 Improvements of finned-tube $CO_2$ gas cooler by eliminating longitudinal heat conduction

It is known from section 8.2 that heat conduction though fins can negatively influence the temperature of $CO_2$ in the finned-tube gas cooler. Therefore, to investigate the effects of heat conduction through fins on the performance of a finned-tube $CO_2$ gas cooler and the cooling COP of its associated transcritical refrigeration system were carried out by utilizing split fins. The following key points have been obtained and summarized:

- A finned-tube $CO_2$ gas cooler should not ignore heat conduction through fin surfaces due to the considerable temperature difference between neighboring tube rows. For the coil with continuous fins, it is noticed that heat dissipates smoothly across the entire fin surface. In contrast, heat dissipation is constrained and limited for coils with split fins. Splitting the fins is therefore important and a good way to prevent most heat transfer along the fins.
- The temperature profile of the refrigerant flow from entrance to outlet decreases smoothly along the tube circuit for the coil with split fins. As a result of the negative effect of heat conduction through fins, the refrigerant flow can be reheated in the middle part of the tube circuit with fins that are continuous.
- Reduction of approach temperature can be effectively achieved with maximum valve of 7.5 K. The lower approach temperature, the higher heating capacity and thus higher COP of system. Heating capacity can be improved by an average of 10% by replacing continuous fins with split fins.

- The results demonstrate that split fins should be applied between neighboring tube rows with the greatest temperature differential to prevent heat conduction via the fins. The location of split fins should therefore take into account the various tube circuitry layouts.

## 8.3 CFD simulations of supercritical $CO_2$ shell-and-tube gas heater

For evaluating the effects of $CO_2$ gas heater on performance of biomass-$CO_2$ transcritical Brayton Cycle, a detailed CFD model was developed and validated for analyzing the $CO_2$ gas heater at different operating conditions as well as its associated system. The following key points have been obtained and summarized:

- With an increase in mass flow rate on both the shell and tube sides, it is possible to enhance the heat transfer coefficient and pressure. The shell side thermal-hydraulic performance was successfully validated with Kern and Bell-Delaware method, and it was demonstrated that Bell-Delaware method can predict pressure drop more precisely than Kern method.
- If the positions of the flue gas entry and exit ports are far from the shell's ends, stagnant zones may exist. As a result of the relative lower velocity, the heat transfer coefficients in stagnant zones are lower, resulting in decreased heat transfer rates.

- It is noticed that fluid velocity increases after crossing a baffle. However, recirculation zones are produced behind each baffle, where fluid velocities are lower, making these regions inefficient.
- The heating capacity of the gas heater increases with increasing flue gas temperature, flue gas mass flow rate, and $CO_2$ mass flow rate. However, the influence of $CO_2$ pressure on the heating capacity is neglectable.
- Both flue gas mass flow rate and $CO_2$ pressure have a substantial impact on the thermal efficiency of the system, which may be accounted for in optimal control strategies. With a higher flue gas mass flow rate, the rate of thermal efficiency improvement decreases. There exists a $CO_2$ pressure that maximizes the thermal efficiency of the system.
- Through relocating the flue gas inlet and outlet ports of shell-and-tube heat exchanger (STHXB), the shell side heat transfer coefficient, effectiveness and heating capacity of heat exchanger can be effectively improved. Although higher power consumption of exhaust fan can be caused, the increment of pressure drop is still lower than that of heat transfer coefficient. As a result, it is concluded that STHXB has better performance compared to original $CO_2$ gas heater STHXA, which can contribute to higher thermal efficiency of associated system.

## 8.4 Thermodynamic analysis of biomass-$CO_2$ transcritical Brayton Cycle

A thermodynamic model was carried out to analyze the effects of flue gas temperature, flue gas flow rate, heat sink temperature, $CO_2$ turbine inlet and outlet pressure on performance of biomass-$CO_2$ transcritcial Brayton Cycle. This thermodynamic model was integrated with the CFD results of $CO_2$ gas heater to achieve higher accuracy. The following key points have been obtained and summarized:

- The turbine power generation increases with higher turbine inlet pressure, higher turbine outlet pressure, higher heat source temperature and higher heat source mass flow rate.
- Mass flow rate of $CO_2$ decreases with the increase of turbine inlet and outlet pressure.
- Power consumption of compressor increases with higher $CO_2$ turbine inlet pressure. In contrast, with the increase in turbine outlet pressure, it decreases at lower outlet pressure and then increases at higher outlet pressure.
- With $CO_2$ turbine inlet pressure increasing, gas cooler has the highest exergy loss at higher turbine inlet pressure. Exergy loss of recuperator decreases with increases in turbine inlet pressure.
- Exergy loss of gas heater and recuperator can be increased with higher turbine outlet pressure. In addition, exergy loss of gas cooler decreases at lower turbine outlet pressure and continuously increase at higher turbine outlet pressure.

- System thermal efficiency and exergy efficiency increases with higher heat source temperature, higher heat source mass flow rate and lower heat sink temperature. An important finding is that there exists an optimal $CO_2$ turbine inlet pressure or $CO_2$ turbine outlet pressure to maximize the system thermal efficiency and system exergy efficiency.
- The model development and simulation can contribute significantly to understand the system operations and eventually optimise the system structure designs and controls.

## 8.5 Suggestions for future work

In this thesis, a small-scale biomass-$CO_2$ Transcritical Brayton Cycle power generation system was designed and constructed. Detailed analysis of heat exchangers (finned-tube $CO_2$ gas cooer and $CO_2$ gas heater) and whole system contributes to development of the proposed system.

For CFD simulations of finned-tube gas cooler, although effects of many impact parameters have been investigated and analysed, a possible future work would be to explore different geometries such as different tube circuits with different locations of split fins for high temperature working fluid to further improve the performance of finned-tube gas cooler. In addition, theoretical study could be conducted into analysing performance of replacing the plate heat exchanger with a finned-tube gas cooler in the proposed biomass-$CO_2$ transcritical power system.

In the CFD simulations of supercritical $CO_2$ gas heater, although relocating the inlet and outlet ports can effectively eliminate the stagnant regions and improve the performance of both heat exchanger and system. Stagnant regions still exit when fluid flows after baffles. For further improving the performance of the long-length $CO_2$ gas heater and associated biomass-$CO_2$ power generation system, a future work would be to investigate effects of increasing baffles number.

Although the results of CFD modelling and manufacturing data were integrated in the thermodynamic EES modeling, a combination of CFD simulations and component model development in TRNSYS would be required in future work.

The majority of the work carried out in this thesis was mainly based on modelling methods. Although simulations were validated with published literature, empirical correlations and manufacture data, showing good agreements. A possible future work would be to analyse the performance of components and whole system experimentally. Experimental data provides more solid and reliable validation of simulations.

# References

[1] Statistical Review of World Energy 2021, 70th edition. [online] Available at: <https://www.bp.com/en/global/corporate/energy-economics/statistical-review-of-world-energy.html> [Accessed 23 June 2022].

[2] IEA. 2022. Global Energy Review: $CO_2$ Emissions in 2021 – Analysis - IEA. [online] Available at: <https://www.iea.org/reports/global-energy-review-$CO_2$-emissions-in-2021-2> [Accessed 23 June 2022].

[3] GOV.UK. 2022. *UK energy in brief 2021*. [online] Available at: <https://www.gov.uk/government/statistics/uk-energy-in-brief-2021> [Accessed 23 June 2022].

[4] Reddy, C.C.S., Naidu, S.V. and Rangaiah, G.P., 2013. Waste heat recovery methods and technologies. *Chemical Engineering*, *120*(1), pp.28-38.

[5] Tchanche, B.F., Lambrinos, G., Frangoudakis, A. and Papadakis, G., 2011. Low-grade heat conversion into power using organic Rankine cycles–A review of various applications. *Renewable and Sustainable Energy Reviews*, *15*(8), pp.3963-3979.

[6] Pospíšil, J., Lisý, M. and Špiláček, M., 2016. Optimalization of Afterburner Channel in Biomass Boiler Using CFD Analysis. *Acta Polytechnica*, *56*(5), pp.379-387.

[7] Ge, Y.T., Tassou, S.A., Santosa, I.D. and Tsamos, K., 2015. Design optimisation of $CO_2$ gas cooler/condenser in a refrigeration system. *Applied Energy*, *160*, pp.973-981.

[8] Ge, Y.T. and Tassou, S.A., 2011. Performance evaluation and optimal design of supermarket refrigeration systems with supermarket model “SuperSim”. Part II: Model applications. *International journal of refrigeration*, *34*(2), pp.540-549.

[9] Kacludis, A., Lyons, S., Nadav, D. and Zdankiewicz, E., 2012. Waste heat to power (WH2P) applications using a supercritical $CO_2$-based power cycle. *Power-Gen International*, *2012*, pp.11-13.

[10] Cayer, E., Galanis, N., Desilets, M., Nesreddine, H. and Roy, P., 2009. Analysis of a carbon dioxide transcritical power cycle using a low temperature source. *Applied Energy*, *86*(7-8), pp.1055-1063.

[11] Pan, L., Li, B., Wei, X. and Li, T., 2016. Experimental investigation on the $CO_2$ transcritical power cycle. *Energy*, *95*, pp.247-254.

[12] Liu, H., Shao, Y. and Li, J., 2011. A biomass-fired micro-scale CHP system with organic Rankine cycle (ORC)–Thermodynamic modelling studies. *Biomass and Bioenergy*, *35*(9), pp.3985-3994.

[13] Qiu, G., Shao, Y., Li, J., Liu, H. and Riffat, S.B., 2012. Experimental investigation of a biomass-fired ORC-based micro-CHP for domestic applications. *Fuel*, *96*, pp.374-382.

[14] Hung, T.C., Shai, T.Y. and Wang, S.K., 1997. A review of organic Rankine cycles (ORCs) for the recovery of low-grade waste heat. *Energy*, *22*(7), pp.661-667.

[15] Chen, Y., Lundqvist, P., Johansson, A. and Platell, P., 2006. A comparative study of the carbon dioxide transcritical power cycle compared with an organic Rankine cycle with R123 as working fluid in waste heat recovery. *Applied thermal engineering*, *26*(17-18), pp.2142-2147.

[16] Brun, K., Friedman, P. and Dennis, R. eds., 2017. *Fundamentals and applications of supercritical carbon dioxide ($sCO_2$) based power cycles*. Woodhead publishing.

[17] Tchanche, B.F., Pétrissans, M. and Papadakis, G., 2014. Heat resources and organic Rankine cycle machines. *Renewable and Sustainable Energy Reviews*, *39*, pp.1185-1199.

[18] Hung, T.C., Shai, T.Y. and Wang, S.K., 1997. A review of organic Rankine cycles (ORCs) for the recovery of low-grade waste heat. *Energy*, *22*(7), pp.661-667.

[19] Rahbar, K., Mahmoud, S., Al-Dadah, R.K., Moazami, N. and Mirhadizadeh, S.A., 2017. Review of organic Rankine cycle for small-scale applications. *Energy conversion and management*, *134*, pp.135-155.

[20] Maizza, V. and Maizza, A., 1996. Working fluids in non-steady flows for waste energy recovery systems. *Applied Thermal Engineering*, *16*(7), pp.579-590.

[21] Saleh, B., Koglbauer, G., Wendland, M. and Fischer, J., 2007. Working fluids for low-temperature organic Rankine cycles. *Energy*, *32*(7), pp.1210-1221.

[22] Bini, R., Di Prima, M. and Guercio, A., 2010. Organic Rankine cycle (ORC) in biomass plants: an overview on different applications. *Brescia, Italy: Turboden srl*.

[23] Duvia, A., Guercio, A. and Rossi, C., 2009, June. Technical and economic aspects of Biomass fuelled CHP plants based on ORC turbogenerators feeding existing district heating networks. In *Proceedings of the 17th European biomass conference, Hamburg, Germany* (Vol. 29).

[24] Drescher, U. and Brüggemann, D., 2007. Fluid selection for the Organic Rankine Cycle (ORC) in biomass power and heat plants. *Applied thermal engineering*, *27*(1), pp.223-228.

[25] Algieri, A. and Morrone, P., 2012. Comparative energetic analysis of high-temperature subcritical and transcritical Organic Rankine Cycle (ORC). A biomass application in the Sibari district. *Applied Thermal Engineering*, *36*, pp.236-244.

[26] Cohen, G., Cable, R., Brosseau, D. and Price, H., 2005. Parabolic trough organic Rankine cycle solar power plant. *2004 DOE Sol. Energy Technol. Progr. Rev. Meet.,*.

[27] Lecompte, S., Huisseune, H., Van Den Broek, M., Vanslambrouck, B. and De Paepe, M., 2015. Review of organic Rankine cycle (ORC) architectures for waste heat recovery. *Renewable and sustainable energy reviews*, *47*, pp.448-461.

[28] Wei, D., Lu, X., Lu, Z. and Gu, J., 2007. Performance analysis and optimization of organic Rankine cycle (ORC) for waste heat recovery. *Energy conversion and Management*, *48*(4), pp.1113-1119.

[29] Hung, T.C., 2001. Waste heat recovery of organic Rankine cycle using dry fluids. *Energy Conversion and management*, *42*(5), pp.539-553.

[30] Liu, B.T., Chien, K.H. and Wang, C.C., 2004. Effect of working fluids on organic Rankine cycle for waste heat recovery. *Energy*, *29*(8), pp.1207-1217.

[31] Feher, E.G., 1968. The supercritical thermodynamic power cycle. *Energy conversion*, *8*(2), pp.85-90.

[32] Chen, H., Goswami, D.Y. and Stefanakos, E.K., 2010. A review of thermodynamic cycles and working fluids for the conversion of low-grade heat. *Renewable and sustainable energy reviews*, *14*(9), pp.3059-3067.

[33] Yamaguchi, H., Zhang, X.R., Fujima, K., Enomoto, M. and Sawada, N., 2006. Solar energy powered Rankine cycle using supercritical $CO_2$. *Applied thermal engineering*, *26*(17-18), pp.2345-2354.

[34] Angelino, G., 1968. Carbon dioxide condensation cycles for power production.

[35] Chen, H., Goswami, D.Y., Rahman, M.M. and Stefanakos, E.K., 2011. Energetic and exergetic analysis of $CO_2$-and R32-based transcritical Rankine cycles for low-grade heat conversion. *Applied Energy*, *88*(8), pp.2802-2808.

[36] Li, X. and Zhang, X., 2011. Component exergy analysis of solar powered transcritical $CO_2$ Rankine cycle system. *Journal of Thermal Science*, *20*(3), pp.195-200.

[37] Galanis, N., Cayer, E., Roy, P.A., Denis, E.S. and Desilets, M., 2012. Electricity generation from low temperature sources. *Journal of applied fluid mechanics*, *2*(2), pp.55-67.

[38] Chen, Y., 2006. *Novel cycles using carbon dioxide as working fluid: new ways to utilize energy from low-grade heat sources* (Doctoral dissertation, KTH).

[39] Chen, Y., Pridasawas, W. and Lundqvist, P., 2010. Dynamic simulation of a solar-driven carbon dioxide transcritical power system for small scale combined heat and power production. *Solar Energy*, *84*(7), pp.1103-1110.

[40] Shengjun, Z., Huaixin, W. and Tao, G., 2011. Performance comparison and parametric optimization of subcritical Organic Rankine Cycle (ORC) and transcritical power cycle system for low-temperature geothermal power generation. *Applied energy*, *88*(8), pp.2740-2754.

[41] Li, L., Ge, Y.T., Luo, X. and Tassou, S.A., 2018. Experimental analysis and comparison between $CO_2$ transcritical power cycles and R245fa organic Rankine cycles for low-grade heat power generations. *Applied Thermal Engineering*, *136*, pp.708-717.

[42] Li, L., Ge, Y.T., Luo, X. and Tassou, S.A., 2016. Thermodynamic analysis and comparison between $CO_2$ transcritical power cycles and R245fa organic Rankine cycles for low grade heat to power energy conversion. *Applied Thermal Engineering*, *106*, pp.1290-1299.

[43] Hejzlar, P., Dostal, V., Driscoll, M.J., Dumaz, P., Poullennec, G. and Alpy, N., 2006. Assessment of gas cooled fast reactor with indirect supercritical $CO_2$ cycle. *Nuclear Engineering and Technology*, *38*(2), pp.109-118.

[44] Ahn, Y., Bae, S.J., Kim, M., Cho, S.K., Baik, S., Lee, J.I. and Cha, J.E., 2015. Review of supercritical $CO_2$ power cycle technology and current status of research and development. *Nuclear engineering and technology*, *47*(6), pp.647-661.

[45] Wang, L., Pan, L.M., Wang, J., Chen, D., Huang, Y. and Hu, L., 2019. Investigation on the temperature sensitivity of the S-$CO_2$ Brayton cycle efficiency. *Energy*, *178*, pp.739-750.

[46] Zhang, Z., Chen, L., Yang, B., Ge, Y. and Sun, F., 2015. Thermodynamic analysis and optimization of an air Brayton cycle for recovering waste heat of blast furnace slag. *Applied Thermal Engineering*, *90*, pp.742-748.

[47] Olumayegun, O., Wang, M. and Kelsall, G., 2017. Thermodynamic analysis and preliminary design of closed Brayton cycle using nitrogen as working fluid and coupled to small modular Sodium-cooled fast reactor (SM-SFR). *Applied Energy*, *191*, pp.436-453.

[48] Wright, S.A., Vernon, M.E. and Pickard, P.S., 2013. *Concept design for a high temperature helium Brayton cycle with interstage heating and cooling* (No. SAND2006-4147). Sandia National Lab.(SNL-NM), Albuquerque, NM (United States).

[49] Gad-Briggs, A. and Pilidis, P., 2017. Analyses of Simple and Intercooled Recuperated Direct Brayton Helium Gas Turbine Cycles for Generation IV Reactor Power Plants. *Journal of Nuclear Engineering and Radiation Science*, *3*(1).

[50] Dostal, V., Hejzlar, P. and Driscoll, M.J., 2006. The supercritical carbon dioxide power cycle: comparison to other advanced power cycles. *Nuclear technology*, *154*(3), pp.283-301.

[51] Bae, S.J., Lee, J., Ahn, Y. and Lee, J.I., 2015. Preliminary studies of compact Brayton cycle performance for small modular high temperature gas-cooled reactor system. *Annals of Nuclear Energy*, *75*, pp.11-19.

[52] Ishiyama, S., Muto, Y., Kato, Y., Nishio, S., Hayashi, T. and Nomoto, Y., 2008. Study of steam, helium and supercritical $CO_2$ turbine power generations in prototype fusion power reactor. *Progress in nuclear energy*, *50*(2-6), pp.325-332.

[53] Edward, J.P., Steven, A.W. and Milton, E.V., 2011. Supercritical $CO_2$ Direct Cycle Gas Fast Reactor (SCGFR) Concept. *Sandia National Lab., Albuquerque, NM, Report No. SAND2011-2525*.

[54] Liu, Y., Wang, Y. and Huang, D., 2019. Supercritical $CO_2$ Brayton cycle: A state-of-the-art review. *Energy*, *189*, p.115900.

[55] Dostal, V., Driscoll, M.J. and Hejzlar, P., 2004. A supercritical carbon dioxide cycle for next generation nuclear reactors.

[56] Wright, S.A., Radel, R.F., Vernon, M.E., Pickard, P.S. and Rochau, G.E., 2010. *Operation and analysis of a supercritical $CO_2$ Brayton cycle* (No. SAND2010-0171). Sandia National Laboratories (SNL), Albuquerque, NM, and Livermore, CA (United States).

[57] Qiu, Y., Li, M.J., He, Y.L. and Tao, W.Q., 2017. Thermal performance analysis of a parabolic trough solar collector using supercritical $CO_2$ as heat transfer fluid under non-uniform solar flux. *Applied Thermal Engineering*, *115*, pp.1255-1265.

[58] Reyes-Belmonte, M.A., Sebastián, A., Romero, M. and González-Aguilar, J., 2016. Optimization of a recompression supercritical carbon dioxide cycle for an innovative central receiver solar power plant. *Energy*, *112*, pp.17-27.

[59] Mecheri, M. and Le Moullec, Y., 2016. Supercritical $CO_2$ Brayton cycles for coal-fired power plants. *Energy*, *103*, pp.758-771.

[60] Le Moullec, Y., 2013. Conceptual study of a high efficiency coal-fired power plant with $CO_2$ capture using a supercritical $CO_2$ Brayton cycle. *Energy*, *49*, pp.32-46.

[61] Sadeghianjahromi, A. and Wang, C.C., 2021. Heat transfer enhancement in fin-and-tube heat exchangers–A review on different mechanisms. *Renewable and Sustainable Energy Reviews*, *137*, p.110470.

[62] Tsamos, K.M., Ge, Y.T., Santosa, I.D.M.C. and Tassou, S.A., 2017. Experimental investigation of gas cooler/condenser designs and effects on a $CO_2$ booster system. *Applied Energy*, *186*, pp.470-479.

[63] Jamali, S., Yari, M. and Mohammadkhani, F., 2017. Performance improvement of a transcritical $CO_2$ refrigeration cycle using two-stage thermoelectric modules in sub-cooler and gas cooler. *International Journal of Refrigeration*, *74*, pp.105-115.

[64] Kim, M.S., Kang, D.H., Kim, M.S. and Kim, M., 2017. Investigation on the optimal control of gas cooler pressure for a $CO_2$ refrigeration system with an internal heat exchanger. *International Journal of Refrigeration*, *77*, pp.48-59.

[65] Liao, S.M., Zhao, T.S. and Jakobsen, A., 2000. A correlation of optimal heat rejection pressures in transcritical carbon dioxide cycles. *Applied Thermal Engineering*, *20*(9), pp.831-841.

[66] Ge, Y.T. and Tassou, S.A., 2009. Control optimisation of $CO_2$ cycles for medium temperature retail food refrigeration systems. *International Journal of Refrigeration*, *32*(6), pp.1376-1388.

[67] Gnielinski, V., 1976. New equations for heat and mass transfer in turbulent pipe and channel flow. *Int. Chem. Eng.*, *16*(2), pp.359-368.

[68] Dang, C. and Hihara, E., 2004. In-tube cooling heat transfer of supercritical carbon dioxide. Part 1. Experimental measurement. *International journal of refrigeration*, *27*(7), pp.736-747.

[69] Oh, H.K. and Son, C.H., 2010. New correlation to predict the heat transfer coefficient in-tube cooling of supercritical $CO_2$ in horizontal macro-tubes. *Experimental Thermal and Fluid Science*, *34*(8), pp.1230-1241.

[70] Pettersen, J., Rieberer, R. and Munkejord, S.T., 2000. Heat transfer and pressure drop characteristics of supercritical carbon dioxide in microchannel tubes under cooling,

4th IIR Gustav Lorentzen Conference on Natural Working Fluids. In *A5127, SINTEF Energy Research, Refrigeration and Air Conditioning*.

[71] Pitla, S.S., Groll, E.A. and Ramadhyani, S., 2002. New correlation to predict the heat transfer coefficient during in-tube cooling of turbulent supercritical $CO_2$. *International journal of refrigeration*, *25*(7), pp.887-895.

[72] Wang, C.C., Chi, K.Y. and Chang, C.J., 2000. Heat transfer and friction characteristics of plain fin-and-tube heat exchangers, part II: Correlation. *International Journal of Heat and mass transfer*, *43*(15), pp.2693-2700.

[73] Shah, R.K. and Sekulic, D.P., 2003. *Fundamentals of heat exchanger design*. John Wiley & Sons.

[74] Ge, Y.T. and Cropper, R.T., 2009. Simulation and performance evaluation of finned-tube $CO_2$ gas coolers for refrigeration systems. *Applied Thermal Engineering*, *29*(5-6), pp.957-965.

[75] Lee, J. and Domanski, P.A., 1997. *Impact of air and refrigerant maldistributions on the performance of finned-tube evaporators with R-22 and R-407C. Final Report* (No. DOE/CE/23810-81). Air-Conditioning and Refrigeration Technology Inst., Inc., Arlington, VA (United States).

[76] Starace, G., Fiorentino, M., Longo, M.P. and Carluccio, E., 2017. A hybrid method for the cross flow compact heat exchangers design. *Applied Thermal Engineering*, *111*, pp.1129-1142.

[77] Erek, A., Özerdem, B., Bilir, L. and Ilken, Z., 2005. Effect of geometrical parameters on heat transfer and pressure drop characteristics of plate fin and tube heat exchangers. *Applied Thermal Engineering*, *25*(14-15), pp.2421-2431.

[78] Bhuiyan, A.A., Amin, M.R. and Islam, A.S., 2013. Three-dimensional performance analysis of plain fin tube heat exchangers in transitional regime. *Applied Thermal Engineering*, *50*(1), pp.445-454.

[79] Yogesh, S.S., Selvaraj, A.S., Ravi, D.K. and Rajagopal, T.K.R., 2018. Heat transfer and pressure drop characteristics of inclined elliptical fin tube heat exchanger of varying ellipticity ratio using CFD code. *International journal of heat and mass transfer*, *119*, pp.26-39.

[80] Park, C.Y. and Hrnjak, P., 2007. Effect of heat conduction through the fins of a microchannel serpentine gas cooler of transcritical $CO_2$ system. *International Journal of Refrigeration*, *30*(3), pp.389-397.

[81] Zilio, C., Cecchinato, L., Corradi, M. and Schiochet, G., 2007. An assessment of heat transfer through fins in a fin-and-tube gas cooler for transcritical carbon dioxide cycles. *HVAC&R Research*, *13*(3), pp.457-469.

[82] Baek, S., Kim, J.H., Jeong, S. and Jung, J., 2012. Development of highly effective cryogenic printed circuit heat exchanger (PCHE) with low axial conduction. *Cryogenics*, *52*(7-9), pp.366-374.

[83] Romero-Méndez, R., Sen, M., Yang, K.T. and McClain, R.L., 1997. Effect of tube-to-tube conduction on plate-fin and tube heat exchanger performance. *International journal of heat and mass transfer*, *40*(16), pp.3909-3916.

[84] Domanski, P.A., Choi, J.M. and Payne, W.V., 2007, August. Longitudinal heat conduction in finned-tube evaporators. In *22nd IIR International Congress of Refrigeration, Beijing, China*.

[85] Chiou, J.P., 1978. Thermal performance deterioration in crossflow heat exchanger due to the flow nonuniformity.

[86] Hoffmann-Vocke, J., Neale, J. and Walmsley, M., 2011. The effect of inlet conditions on the air side hydraulic resistance and flow maldistribution in industrial air heaters. *International journal of heat and fluid flow*, *32*(4), pp.834-845.

[87] Ranganayakulu, C., Seetharamu, K.N. and Sreevatsan, K.V., 1996. The effects of inlet fluid flow nonuniformity on thermal performance and pressure drops in crossflow plate-fin compact heat exchangers. *International Journal of Heat and Mass Transfer*, *40*(1), pp.27-38.

[88] Aganda, A.A., Coney, J.E.R. and Sheppard, C.G.W., 2000. Airflow maldistribution and the performance of a packaged air conditioning unit evaporator. *Applied Thermal Engineering*, *20*(6), pp.515-528.

[89] Blecich, P., 2015. Experimental investigation of the effects of airflow nonuniformity on performance of a fin-and-tube heat exchanger. *International Journal of Refrigeration*, *59*, pp.65-74.

[90] Yaïci, W., Ghorab, M. and Entchev, E., 2014. 3D CFD analysis of the effect of inlet air flow maldistribution on the fluid flow and heat transfer performances of plate-fin-and-tube laminar heat exchangers. *International Journal of Heat and Mass Transfer*, *74*, pp.490-500.

[91] Lee, H.S., 2010. *Thermal design: heat sinks, thermoelectrics, heat pipes, compact heat exchangers, and solar cells*. John Wiley & Sons.

[92] Pekdemir, T., Davies, T.W., Haseler, L.E. and Diaper, A.D., 1994. Pressure drop measurements on the shell side of a cylindrical shell-and-tube heat exchanger. *Heat transfer engineering*, *15*(3), pp.42-56.

[93] Gay, B., Mackley, N.V. and Jenkins, J.D., 1976. Shell-side heat transfer in baffled cylindrical shell-and tube exchangers—an electrochemical mass-transfer modelling technique. *International Journal of Heat and Mass Transfer*, *19*(9), pp.995-1002.

[94] Kim, W.K. and Aicher, T., 1997. Experimental investigation of heat transfer in shell-and-tube heat exchangers without baffles. *Korean Journal of Chemical Engineering*, *14*(2), pp.93-100.

[95] Li, H. and Kottke, V., 1998. Local heat transfer in the first baffle compartment of the shell-and-tube heat exchangers for staggered tube arrangement. *Experimental thermal and fluid science*, *16*(4), pp.342-348.

[96] He, Z., Fang, X., Zhang, Z. and Gao, X., 2016. Numerical investigation on performance comparison of non-Newtonian fluid flow in vertical heat exchangers combined helical baffle with elliptic and circular tubes. *Applied Thermal Engineering*, *100*, pp.84-97.

[97] Pal, E., Kumar, I., Joshi, J.B. and Maheshwari, N.K., 2016. CFD simulations of shell-side flow in a shell-and-tube type heat exchanger with and without baffles. *Chemical engineering science*, *143*, pp.314-340.

[98] Ozden, E. and Tari, I., 2010. Shell side CFD analysis of a small shell-and-tube heat exchanger. *Energy Conversion and Management*, *51*(5), pp.1004-1014.

[99] Halle, H., Chenoweth, J.M. and Wambsganss, M.W., 1988. Shellside waterflow pressure drop distribution measurements in an industrial-sized test heat exchanger.

[100] Sparrow, E.M. and Reifschneider, L.G., 1986. Effect of interbaffle spacing on heat transfer and pressure drop in a shell-and-tube heat exchanger. *International journal of heat and mass transfer*, *29*(11), pp.1617-1628.

[101] Abeykoon, C., 2020. Compact heat exchangers–Design and optimization with CFD. *International Journal of Heat and Mass Transfer*, *146*, p.118766.

[102] El Maakoul, A., Laknizi, A., Saadeddine, S., El Metoui, M., Zaite, A., Meziane, M. and Abdellah, A.B., 2016. Numerical comparison of shell-side performance for shell and tube heat exchangers with trefoil-hole, helical and segmental baffles. *Applied Thermal Engineering*, *109*, pp.175-185.

[103] Kunwer, R., Pandey, S. and Bhurat, S.S., 2020. Comparison of selected shell and tube heat exchangers with segmental and helical baffles. *Thermal Science and Engineering Progress*, *20*, p.100712.

[104] Kral, D., Stehlik, P., Van Der Ploeg, H.J. and Master, B.I., 1996. Helical baffles in shell-and-tube heat exchangers, Part I: Experimental verification. *Heat transfer engineering*, *17*(1), pp.93-101.

[105] Bell, K.J., Kakac, S., Bergles, A. and Mayinger, F., 1981. Delaware method for shell side design, heat exchanger thermal-hydraulic fundamentals and design. *Kakac, AE Bergles, and F*.

[106] Kern, D.Q. and Kern, D.Q., 1950. *Process heat transfer* (Vol. 5). New York: McGraw-Hill.

[107] Gaddis, E.S. and Gnielinski, V., 1997. Pressure drop on the shell side of shell-and-tube heat exchangers with segmental baffles. *Chemical Engineering and Processing: Process Intensification*, *36*(2), pp.149-159.

[108] Jayachandriah, B. and Vinay, V., 2015. Design of helical baffle in shell and tube heat exchanger and comparing with segmental baffle using kern method. *Internasional Journal of Emerging Tehnology in Computer Science & Electronics*, *13*(2).

[109] Shinde, S. and Chavan, U., 2018. Numerical and experimental analysis on shell side thermo-hydraulic performance of shell and tube heat exchanger with continuous helical FRP baffles. *Thermal Science and Engineering Progress*, *5*, pp.158-171.

[110] Bayram, H. and Sevilgen, G., 2017. Numerical investigation of the effect of variable baffle spacing on the thermal performance of a shell and tube heat exchanger. *Energies*, *10*(8), p.1156.

[111] Zhang, X.Y., Ge, Y.T. and Sun, J.N., 2020. Performance analysis of finned-tube $CO_2$ gas cooler with advanced 1D-3D CFD modelling development and simulation. *Applied Thermal Engineering*, *176*, p.115421.

[112] Hwang, Y., Jin, D.H., Radermacher, R. and Hutchins, J.W., 2005. Performance Measurement of $CO_2$ Heat Exchangers. *ASHRAE transactions*, *111*(2).

[113] Singh, V., Abdelaziz, O., Aute, V. and Radermacher, R., 2011. Simulation of air-to-refrigerant fin-and-tube heat exchanger with CFD-based air propagation. International journal of refrigeration, 34(8), pp.1883-1897.

[114] Kim, M.H., Pettersen, J. and Bullard, C.W., 2004. Fundamental process and system design issues in $CO_2$ vapor compression systems. Progress in energy and combustion science, 30(2), pp.119-174.

[115] Zhang, X. and Ge, Y.T., 2021. The effect of heat conduction through fins on the performance of finned-tube $CO_2$ supercritical gas coolers. International Journal of Heat and Mass Transfer, 181, p.121908.

[116] Bergman, T.L., Bergman, T.L., Incropera, F.P., Dewitt, D.P. and Lavine, A.S., 2011. Fundamentals of heat and mass transfer. John Wiley & Sons.

[117] Pettersen, J., Rieberer, R. and Munkejord, S.T., 2000. Heat transfer and pressure drop for flow of supercritical and subcritical $CO_2$ in microchannel tubes. NORWEGIAN UNIV OF SCIENCE AND TECHNOLOGY TRONDHEIM DEPT OF REFRIGERATION AND AIR CONDITIONING.

[118] Dang, C. and Hihara, E., 2004. In-tube cooling heat transfer of supercritical carbon dioxide. Part 1. Experimental measurement. International journal of refrigeration, 27(7), pp.736-747.

[119] Olson, D.A., 2000. Heat transfer of supercritical carbon dioxide flowing in a cooled horizontal tube.

[120] Rossetti, A., Marinetti, S. and Minetto, S., 2018. Multi-physics simulation of $CO_2$ gas coolers using equivalence modelling. International Journal of Refrigeration, 90, pp.99-107.

[121] Sánchez, D., Cabello, R., Llopis, R. and Torrella, E., 2012. Development and validation of a finite element model for water– $CO_2$ coaxial gas-coolers. Applied energy, 93, pp.637-647.

[122] Yang, D., Khan, T.S., Al-Hajri, E., Ayub, Z.H. and Ayub, A.H., 2019. Geometric optimization of shell and tube heat exchanger with interstitial twisted tapes outside the tubes applying CFD techniques. Applied Thermal Engineering, 152, pp.559-572.

[123] Petukhov, B.S., Genin, L.G. and Kovalev, S.A., 1974. Heat transfer in nuclear power plants. M. Atomizdat.

[124] Ge, Y., Zhang, X., Ling C., Lang, P., 2020 Power Generation and Heat Recovery from Biomass with Advanced $CO_2$ Thermodynamic Power Cycles: Modelling Development and Simulation. IIR Rankine 2020 Conference - Advances in Cooling, Heating and Power Generation. Virtual. Paper ID 1229

# Appendix A

The calibration equations of the thermocouples for biomass-$CO_2$ Brayton Cycle system test rig are demonstrated in Table a.1.

General Equation of thermocouples:

$$Y = mX + b$$

X=measured temperature by thermocouple ˚C

Y=estimated actual value of temperature ˚C

m=slope of Y and X correlation

b= constant or Y intercept

$R^2$ =coefficient of correlation

**Table a. 1 Calibration equations of thermocouples for biomass-$CO_2$ Brayton Cycle system test rig.**

| Thermocouples | m | b | $R^2$ |
|---|---|---|---|
| T1 | 0.969007 | 0.933437 | 0.999991 |
| T2 | 0.968878 | 0.45975 | 0.999997 |
| T3 | 0.965952 | 0.775454 | 0.99999 |
| T4 | 0.964714 | 0.305189 | 0.999991 |
| T5 | 0.972173 | 0.410525 | 0.999964 |
| T6 | 0.968475 | 0.590778 | 0.999972 |
| T7 | 965979 | 0.051282 | 0.999963 |
| T8 | 0.972035 | 0.249693 | 0.999939 |
| T9 | 0.964232 | 0.735088 | 0.999979 |
| T10 | 0.965386 | 0.393377 | 0.999989 |
| T11 | 0.962972 | 0.726775 | 0.999984 |
| T12 | 0.960232 | 0.094247 | 0.999991 |
| T13 | 0.963869 | 0.463436 | 0.999987 |
| T14 | 0.96325 | 0.184175 | 0.999994 |
| T15 | 0.980856 | 0.468336 | 0.999845 |
| T16 | 0.972339 | 0.742046 | 0.999967 |
| T17 | 0.973277 | 0.312414 | 0.999995 |
| T18 | 0.969784 | 0.649764 | 0.999988 |
| T20 | 0.975784 | 0.341274 | 0.999996 |

# Appendix B

The C code for matching heat transfer coefficient from Phase I model to phase II model. Due to the code is too long, for saving the space, important part of the code is shown as below.

Figure b. 1 Print screen of C code for matching airside heat transfer coefficients to phase II model.

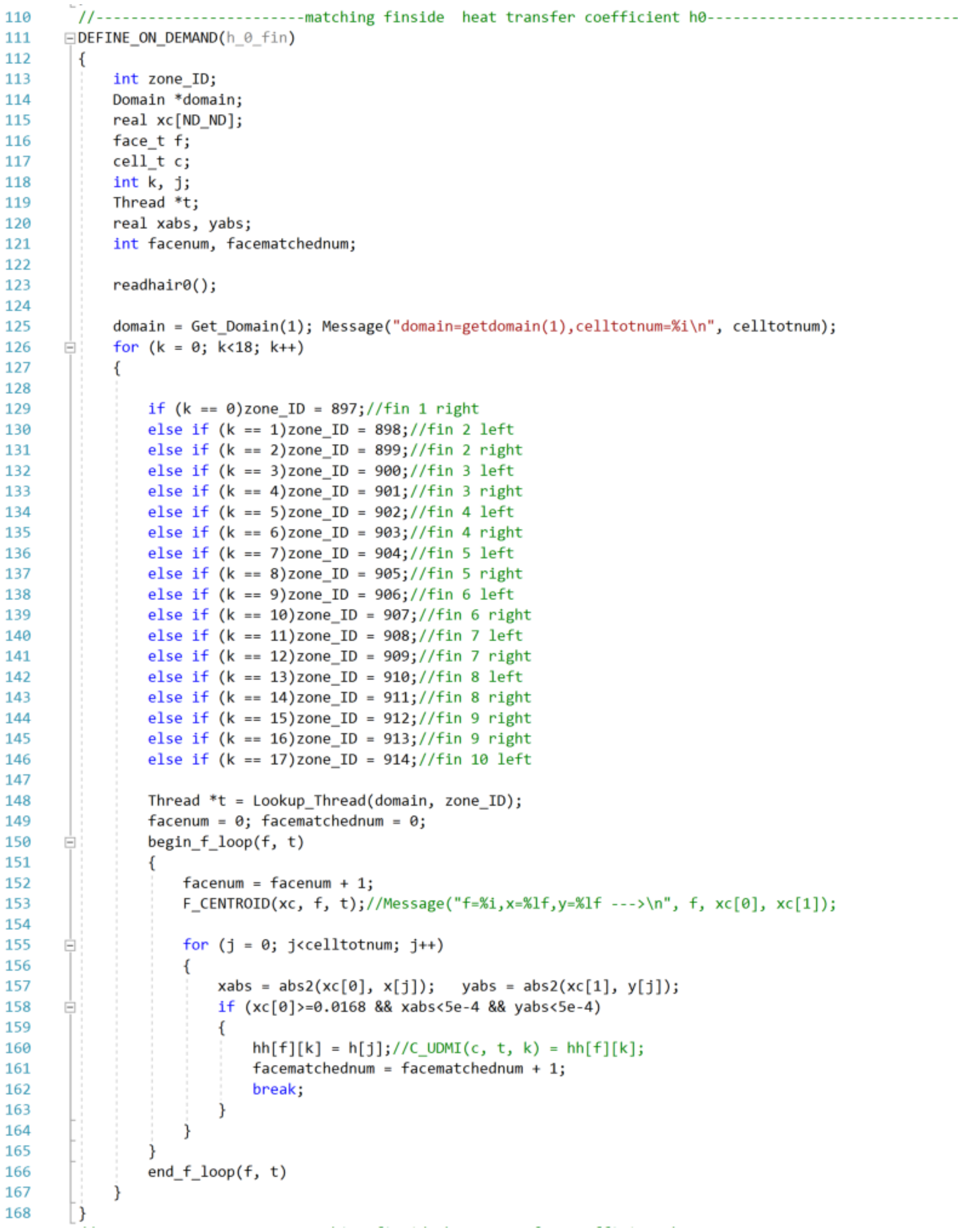

```c
//------------------------matching finside  heat transfer coefficient h0----------------------------
DEFINE_ON_DEMAND(h_0_fin)
{
    int zone_ID;
    Domain *domain;
    real xc[ND_ND];
    face_t f;
    cell_t c;
    int k, j;
    Thread *t;
    real xabs, yabs;
    int facenum, facematchednum;

    readhair0();

    domain = Get_Domain(1); Message("domain=getdomain(1),celltotnum=%i\n", celltotnum);
    for (k = 0; k<18; k++)
    {

        if (k == 0)zone_ID = 897;//fin 1 right
        else if (k == 1)zone_ID = 898;//fin 2 left
        else if (k == 2)zone_ID = 899;//fin 2 right
        else if (k == 3)zone_ID = 900;//fin 3 left
        else if (k == 4)zone_ID = 901;//fin 3 right
        else if (k == 5)zone_ID = 902;//fin 4 left
        else if (k == 6)zone_ID = 903;//fin 4 right
        else if (k == 7)zone_ID = 904;//fin 5 left
        else if (k == 8)zone_ID = 905;//fin 5 right
        else if (k == 9)zone_ID = 906;//fin 6 left
        else if (k == 10)zone_ID = 907;//fin 6 right
        else if (k == 11)zone_ID = 908;//fin 7 left
        else if (k == 12)zone_ID = 909;//fin 7 right
        else if (k == 13)zone_ID = 910;//fin 8 left
        else if (k == 14)zone_ID = 911;//fin 8 right
        else if (k == 15)zone_ID = 912;//fin 9 right
        else if (k == 16)zone_ID = 913;//fin 9 right
        else if (k == 17)zone_ID = 914;//fin 10 left

        Thread *t = Lookup_Thread(domain, zone_ID);
        facenum = 0; facematchednum = 0;
        begin_f_loop(f, t)
        {
            facenum = facenum + 1;
            F_CENTROID(xc, f, t);//Message("f=%i,x=%lf,y=%lf --->\n", f, xc[0], xc[1]);

            for (j = 0; j<celltotnum; j++)
            {
                xabs = abs2(xc[0], x[j]);   yabs = abs2(xc[1], y[j]);
                if (xc[0]>=0.0168 && xabs<5e-4 && yabs<5e-4)
                {
                    hh[f][k] = h[j];//C_UDMI(c, t, k) = hh[f][k];
                    facematchednum = facematchednum + 1;
                    break;
                }
            }
        }
        end_f_loop(f, t)
    }
}
```

The $CO_2$ side heat transfer coefficient and temperature are calculated as below C code, for saving space, the duplicated part are replace by ‘’…..’’. This is only an example at one specified operating condition. For different operating conditions, parameters in C code should be correspondingly changed.

Figure b. 2 Print screen of C code for calculating $CO_2$ heat transfer coefficients and temperature.

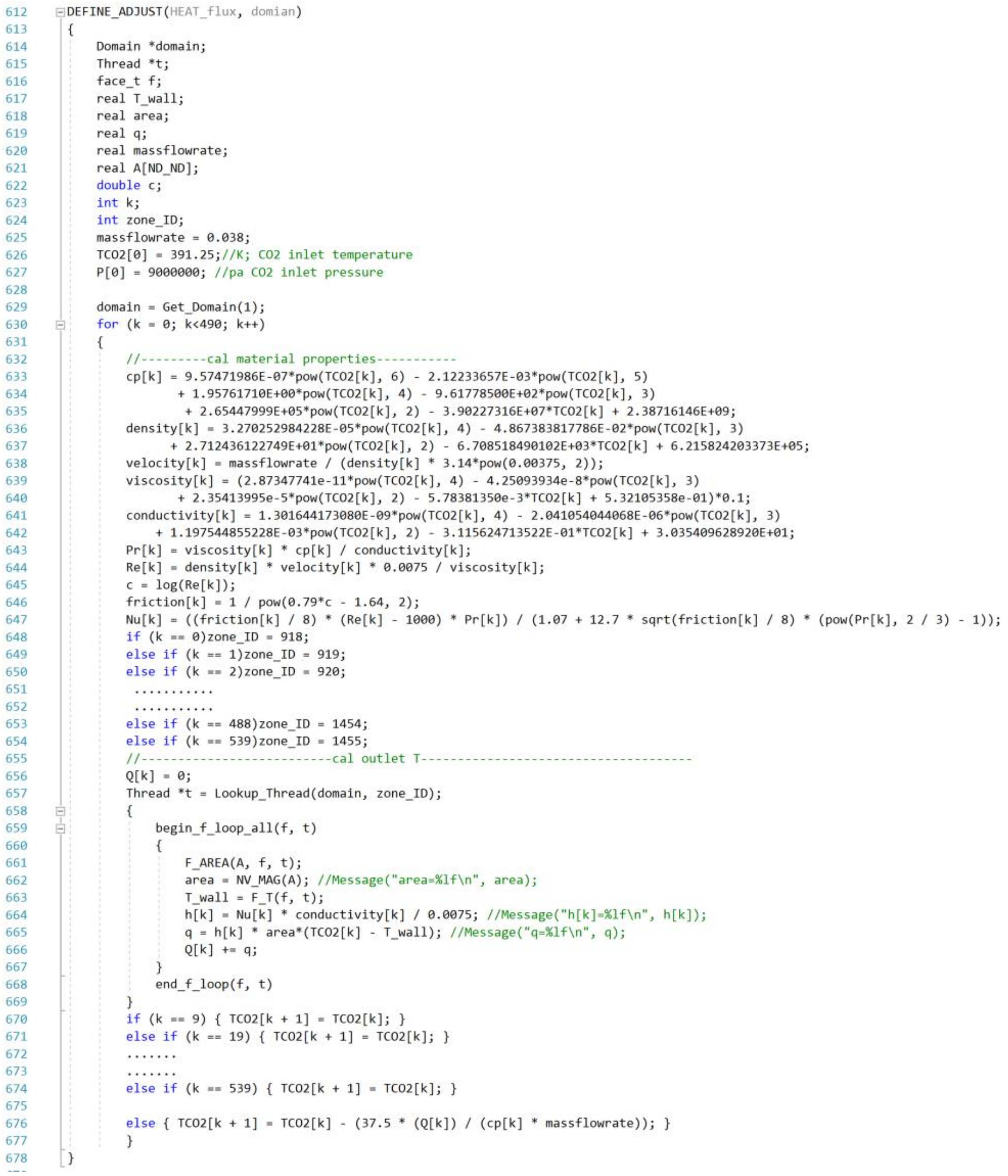

```
DEFINE_ADJUST(HEAT_flux, domian)
{
    Domain *domain;
    Thread *t;
    face_t f;
    real T_wall;
    real area;
    real q;
    real massflowrate;
    real A[ND_ND];
    double c;
    int k;
    int zone_ID;
    massflowrate = 0.038;
    TCO2[0] = 391.25;//K; CO2 inlet temperature
    P[0] = 9000000; //pa CO2 inlet pressure

    domain = Get_Domain(1);
    for (k = 0; k<490; k++)
    {
        //---------cal material properties-----------
        cp[k] = 9.57471986E-07*pow(TCO2[k], 6) - 2.12233657E-03*pow(TCO2[k], 5)
               + 1.95761710E+00*pow(TCO2[k], 4) - 9.61778500E+02*pow(TCO2[k], 3)
                + 2.65447999E+05*pow(TCO2[k], 2) - 3.90227316E+07*TCO2[k] + 2.38716146E+09;
        density[k] = 3.270252984228E-05*pow(TCO2[k], 4) - 4.867383817786E-02*pow(TCO2[k], 3)
              + 2.712436122749E+01*pow(TCO2[k], 2) - 6.708518490102E+03*TCO2[k] + 6.215824203373E+05;
        velocity[k] = massflowrate / (density[k] * 3.14*pow(0.00375, 2));
        viscosity[k] = (2.87347741e-11*pow(TCO2[k], 4) - 4.25093934e-8*pow(TCO2[k], 3)
               + 2.35413995e-5*pow(TCO2[k], 2) - 5.78381350e-3*TCO2[k] + 5.32105358e-01)*0.1;
        conductivity[k] = 1.301644173080E-09*pow(TCO2[k], 4) - 2.041054044068E-06*pow(TCO2[k], 3)
            + 1.197544855228E-03*pow(TCO2[k], 2) - 3.115624713522E-01*TCO2[k] + 3.035409628920E+01;
        Pr[k] = viscosity[k] * cp[k] / conductivity[k];
        Re[k] = density[k] * velocity[k] * 0.0075 / viscosity[k];
        c = log(Re[k]);
        friction[k] = 1 / pow(0.79*c - 1.64, 2);
        Nu[k] = ((friction[k] / 8) * (Re[k] - 1000) * Pr[k]) / (1.07 + 12.7 * sqrt(friction[k] / 8) * (pow(Pr[k], 2 / 3) - 1));
        if (k == 0)zone_ID = 918;
        else if (k == 1)zone_ID = 919;
        else if (k == 2)zone_ID = 920;
         ...........
         ...........
        else if (k == 488)zone_ID = 1454;
        else if (k == 539)zone_ID = 1455;
        //-------------------------cal outlet T-------------------------------------
        Q[k] = 0;
        Thread *t = Lookup_Thread(domain, zone_ID);
        {
            begin_f_loop_all(f, t)
            {
                F_AREA(A, f, t);
                area = NV_MAG(A); //Message("area=%lf\n", area);
                T_wall = F_T(f, t);
                h[k] = Nu[k] * conductivity[k] / 0.0075; //Message("h[k]=%lf\n", h[k]);
                q = h[k] * area*(TCO2[k] - T_wall); //Message("q=%lf\n", q);
                Q[k] += q;
            }
            end_f_loop(f, t)
        }
        if (k == 9) { TCO2[k + 1] = TCO2[k]; }
        else if (k == 19) { TCO2[k + 1] = TCO2[k]; }
        .......
        .......
        else if (k == 539) { TCO2[k + 1] = TCO2[k]; }

        else { TCO2[k + 1] = TCO2[k] - (37.5 * (Q[k]) / (cp[k] * massflowrate)); }
        }
}
```

# Appendix C

Airflow inlet velocity functions for linear-up, linear-down and parabolic. X is the position of air inlet.

- Linear-up:

$$v_a = 4.3478x + 1.8462, \qquad when\ v_{a,average\ inlet} = 1\ m/s$$

$$v_a = 8.6957x + 3.6924, \qquad when\ v_{a,average\ inlet} = 2\ m/s$$

$$v_a = 13.043x + 5.5385, \qquad when\ v_{a,average\ inlet} = 3\ m/s$$

- Linear-down:

$$v_a = -4.3478x + 0.1538, \qquad when\ v_{a,average\ inlet} = 1\ m/s$$

$$v_a = -8.6957x + 0.3076, \qquad when\ v_{a,average\ inlet} = 2\ m/s$$

$$v_a = -13.043x + 0.4615, \qquad when\ v_{a,average\ inlet} = 3\ m/s$$

- Parabolic

$$v_a = -28.335x^2 - 11.0371x + 0.4259, \qquad when\ v_{a,average\ inlet} = 1\ m/s$$

$$v_a = -56.71x^2 - 22.074x + 0.8519, \qquad when\ v_{a,average\ inlet} = 2\ m/s$$

$$v_a = -85.066x^2 - 33.111x + 1.278, \qquad when\ v_{a,average\ inlet} = 3\ m/s$$